

A NOVEL 2-D TRANSITION METAL CYANIDE MEMBRANE: MODELING,
STRUCTURAL, MAGNETIC, AND FUNCTIONAL CHARACTERIZATION

by

Marcus Goss

A dissertation submitted to the Graduate Council of
Texas State University in partial fulfillment
of the requirements for the degree of
Doctor of Philosophy
with a Major in Materials Science, Engineering, and Commercialization
August 2015

Committee Members:

Gary W. Beall, Chair

William Chittenden

L. Kevin Lewis

Glenn Longley

Clois E. Powell

COPYRIGHT

by

Marcus Goss

2015

FAIR USE AND AUTHOR'S PERMISSION STATEMENT

Fair Use

This work is protected by the Copyright Laws of the United States (Public Law 94-553, section 107). Consistent with fair use as defined in the Copyright Laws, brief quotations from this material are allowed with proper acknowledgment. Use of this material for financial gain without the author's express written permission is not allowed.

Duplication Permission

As the copyright holder of this work I, Marcus Goss, authorize duplication of this work, in whole or in part, for educational or scholarly purposes only.

DEDICATION

This work is dedicated to my wife and friend Mahdi Martin.

ACKNOWLEDGEMENTS

Thank you God.

Thank you mom, and dad.

I would like to extend my thanks and gratitude to Dr. Gary Beall. As my mentor he has provided guidance through more than 15 years of my life. It is thanks to him that I have found the courage and the desire to rise to this and many other challenges.

I thank my committee members; Dr. Bill Chittenden, Dr. Kevin Lewis, Dr. Glenn Longley, and Dr. Bert Powell.

I also thank Dr. Thomas Myers, Dr. Bill Brittain, Dr. Debra Feakes, Dr. Ross Compton, Dr. Pat Cassidy, Dr. Chad Booth, Dr. Chang Ji, Dr. Jennifer Irvin, Dr. Tania Betancourt, Dr. Ben Martin, Dr. Todd Hudnall, Dr. Chris Dorsey, and Dr. Robert Davis, Dr. Haoran Chen, Dr. Ray Cook, Dr. Amber Douglas, Dr. Tyler Nash, Sayantan Das, Ash Kotwal, Lisa Taylor, Travis Cantu, Dr. Brandon Henderson, Mike Gardner, Dr. Malcolm Prouty and Dr. David Irvin, Karla Pizana, Judy Thompson, Bryttne Lowden, George Steinke, Claudia Roeschmann, Marty Jacobvitz, Jamie Rhodes, Dan Millikin, Al Martinez, and Eric Shires.

TABLE OF CONTENTS

	Page
ACKNOWLEDGEMENTS	v
LIST OF TABLES	viii
LIST OF FIGURES	ix
ABSTRACT	xi
CHAPTER	
1. INTRODUCTION.....	1
1.1. Introduction.....	1
1.2. Transition Metal Cyanide Structure.....	3
1.3. Ion Selective Membrane for Desalination	7
1.4. Magnetic Properties	17
2. MOLECULAR DYNAMICS SIMULATIONS.....	20
2.1. Introduction to Molecular Dynamic Simulation	20
2.2. Model Construction	22
2.3. Models of Water Permeability	29
2.4. Models of Ion Selectivity.....	34
2.5. Energy of Pore Transit Modeling	35
3. EXPERIMENTAL METHODS	37
3.1. Preparation Methods for Cyanide-Bridged Transition Metal Complexes.....	37
3.1.1. Single Crystal Growth Method.....	37
3.1.2. Bulk Precipitation Method	40
3.1.3. Formation of Interfacial Sheet Method	41
3.2. Hydration States of Cyanide-Bridged Transition Metal Complexes.....	42

3.3. Exfoliation of 2D Sheets from 3D Frameworks	42
3.4. Ion Selective Membrane Fabrication and Testing	44
3.4.1. Deposition of Exfoliated Precipitated Powder	44
3.4.2. Deposition of Exfoliated Single Crystal	47
3.4.3. Interfacial Precipitation Method	48
3.4.4. Membrane Function Testing	49
3.5. Magnetic Property Experiments	50
3.5.1. Observation of Magnetic Susceptibility	50
3.5.2. Ferromagnetic Analysis	52
3.5.3. Thermal Gravimetric Analysis Magnetic Experiment	53
3.5.4. Vibrational Sample Magnetometer Experiments	55
4. RESULTS AND DISCUSSION	57
4.1. Molecular Dynamics Simulations	57
4.1.1. Model Construction and Crystallographic Comparisons	58
4.1.2. Water Permeability Models	60
4.1.3. Ion Selectivity Models	62
4.1.4. Pore Transit Energy of Single Molecule/Ion Models	64
4.2. Synthesis of Cyanide-Bridged Transition Metal Complexes	70
4.3. Ion Selective Membrane Fabrication	76
4.4. Dehydration Stability Study	77
4.5. Magnetic Properties	81
5. CONCLUSIONS	88
5.1. Summary	88
5.2. Future Work	89
APPENDIX SECTION	91
LITERATURE CITED	109

LIST OF TABLES

Table	Page
1. Comparison of future RO membrane technology performance to today's leading technology	15
2. Reactant loadings in single crystal growth in U-tube experiments	39
3. Reactant loadings in the bulk precipitation growth method	40
4. Saline water test solutions	50
5. Modeled bond lengths vs. crystallographic bond lengths.....	59
6. Comparison of the unit cell dimensions of molecular models with crystallographic data.....	60
7. Quantitative TGA results for composition of cyanide-bridged transition metal precipitated powders.....	73
8. Mass change in the isothermal samples under a magnetic field.....	86

LIST OF FIGURES

Figure	Page
1. Generalized diagram of a Hofmann clathrate	4
2. Simplified mechanism for exfoliation of 3D structures into 2D sheets.....	6
3. SEM images of transition metal cyanide nanosheets	7
4. Diagram showing square framework of atoms in the single layer	8
5. Water Scarcity Index	10
6. Osmosis of water through a semipermeable membrane	12
7. Typical thin film composite membrane	14
8. Simulation Tools – Time vs. Length scale	21
9. Partially dehydrated $\text{Fe}(\text{H}_2\text{O})_2\text{Ni}(\text{CN})_4 \cdot \text{H}_2\text{O}$ structure	25
10. Model of flat sheet of dehydrated $\text{FeNi}(\text{CN})_4$	27
11. Graphene and nanoporous graphene sheets.....	29
12. Diagram of piston model used to simulate pressure.....	30
13. Cycle of the steps in MD simulations.....	33
14. Periodic model of water desalination	35
15. Single crystal growth apparatus.....	38
16. SEM images of the hydrophobic and hydrophilic membrane supports.....	45
17. Observational magnetic experiment setup.....	52
18. Magnetic TGA Experiment	55

19. Plots of ion to water transit rates for FeNi(CN) ₄ and nanoporous graphene	63
20. Wire frame model of the close contacts of water and the sheet atoms while in the pore of a Pt ₂ Ni(CN) ₄ sheet	65
21. Sequence showing the orientation of water as it passes through the FeNi(CN) ₄ membrane	66
22. Energy profile of water during pore transit	67
23. Energy profile comparison of water, sodium ion, and chloride as they transit the pore	69
24. Energy profile comparison of hydrophobic and hydrophilic pores in nanoporous graphene	70
25. TGA plot of FeNi(CN) ₄	72
26. XRD powder diffraction patterns for the cyanide-bridged transition metal precipitates	74
27. SEM image of thin plate-like sheets of the exfoliated material.....	75
28. SEM image of the PVDF membrane after deposition of exfoliated Fe(H ₂ O) ₂ Ni(CN) ₄ powder.....	76
29. TGA Plot of Fe(H ₂ O) ₂ Ni(CN) ₄ ·4H ₂ O showing dehydration events.....	78
30. Plot of dehydration events, temperature vs. unit cell volume.....	79
31. Color change on dehydration of cyanide-bridged transition metal precipitated powder	80
32. Magnetic behavior in the precipitated powder	82
33. Ferromagnetic suspension test of suspended powder in water	83
34. TGA plot of the influence of a magnetic field on the precipitated powders	85
35. Vibrational sample magnetometer hysteresis loops	87

ABSTRACT

A novel 2-dimensional crystalline material composed of cyanide-bridged metal nanosheets with a square planar framework has been prepared. This material, similar to Hofmann clathrates, has a variety of interesting properties. The material is crystalline and possesses characteristics that include magnetic properties, electronic properties and useful structural features. They have recently been exfoliated into individual crystalline sheets. These sheets show a strong potential for use as ion selective membranes. Performance improvements in water purification and desalination by reverse osmosis methods owing to their single atom thickness is possible. A series of dynamic molecular simulations has provided an understanding of the mechanism for water permeability and salt rejection. Energy profiles for the passage of water and ionic species through the porous areas of these nanosheets have been built and reported. Performance estimates of the efficacy of this novel material for use as an ion selective membrane such as an improved desalination RO membrane are presented. Experiments in synthesis and exfoliation of this class of cyanide-bridged transition metal complex were conducted and the results are presented. A preliminary investigation into the magnetic properties of these materials is included.

CHAPTER 1

INTRODUCTION

1.1 Introduction

Transition metal compounds have long been studied and explored for their interesting characteristics such as their molecular magnetic and electronic properties and their use as pigments. The cyanide-bridged transition metal compound, Prussian blue, was discovered by Diesbach in 1704 and has been widely used as a dye pigment.¹ The chemical composition is iron(III)-hexacyanoferrate(II) and it is an octahedrally structured compound with six cyano ligands branching from a central iron(III) atom. The three dimensional structure originating from the transition metal center makes an excellent starting point for building two-dimensional (2D) and three-dimensional (3D) compounds. Transition metal cyanide-bridged frameworks have been the subject of many investigations over the past 50 years and have led to numerous applications. They have also played a critical role in the understanding of coordination chemistry.²⁻⁵

This research has explored a series of cyanide-bridged transition metal compounds that form 3D structures. They are then separated into 2D sheets and explored as membranes for ion selectivity. These compounds represent a new approach to building 2D and 3D materials composed of crystalline polymeric networks. A similar structure exists in the family of complexes called Hofmann clathrates.⁶ Their structure also contains square planar nickel atoms with four cyanide bridges to adjacent transition metals. Octahedral coordination at the transition metal sites allows for two additional

molecules to form coordination bonding perpendicular to this plane. In Hofmann clathrates these species are typically amines. The interlayer molecules that occupy the space between the layers are typically aromatic compounds such as benzene.⁶ The 3D structure presented in this work is without aromatic compounds. The structure is still maintained by coordinating water in the interstitial spaces. Applications of these types of materials are catalysis, molecular magnetism, electronic materials and bioengineering.⁷⁻¹⁵ Few studies have been focused on the potential membrane applications of these structures.¹⁶⁻²⁰

This metal cyanide-bridged framework has been studied recently at Texas State University. The majority of applications where transition metal cyano complexes are utilized takes advantage of the 3D structural properties of the material. Encapsulation of molecules has been studied as one example.^{19,21} A stable 2D structure from a complex that forms a 3D framework shares many considerations with the use of naturally occurring smectic clays in polymeric nanocomposite materials.^{22,23} The separation and utilization of individual sheets of clay from stacked structures is at the crux of manipulating those materials into a beneficial additive.²⁴ Studies have shown that exfoliation, which is considered complete separation of sheets from a layered material, can be achieved by substituting interlayer components. This strategy, applied to the metal cyanide-bridged framework, has resulted in creation of a new 2D material.²⁵

1.2 Transition Metal Cyanide Structure

The basic structure of 3D frameworks is built from alternating units of a divalent six-coordination transition metal center with a divalent metal in square planar or four-coordination. A cyanide group forms a bridge between these centers in each of four directions. This forms a planar lattice network of squares that extend into two dimensions. In assigning a unit cell to the structure typically the plane containing these atoms will be given by the a and b direction. The c dimension of the unit cell runs perpendicular to this plane. A lack of bonding between individual metal cyanide sheets creates an interlamellar or basal space between them in the c direction. This space is occupied by molecules coordination-bonded to the two available coordination sites above and below the plane. The distance of the basal space is dependent on the identity and size of the molecule. Additional molecules may also occupy this space. Figure 1 shows a general representation of the 3D structure and the guest molecules occupying the basal space.

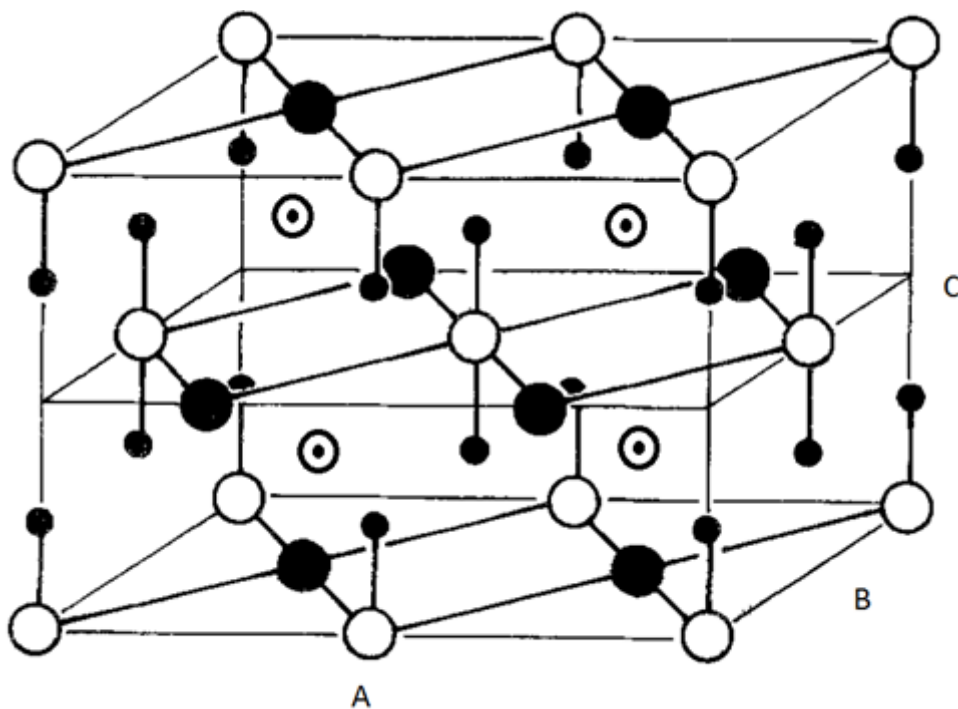


Figure 1. Generalized diagram of a Hofmann clathrate. White circles represent the transition metals in the +2 valence state that assume octahedral coordination; the large black circles are transition metals in the square planar configuration. The small black circles occupying the octahedral sites are NH_3 (hydrogens not shown). The dot circles represent the locations of enclathrated molecules within the basal space. The crystal lattice indices A, B, and C are typical directions of visualizing the unit cell (figure adapted from Iwamoto).⁶

The Hofmann clathrates form a type of cage structure with octahedral coordinated metals. The formula is referred to generally as $\text{M}(\text{M}_x)_2\text{M}'(\text{CN})_4$, where M refers to transition metals in the +2 valence state such as iron(II), manganese(II), nickel(II), cadmium(II), cobalt(II), copper(II), and M' refers to transition metals in a four-coordination square planar position. M_x are NH_3 molecules that assume a trans-configuration above and below the plane. In the original work there were aromatic molecules referred to as enclathared that are trapped in the open space between the

layers. The c- dimension of the lattice is affected by the size and identity of the guest molecule.⁶ Rayner and Powell discovered that these guest molecules could be substituted, forming a new complex.²⁶ In 1981 Iwamoto began hydrating the Hofmann clathrates.⁶ Preparation of hydrate forms takes place with an aqueous solution in place of an ammonia solution. In this network, additional waters of hydration were contained in the structure. The general formula was adapted to show these hydration states: $M(H_2O)_2M'(CN)_4 \cdot y(H_2O)$. The hydrated clathrates were in the orthorhombic phase.²⁵

The complete crystallographic structures have been solved for $Fe(H_2O)_2Ni(CN)_4 \cdot 4H_2O$, $Mn(H_2O)_2Ni(CN)_4 \cdot 4H_2O$, $Ni(H_2O)_2Ni(CN)_4 \cdot 4H_2O$, $Co(H_2O)_2Ni(CN)_4 \cdot 4H_2O$ and $Cd(H_2O)_2Ni(CN)_4 \cdot 4H_2O$.^{25,27-29} The crystallographic data is presented in the Appendix for these complexes. A study of the hydration states of some of these materials is presented in this dissertation. There is strong indication that the hydration state affects the framework by inducing a curvature to the sheet. This curvature was predicted by Nash using molecular dynamics simulations and was confirmed using X-ray powder diffraction techniques.³⁰ The bond distances in the network vary slightly depending on the identity of the transition metals. Bond distances are affected by the curvature of the sheet. The extent of curvature may be related to atom identity in the structure. The stability of the hydrated states may also depend on the curvature. The molecular modeling conducted in this study sought to find the relationship and importance of curving to the stability of the hydrated state. Stability plays an important role in the ability to exfoliate the layers. A relationship between hydrated structure and exfoliation in smectic materials has been studied.^{23,31}

The formation of a 2D material from these frameworks has been explored by Nash.²⁵ Properties of 2D forms of materials typically differ from their parent 3D structure and often provide unique material benefit. The underlying principle of separation is the substitution at the coordination sites with a larger organic molecule in a simplified diagram in Figure 2. This approach mimics methods utilized in the organoclay industry and the study of modified clay technologies.³²⁻³⁶ One such organic molecule that has demonstrated excellent intercalation is n-dodecylpyrrolidinone (DDP). The structure of this organic molecule is a five member ring with a nitrogen and an adjacent carbonyl group. Bonded to the nitrogen site is a 12 carbon saturated chain.

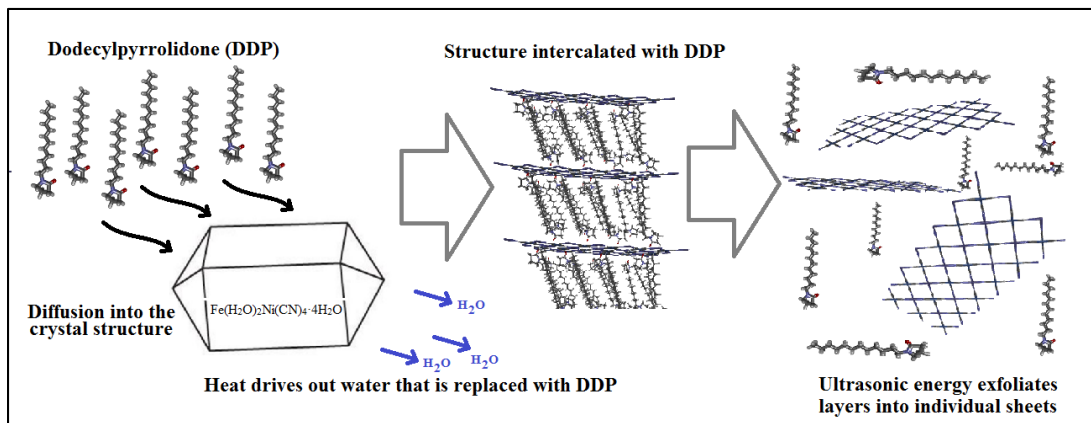


Figure 2. Simplified mechanism for exfoliation of 3D structures into 2D sheets. The organic DDP molecules replace structural water in the hydrated crystal by intercalation. The increased distance between layers allows for separation into exfoliated sheets.

This structure combines a strong dipole and a hydrogen bonding moiety. An environment of weak van der Waals interlayer interactions stabilizes the network at large basal distances. Our previous work in 2004 demonstrated that DDP was effective at intercalation of montmorillonite clay.³⁷ After the organic has intercalated into the

material the energy to achieve exfoliation is lowered. Exfoliated nanosheets of $\text{MnNi}(\text{CN})_4$ and $\text{CoNi}(\text{CN})_4$ were obtained by Nash using these methods and were imaged by scanning electron microscope (SEM) are in Figure 3. It was important to obtain data that verifies that these 2D sheets remain relatively flat after exfoliation and have enough rigidity to withstand deposition onto a substrate without wrinkle formation or stress fractures. Manipulation and arrangement of atomistically thin individual sheets was one of the biggest challenges in this research.

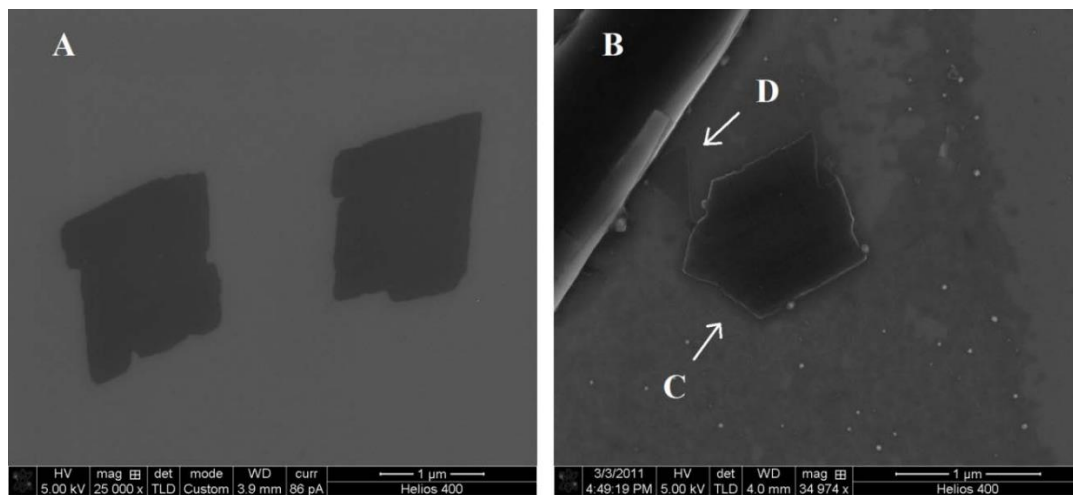


Figure 3. SEM images of transition metal cyanide nanosheets. An SEM image of (A) two similar single $\text{MnNi}(\text{CN})_4$ nanosheets is shown along with an image of (B) $\text{CoNi}(\text{CN})_4$ nanoparticles. The (C) large sheet in the middle is a multilayer structure, the (D) smaller triangular shaped piece next to it appears to be a single molecular layer.²⁵

1.3 Ion Selective Membrane for Desalination

We speculate that the framework of the 2D nanosheets in these cyanide-bridged transition metal complexes could be ion selective. The square grid structure resulting

from the framework of square planar and octahedral coordination atom sites in the corners with cyanide bridge ligands connecting these corners forms openings in the 2D sheet. An opening between atomic radii of ≈ 0.3 nm exists in the center of each square as seen in Figure 4. If the performance of this material as a filter media proves effective, applications in separations, desalination, and purification could benefit.

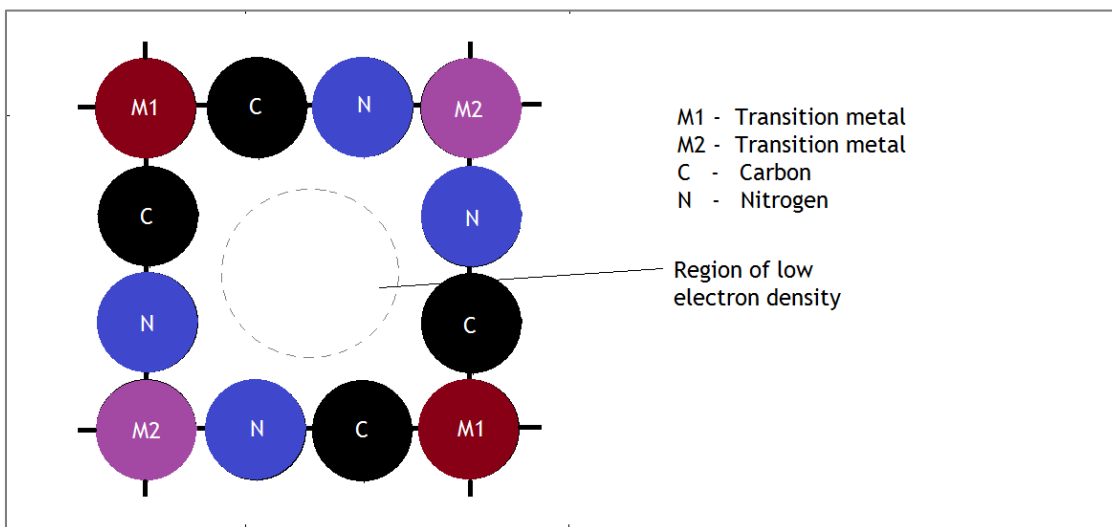


Figure 4. Diagram showing square framework of atoms in the single layer. The framework creates a small opening between atomic radii that water molecules can move through. The circles shown are not to scale.

Some of the applications where this technology could make improvements are; ion selective biomembranes, chemical reaction buffer membranes, gas purification membranes, and reverse osmosis (RO) membranes.³⁸⁻⁴⁶ The inherent benefit of an atomistically thin membrane material is that it provides function at lower energy costs, lower materials expense, and it is also possible that the metals in the membrane provide an antifouling advantage.

One of the most exciting potential applications for this material is as a new type of RO membrane for desalination. Most of the world's water is saline and is unsuitable for use for many applications including agriculture and drinking water. Human life is not possible without freshwater and no other substance can be substituted. Water supply is a rapidly growing global problem with a dire need. The world must obtain an increasing supply of freshwater to sustain its future populations.⁴⁷ The world's total population is near 7.35 billion persons with an aggregate annual growth rate of 1.7%.^{48,49} The projected population will exceed 8 billion by 2025.⁴⁹ Geographic regions with the largest segments of this growth are of significant interest. The highest populations and highest rates of growth are found in regions that are desert, or along coastlines.⁵⁰ It is also those geographic areas that have the lowest available freshwater resources.^{51,52} Figure 5 shows a global map of water scarcity identifying where water is difficult to come by.

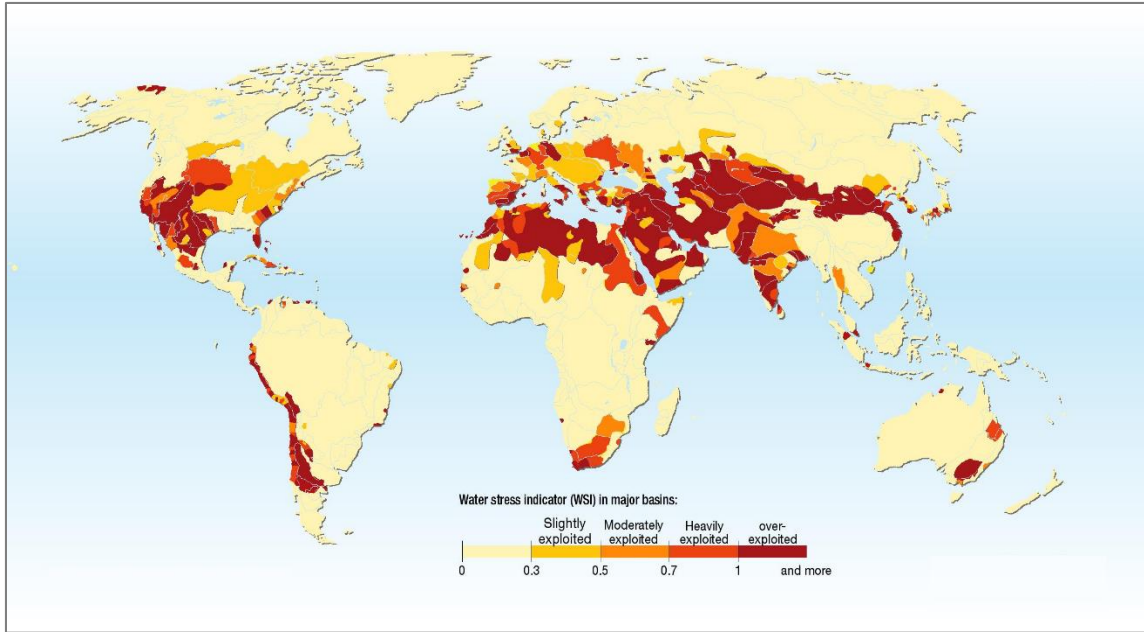


Figure 5. Water Scarcity Index. The relative water stress around the globe.⁵³

The world's oceans contain 97.5% of all water on the planet.⁵³ The saline water of the ocean is unacceptable for human consumption. Most industrial uses that require water cannot use saline water either. This enormous supply of water can be used to supply all the water needs on the planet through the use of effective desalination technology. Desalination of seawater has a long history and has been demonstrated as an important supply of freshwater in many parts of the world.^{54,55} The economics of desalination become the limiting factor. The cost of desalinated water is too high for many localities, leaving it an unviable solution at present.⁵⁶ New technologies and processes for desalination of seawater have promise for reducing cost and broadening the application into communities where it is inaccessible. Problems related to water scarcity, including widespread disease and armed conflict surrounding control of water

supplies, might be solved with higher efficiency process and materials in seawater desalination.^{56,57}

Modern desalination is accomplished commercially by a number of well-developed technologies. These technologies are organized into four broad categories: distillation based methods, ionic methods, crystallization techniques, and membrane related processes.^{45,58,59} There are examples where combinations of these methods are employed with some success. The development and use of these methods runs somewhat parallel to each other. Membrane technology has greatly outpaced the others in terms of commercial application since the 1990's.⁵⁴ The scope of this text deals with membrane methods of desalination.

Membrane methods separate ions from water through the use of a semipermeable membrane. This membrane allows water to flow through while restricting ions from passing. The most popular method of seawater desalination today is reverse osmosis membrane desalination or seawater RO (SWRO). This technology uses pressure to overcome the osmosis principle. Osmosis is a natural phenomenon where the flow of water molecules through a semipermeable membrane (impermeable to solute) results when the solute concentration on either side of the membrane differ from the other side. The flow is the result of pressure developing when molecules of water move toward the side with the greater solute concentration in an effort to reach an equilibrium state. The hydrostatic force required to maintain this condition is called the osmotic pressure. This

pressure is a colligative property dependent on the concentration but not molecular identity.⁶⁰ Figure 6 shows a diagram of osmosis across a semipermeable membrane.

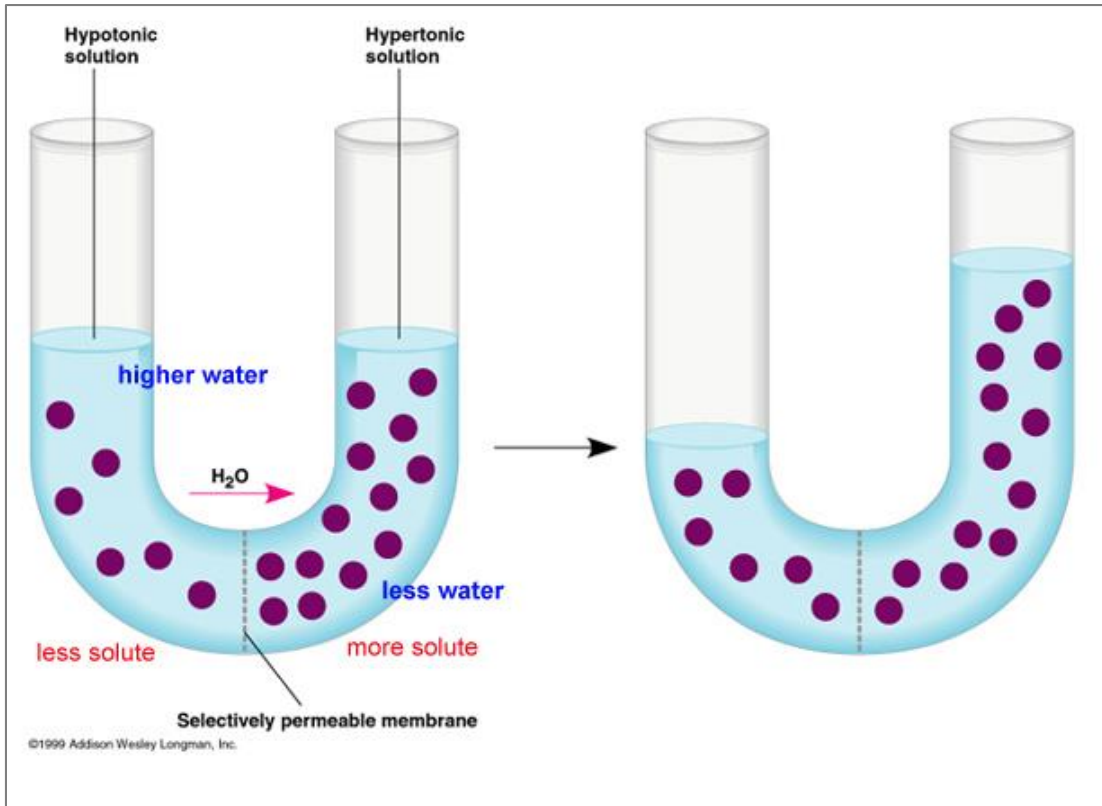


Figure 6. Osmosis of water through a semipermeable membrane. Water moves from lower concentrations of solutes to higher concentrations without input of energy.⁶¹

Reverse osmosis is accomplished when pressure is applied to the high solute side of a semipermeable membrane and the osmotic pressure of a system is exceeded. This causes the solvent to flow opposite the normal osmotic direction. The water molecules on the side of the semipermeable membrane with the higher solute concentration now flow across to the side with the lower solute concentration. The

pressure required is a function of the concentration difference so as the high solute side increases in concentration the osmotic pressure will increase.⁶¹ It is not possible to completely separate water from solute species since the osmotic pressure cannot be maintained at high concentrations.

Pressure is needed to drive water across the membrane is a function of membrane thickness. Water flux contributions to pressure requirements are minimized by thinner membranes. Generating high pressure requires energy input. SWRO desalination has to be more efficient to be a widespread, affordable source for fresh water. Other costs include the equipment and facilities, but the largest costs are membrane costs. This is because RO membranes have short life spans with the principle cause being fouling.⁶²⁻⁶⁴ Chemicals and organisms buildup on the functional surface of the membrane and reduce water flux. This drives the pressure requirements higher. The effects of fouling has been reduced by the use of cross water flow across the membrane. This greatly reduces the excess pressures and allows fouling agents to flow away from the surface. Testing and development of membranes is often accomplished in dead-end flow where the flow is perpendicular to the membrane surface.

The membrane material most commonly used in today's SWRO applications is thin the thin film composite (TFC) membranes. Figure 7 shows the layered structure of TFC membranes. The membrane is constructed by depositing a polyamide layer over a polyethersulfone or polysulfone porous layer which has been deposited on a non-woven fabric support layer. The polyamide contains a high density of nanoscale pores and is

greater than 100 nanometers thick but generally less than 200 nanometers thick. The underlying porous layer of polyethersulfone or polysulfone is typically 50 micrometers thick that supports the thin polyamide film. The fabric support layer can be over a millimeter in thickness. The fabrication of these membranes is done by interfacial polymerization of the layers and can be expensive. TFC membranes are susceptible to damage in acidic environments and elevated free chloride concentrations. TFC membranes also suffer from compaction problems under high pressure.^{59,65}

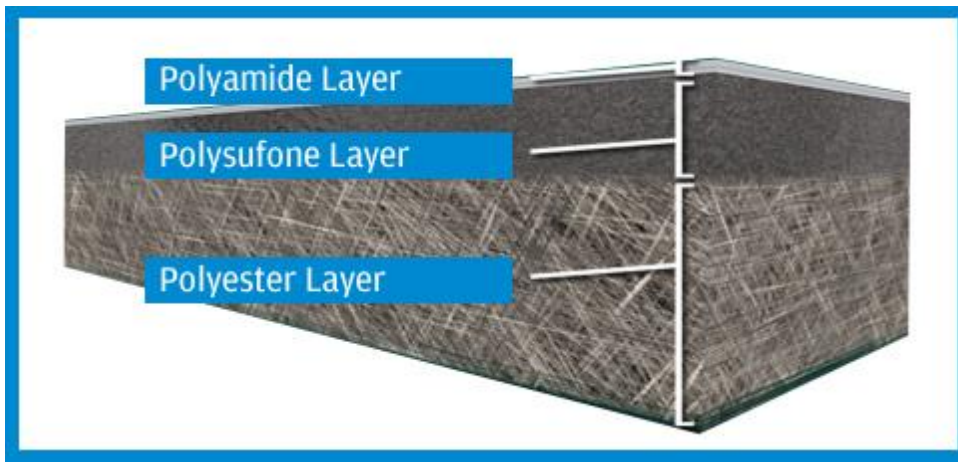


Figure 7. Typical thin film composite membrane. The ion selective, polyamide layer at the top of the image is 100 nm to 150 nm thick.⁶⁶

Numerous methods to improve TFC membrane technology by chemical surface treatments, nanocomposite additives, and polymer improvements are reported.^{42,44,45,58,59,67-73} Table 1 compares water permeability, salt rejection and fouling susceptibilities for current commercial technologies and proposed future technologies. TFC membrane research in reducing the thickness of the ion selective layer is lacking in the science.

Table 1. Comparison of future RO membrane technology performance to today's leading technology.

Technology Type	Water Permeability (L/cm ² /day/MPa)	Salt Rejection %	Fouling Susceptibility	Reference
Salt Water RO Thin Film Composite	0.05	99.2	High	Pendergast
MFI Zeolite NTFC	0.1	90	High	Jeong
High flux RO	0.5	98	High	Zhao
CNT –Embedded films*	40	96	Mid	Corry
Nanoporous Graphene *	80	99.9	Mid	Cohen-Tanugi
Transition Metal Cyanide Bridged Membranes *	130	99.9	Low	

*Theoretical – Data based on simulation modeling

The ranked effectiveness of RO membranes is by salt rejection and water permeability. The best membranes have high water permeability and high salt rejection. Flux is the movement of water through a membrane. It is typically expressed as volume per area per unit of time and typical units are gallons per square foot per day (GFD or GSFD) or liters per square meter per hour (l/m²/h). The flux of RO membrane is directly proportional to temperature and pressure.⁷⁴ Water permeability measurements incorporate pressure into the equation. Temperature is assumed to be 20 °C (293.15 K). The amount of total dissolved solids that pass through a given area of membrane per unit of time is the salt flux. Salt flux is dependent on the concentration gradient and not driving pressure. Therefore an increase in the pressure will result in a decrease in the

concentration of salts in the permeate. The pressure can be increased in order to dilute a constant amount of salt with more pure water resulting in higher flow. This requires even higher pressure as the concentration increases to maintain a level above that of osmotic pressure. Flux across a membrane scales inversely with the membrane's thickness. Minimizing this distance is a promising approach to improving RO membrane efficiency.

Two promising technological approaches to improve RO membranes are the use of carbon nanotubes (CNT)⁷⁵⁻⁷⁸ and graphene, a single layer thickness sheet of continuous carbon atoms.^{79,80} Graphene is impermeable to water. The material must be engineered to contain holes to allow water flow.⁸⁰⁻⁸³ The permeability of membranes is highly dependent on the pore density. This presents a problem for CNTs because close packing of CNTs is difficult to achieve.^{76,82} Application of nanoporous graphene sheets with high pore density compromises mechanical strength. Stability is inversely influenced by increasing the pore density. The 2D cyano bridged transition metal nanosheet framework represents a fishnet-like structure with maximum pore density as well as being atomistically thick. The average area per pore is 25 \AA^2 with $15-18 \text{ \AA}^2$ having little or no electron cloud density. These two advantages predict that the application of this nanosheet material in RO membranes result in a highly efficient membrane. There have been six mechanisms proposed to explain water permeability and salt rejection in nanoporous membranes: size exclusion, dehydration effects on the cage structure around ionic species, charge repulsion, specific pore interactions (like

biological channel mechanisms), interactions of solutes with the pore's chemical structure, and entropic differences.⁸⁴

1.4 Magnetic Properties

The field of molecular based magnets is growing from the fundamental point of view and from the potential applications of these materials. Magnetism at the molecular level behaves identically to magnetic substances such as transition metal, rare earth or electromagnetic magnets.⁸ What makes molecular magnets different from conventional metallic magnets is that metal atoms containing d or f shell electrons don't have to be adjacent to one another. The atoms containing unpaired electrons can be separated by other atoms or organic moieties.⁸⁵ Some of the materials studied in this text contain transition metals with an unpaired electron in the d shell. These magnetic centers are separated by cyano ligand bridges and are relatively distant from one another. Magnetism of this type originates from spin crossover (SCO) where electron spins influence the spin characteristics in other atoms. The distance between these centers is influential on how effective the coupling is and the magnetic moment measurable in the bulk. SCO materials exhibit bi-stability, or stability in paramagnetic and diamagnetic phases, at the molecular level and could be utilized as a switchable material. One approach to utilizing this would be to manipulate the distances between transition metals thereby regulating SCO.⁸⁶ The spin coupling mechanism originates from thermodynamically competing spin states (high vs. low).⁸⁷

Previous studies of the cyanide-bridged transition metal materials have shown them to have these magnetic properties in the 3D structure.^{9,16,86} Two of these, having the same transition metal type, both having +2 valence state, simultaneously exhibit two different magnetic properties.⁹ When this phenomenon is superimposed with the discovery that these transition metals can form octahedral coordination and square planar coordination in the same framework this behavior is worthy of exploration. Two applications; molecular magnetic memory devices and molecular switches, could be of commercial interest.

Nash *et al.* performed density functional theory calculations to predict the magnetic properties of the $MNi(CN)_4$ planar sheets for $M=Ni, Zn, Mn, Fe, Co,$ and Cu .³⁰ Their results indicate higher magnetic susceptibility in the $FeNi(CN)_4$ and $MnNi(CN)_4$ than in the others.³⁰ It was proposed that the $Ni_2(CN)_4$ material exhibits purely diamagnetic and insulating character. In systems where even number d-electrons exist, the system is either antiferromagnetic or diamagnetic, this is likely due to electron pair interactions cancelling spin coupling. In the odd numbered d-electrons a stable ferromagnetic property was exhibited.³⁰

The magnetic moment of these materials has been determined using a vibrational sample magnetometer (VSM). Saturation magnetization (M_{sat}), remanence (M_r), coercivity (H_c), and the energy product (BH_{max}) can all be obtained for the material in this instrument.⁸⁸ Low temperature effects can also be measured. Low temperature Curie points can be identified on magnetometers operating at low temperature. BH_{max} is

determined from the second quadrant or demagnetization curve of the material where the curve is recorded starting at remanence M_r and ending at the coercivity H_c .⁸⁸ Remanence is the magnetic memory of the material and coercivity is a measure of reduction in magnetic sensitivity.⁸⁸

CHAPTER 2

MOLECULAR DYNAMICS SIMULATIONS

2.1. Introduction to Molecular Dynamics Simulations

Computational analysis ranging from macroscale modeling to atomic simulations can facilitate the advancement of research. Predicting laboratory results in advance of bench work saves time and money. Simulations are used to develop research methods to streamline the scientific process. Computer models help explain phenomena and improve understanding of mechanisms and processes. Many fields such as semiconductors, biochemistry, medicine, polymer materials, energy technology, transportation, and other institutions now benefit from computational research.⁸⁹⁻⁹⁶

There are several computational methods that are employed in research and development that cover different timescales and dimensional scales. These methods model different aspects of behavior from quantum mechanical analysis to molecular dynamics, mesoscale modeling and continuum domains.⁹⁷ Figure 8 explains the relationship of different computational methods to the physical scale and time scale of materials and their movement being studied.

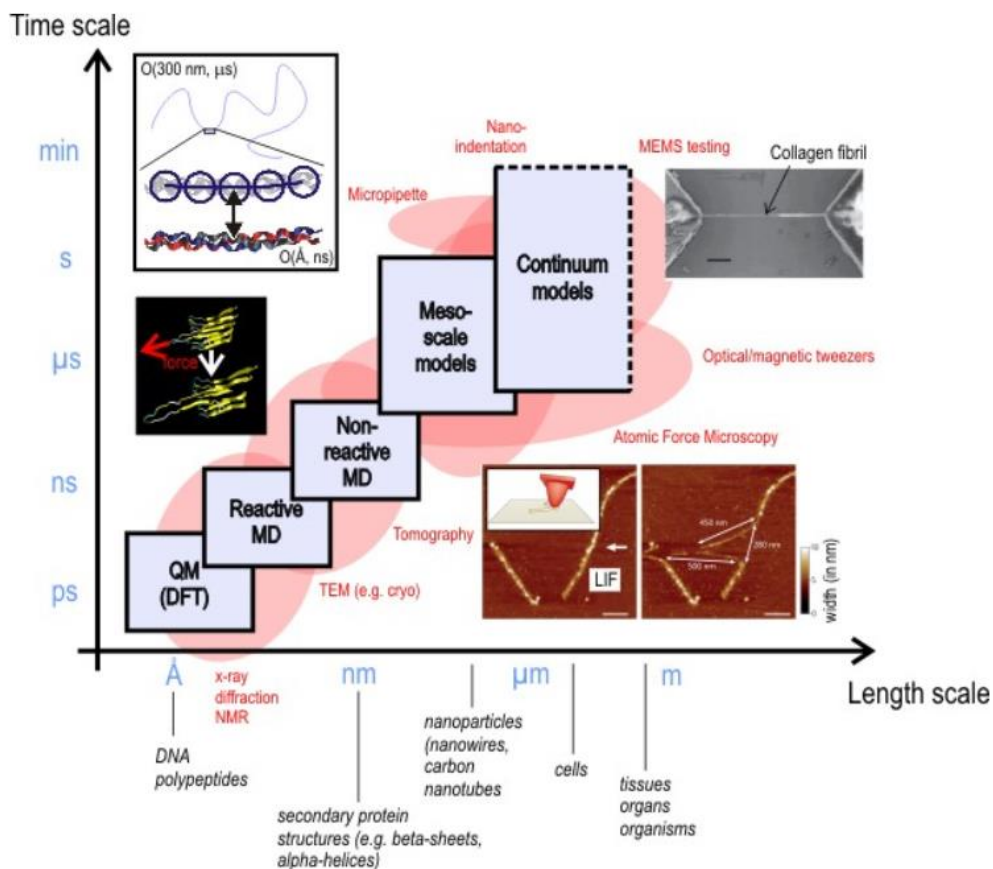


Figure 8. Simulation Tools – Time vs. Length scale. Different types of simulation tools are used for various scales of evaluation. The scale of time changes with size.⁹⁷

Quantum mechanical methods such as density functional theory (DFT) and quantum Monte Carlo simulations are used to model electronic properties and quantum effects on molecular interactions.⁹⁸ Molecular dynamic (MD) simulations model atoms, their interactions, and the forces they encounter. MD is divided into reactive modeling and non-reactive modeling which simulates interactions instead of chemical reactions. MD is a Newtonian approach to modeling motion with respect to finite time intervals. MD simulations are particularly useful at predicting chemical behavior in established conditions.⁹⁹ Mesoscale programs such as thermodynamic Monte Carlo programs and *ab*

initio molecular dynamic simulations are used where quantum mechanical approximations take over because classical mechanics are inaccurate.¹⁰⁰ Continuum simulations are used to model environmental scale behavior like fluid dynamics.^{99,101} Other simulations such as Finite Element Method (FEM) are used in engineering to model material strength and other performance behavior.¹⁰²⁻¹⁰⁵ The use of modeling in plant design, manufacturing, and economics improves the cost effective commercialization of materials.^{106,107}

The computational methods employed in this work are MD simulations. These rely on classical mechanics and physical constraints. As with any modeling, the key is to understand the limitations and assumptions to make realistic approximations that are based in scientific knowledge. The researcher must recognize when erroneous data is generated by either input error or limitations in the software that result in bad data. This understanding requires considerable time and patience to gain the skills to operate models successfully and to achieve meaningful outcomes. This implies there is a critical human component that is essential to successful modeling.¹⁰⁸

2.2. Model Construction

Molecular modeling was performed using Cerius² by Accelrys®, Inc. running in UNIX operating system on a Silicon Graphics platform. A Universal force field (UFF) module was used in all molecular simulations. The UFF is a full periodic table force field. It was designed to improve molecular modeling by including hybridization

dependent atomic bond radii for all elements, improvements in hybridization angles, and a better van der Waals parameter model based on Lennard-Jones potentials. It introduced torsional and inversion barriers and utilized effective nuclear charges. The UFF force constants can be compared to those of AMBER and CHARMM fields.^{109,110} All dynamics simulations performed utilized the Nosé-Hoover thermostat with constant number (atoms), volume, and temperature (NVT). The NVT ensemble is canonical and adds an additional degree of freedom to the Hamiltonian.¹¹¹ The endothermic and exothermic processes are evaluated in a realistic manner. Pressures can be responsive to the ideal gas law without effecting the motions of atoms.

Periodic models of the structures were created by entering the fractional coordinates of the atoms found by single crystal X-ray diffraction into a unit cell using the crystal builder module in Cerius². Models were built of the different cyanide-bridged transition metal sheet frameworks to assess the accuracy of the model. A force field was used to predict the atomic bond distances and the size of the unit cell and other crystallographic predictions. Models of $\text{Fe}(\text{H}_2\text{O})_2\text{Ni}(\text{CN})_4 \cdot 4\text{H}_2\text{O}$, $\text{Mn}(\text{H}_2\text{O})_2\text{Ni}(\text{CN})_4 \cdot 4\text{H}_2\text{O}$, $\text{Ni}(\text{H}_2\text{O})_2\text{Ni}(\text{CN})_4 \cdot 4\text{H}_2\text{O}$ and $\text{Cd}(\text{H}_2\text{O})_2\text{Ni}(\text{CN})_4 \cdot 4\text{H}_2\text{O}$ were built using crystal data obtained by Nash.^{25,30} Hydrogen atoms were added to the water molecules in the model structure. The model built for $\text{Cd}(\text{H}_2\text{O})_2 \text{Ni}(\text{CN})_4 \cdot 4\text{H}_2\text{O}$ had an unexpected problem with projecting the cadmium atoms as octahedral. This was thought to be an error with the UFF parameter file for geometric projections for the cadmium atom. When assigned as octahedral the Cd atoms in the model exhibited tetrahedral angles when energy minimization was performed. The modeling study of that material

was abandoned. After construction, a refinement of charge equilibration (charges are assigned to all individual atoms in the model) and energy minimization was performed.

The model structure and bond distances predicted vary from the crystallographic data. These differences are small and considered negligible in the study. The largest deviations come from the octahedral coordinated transition metal bond with nitrogen. The hydrogen bonding network in the nearby waters of hydration likely affect the neighboring bond more than the model predicts thus the model shortens the length of that bonding.

The models of individual sheets were combined to create stacked sheets of cyanide-bridged transition metal frameworks to build the 3D structure of the clathrate-like complexes. This network model shows the interactions and placement of water in the hydrated complexes. Water placement was performed based on the literature and the work of Nash *et al.*³⁰

Stacked sheets of cyanide-bridged transition metal complexes were modeled with and without waters of hydration. Nash reported the curving of sheets in the hydrated state as evidenced in some of the single crystal XRD solutions. He found that dynamic simulation predicts a flattening of the dehydrated sheets with a reduction in the basal layering. This is consistent with other layered materials when dehydrated.¹¹²⁻¹¹⁴ Nash found that as the material is dehydrated the curvature of the sheets in the $\text{Fe}(\text{H}_2\text{O})_2\text{Ni}(\text{CN})_4 \cdot \text{H}_2\text{O}$ was shifted relative to the layer above or below prior to complete

flattening.²⁵ Figure 9 demonstrates the curvature and shifting of the sheets within the unit cell during dehydration. This curvature precedes flattening of the sheets and a reduction in the interlayer space between the nanosheets. Red spheres represent oxygen atoms of water. Hydrogen atoms are not shown. Upon complete dehydration, flattening of the sheets is predicted and supported by XRD data. Models for membrane studies were presented as flat to simplify the modelling and avoid false indications of increased energy caused by bond angle crowding.

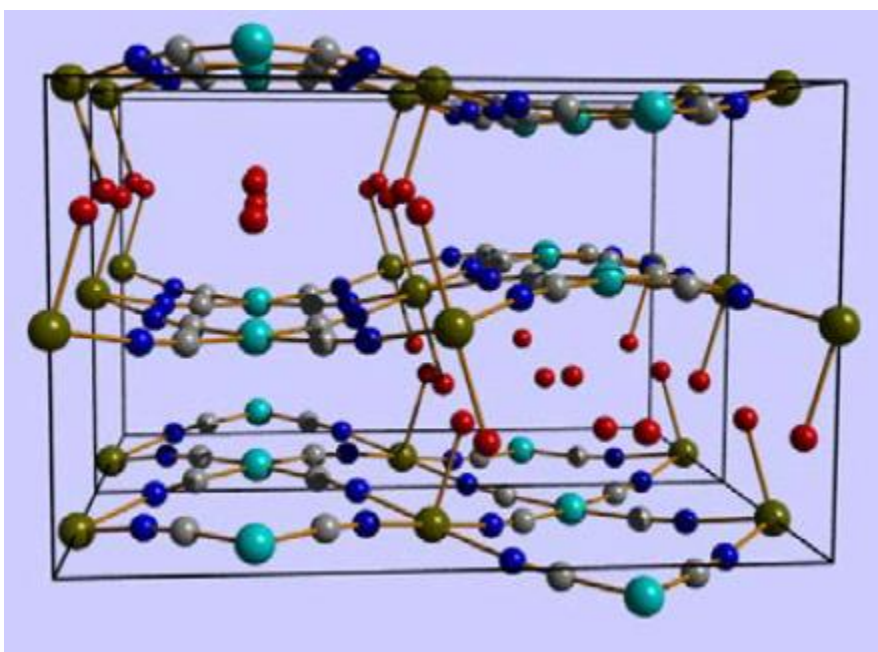


Figure 9. Partially dehydrated $\text{Fe}(\text{H}_2\text{O})_2\text{Ni}(\text{CN})_4 \cdot \text{H}_2\text{O}$ structure. The curvature and shifting of the layers create uneven pockets where water remains in the monohydrate structure prior to dehydration.³⁰

The model of $\text{Fe}(\text{H}_2\text{O})_2\text{Ni}(\text{CN})_4 \cdot 4\text{H}_2\text{O}$ was minimized and a comparison was made between model bond lengths and the crystal data. The difference was consistent with findings presented by Nash *et al.*³⁰ Crystallographic data for $\text{Ni}(\text{H}_2\text{O})_2\text{Ni}(\text{CN})_4$

$\cdot 4\text{H}_2\text{O}$ was obtained from Mathey *et al.*²⁸ Additionally, $\text{Co}(\text{H}_2\text{O})_2 \text{Ni}(\text{CN})_4 \cdot 4\text{H}_2\text{O}$ and $\text{Pt}(\text{H}_2\text{O})_2 \text{Ni}(\text{CN})_4 \cdot 4\text{H}_2\text{O}$ were evaluated in models but not cross referenced to actual crystallographic data.

The objective was to show that the models are accurate and represent the material's framework structure with approximate bond lengths. Based on the examples where crystallographic data is presented for comparison, it is expected that the other models are close in value to crystalline data. The dehydrated structure represents the ideal configuration and simplifies the study of water passage. In the dehydrated state flattening of the structure occurs. This was confirmed by building sheets without water in a completely planar configuration to model a constrained sheet as if it were on a flat support layer. Figure 10 shows a flat sheet of dehydrated $\text{FeNi}(\text{CN})_4$ with green atoms representing nitrogen atoms and orange atoms representing iron atoms. The iron atoms are modeled as octahedral and they will coordinate with ions during the simulation.

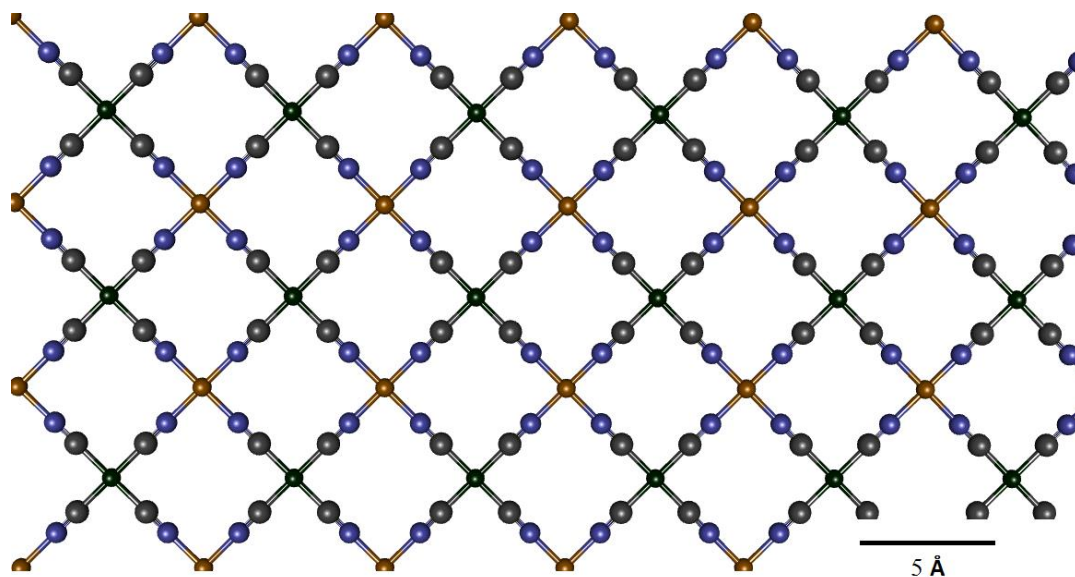


Figure 10. Model of flat sheet of dehydrated FeNi(CN)₄. Blue atoms are nitrogen of the cyano bridge group. They are bonded to iron (orange). The carbon atoms (grey) bond to the nickel atoms (green).

A study of atom distances compared the projected bond lengths in the curved structure versus the flat structure. Differences in the interlamellar space from transition metal identity is significant in the stability of the hydrate structure. This relates to the water interactions between the layers and the variation seen with the identities of the metal atoms. This aspect is investigated experimentally in Chapter 3 and the result discussed in Chapter 4.

Extensive work has been accomplished by Cohen-Tanugi and Grossman at the Massachusetts Institute of Technology on computational analysis of nanoporous graphene for RO desalination.^{80-82,115,116} Graphene is impermeable to small gaseous molecules.⁷⁹ The simulation of graphene as impermeable to water has also been demonstrated. A porous structure can be engineered into the sheets allowing for water

permeation and ion selective behavior.⁸⁰ This has prompted the inclusion of the modeling of these materials in this work to compare with the cyanide-bridged transition metal complexes. A comparison can be made between the model systems that indicate efficiency in water permeability and salt rejection.

A graphene sheet model was constructed. This is a continuous 2D sheet lattice of carbon atoms covalently bonded to 3 neighboring carbon atoms with σ -bonding. An additional π -bond out of plane forms the sp^2 hybridization. Atoms are 1.42 Å apart with bond angles of 120°.¹¹⁷

Periodic models were constructed for both pristine and several porous graphene sheets with different size pores. Because the carbon atoms bordering the holes are missing a σ -bond, the edges must be satisfied with some type of moiety. In these models hydrogens, hydroxyls or a combination of alternating hydroxyl groups and hydrogens forms the edge of the pore. These models represent hydrophobic pores with the hydrogens and hydrophilic pores with the hydroxyls. These structures were comparable to the experiments of Cohen-Tanugi and Grossman.⁸² Figure 11 shows two stacked graphene sheets. The upper sheet is pristine while the lower sheet contains a hydrophilic pore structure in the center. These models were refined and minimized in the same manner as the cyanide-bridged transition metal sheets. Pore size in nanoporous graphene also has a significant effect on both water permeability and salt rejection rates. These pore characteristics have been studied and the best overall size was chosen to be included in this study.

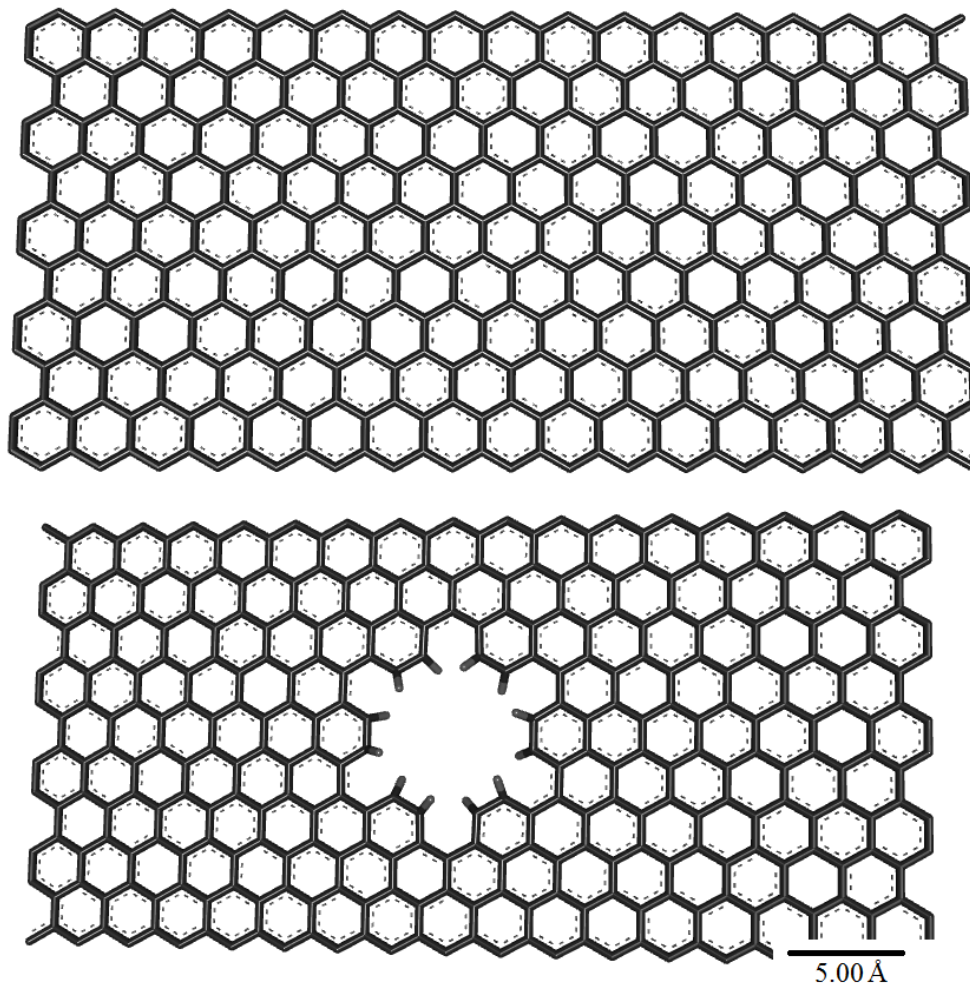


Figure 11. Graphene and nanoporous graphene sheets. The upper sheet is the impermeable pristine sheet and below is a perforated graphene sheet with hydrogenated edge modification around the pore.

2.3. Models of Water Permeability

This modeling was performed to investigate the effectiveness of individual sheets of these complexes as membranes for ion selectivity and SWRO desalination. The mechanics and energy profiles for water molecules permeating through the 2D framework was studied. To accomplish this, water molecules would need a force applied

in the form of pressure. This was accomplished in the MD simulation by creating a closed system with a piston that could be used to control the available volume for water or ionic species to occupy on one side of the membrane being tested. Figure 12 shows a basic drawing of the piston model setup. Pristine graphene was used as the piston face since it is impermeable to both water and any ions present in the model.

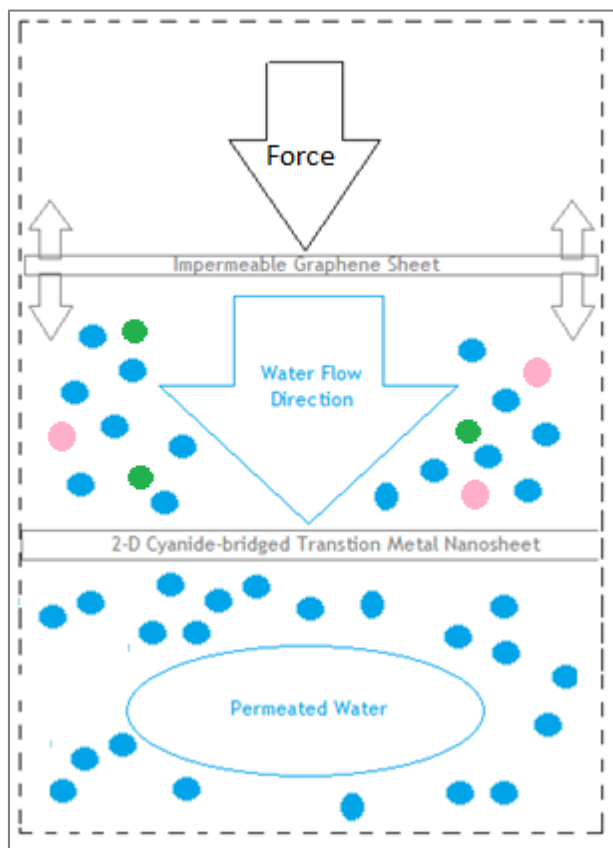


Figure 12. Diagram of piston model used to simulate pressure. The piston provides hydrodynamic pressure to the system forcing water molecules to move toward, and interact with atoms of the membrane.

Periodic models were used in this study. This means that although the model was infinite in all directions periodic cells formed closed systems. If atoms moved laterally

beyond the unit cell they were transposed to an identical coordinate on the opposite side of the cell. Because of this, the model was treated a closed system. By reducing the available volume between the piston and the test sheet a force vector was created on the water and ions within the model. Initially the force was directed down by atoms in proximity but as the space was reduced around individual atoms, interactions increased and force vectors pointed toward adjacent available space. This mechanism was accomplished stepwise with a combination of dynamic simulations of small atomic movements and bonding movement such as stretching, compression or bending. The dynamic movement was combined with energy minimization movements and calculations. This accomplished the lowest energy states for the model based on atomic interactions and positions. When the available volume of the model was such that atomic interactions increased and atoms were unable to maintain low energy distances, pressure on each atom increased and the total energy of the closed system increased. Any pores in the test membrane material offer a place for the compressed water and ions to go that will minimize the system energy and pressure. In this action it was possible to determine the permeability of the membrane.

Water molecules were constructed in a new model, charges were assigned and energy minimized. The water was then copied molecule-by-molecule into the test model. The models either consisted of 192 water molecules in dehydrated sheet models or 206 water molecules when waters were coordinated to octahedral centers. Models of both scenarios were built. The computational power ultimately limits the number of atoms present in the model. The time needed for calculations also increases with the

number of atoms. The size of the model was attributed to these limitations. A similar method was used to include sodium ions and chloride ions. Charges were equilibrated for the model after all water and ions were loaded. The relative number of ionic species in the bulk of the water was calculated based on the average salinity of seawater (total dissolved solids of 35 g/L).¹¹⁸ Some experiments were conducted without ionic species and some were run with excessive ionic content to simulate brine concentrations of up to 350 g/L.

Initial positioning of the piston face (graphene sheet) was such that there was excess volume between the piston and the test membrane for the number of water molecules present. Water density calculations were performed to determine the predicted volume when permeation would likely occur. The open initial condition would allow water to compress in a more realistic way. Slow reductions by stepwise movements of the sheet acted to compress the water until permeation was achieved. The simulations consisted of a cycle of steps meant to allow a combination of dynamic simulation and energy minimization. The cycle also included the manual movement of individual molecules that have become locked in false-energy minimum states. Figure 13 shows the general cycle of steps in these MD simulations. The repetitive process is the most accurate way to model the system and avoid erroneous data. Identifying features and data values during the modeling cycle that appear suspicious or abnormal is critical to achieving good approximations. This cycle was utilized in all the models where the piston model of hydrodynamic pressure was used.

This method was used to evaluate water permeability in the cyanide-bridged transition metal 2D sheets and in pristine and porous graphene models. These experiments were considered to be bulk water / ionic experiments designed to look at water permeation as a function of the force applied by molecules pushing on and interacting with each other. The results are discussed in Chapter 4.

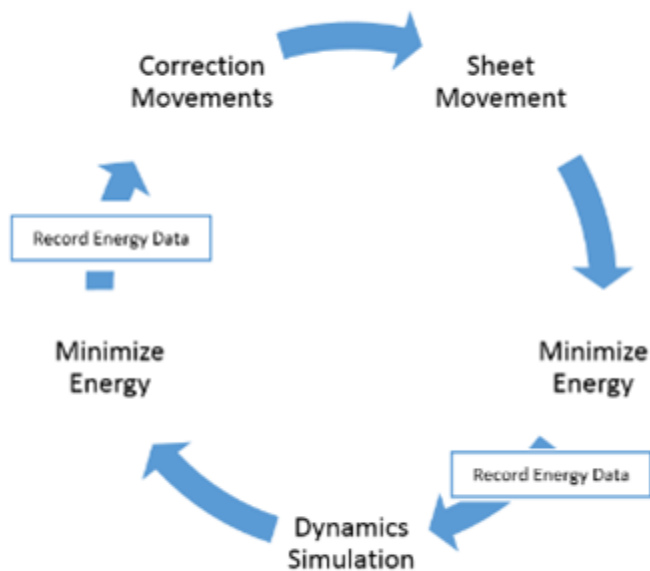


Figure 13. Cycle of the steps in MD simulations. The cycle contains two data collection points bracketing a dynamics simulation step. A correction movement step is included to identify and free molecules locked in a false energy minima configuration.

2.4. Models of Ion Selectivity

After collecting data on various models for determination of comparative water permeation, attention was turned to determining the ion selectivity of the pores. This can be thought of as the rejection of dissolved solids by the membrane and is a gauge of its filtration quality. In the water permeation models, the ions present were maintained above the membrane and not permitted to move through the pores. Here the ions were positioned so that they would encounter force vectors promoting their movement through the membrane. Dynamic simulation behavior of these ions and elevated energy data would semi-quantitatively predict the likelihood of ions transiting the membrane. Results were based on relative numbers of ions and water transiting the membrane. Figure 14 shows a model of water desalination. Sodium ions (pink) and chloride ions (green) are above a $\text{Co}(\text{H}_2\text{O})_2\text{Ni}(\text{CN})_4$ sheet with ions located near pore openings as water (red/white ball and stick models) transits the pores and moves below the membrane.

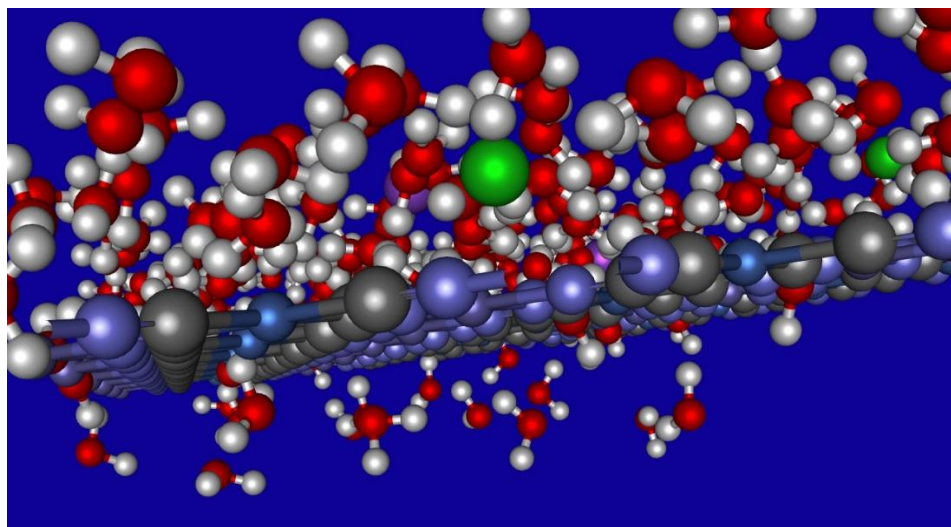


Figure 14. Periodic model of water desalination. Sodium ions and chloride ions are above a $\text{Co}(\text{H}_2\text{O})_2\text{Ni}(\text{CN})_4$ sheet with some water passing through. Ions are near the surface of the membrane but not occupying pores. Note that visualization of the graphene sheet is off. Pink and green spheres represent sodium and chloride ions respectively. Red/white ball and stick models represent water.

2.5. Energy of Pore Transit Modeling

Observations of water molecules moving through the pore structures revealed a pattern of orientation. Additional experiments were conducted to record the change in energy of a molecule as it approached the membrane, oriented to pass and then transited through the pore. This profile of energy could be compared within pore types and sizes and could also be compared to the nanoporous graphene pores. No piston model was needed for these experiments. A series of $\text{Ni}_2(\text{CN})_4$, $\text{Co Ni}(\text{CN})_4$, $\text{FeNi}(\text{CN})_4$, and $\text{Pt}_2(\text{CN})_4$ complexes were tested because these vary in pore size from small to large based on atomic radii. All are in dehydrated form so interactions are limited to atoms on the framework and the species being moved through. The model for testing water

consisted only of the test membrane and a single molecule of water. The sheet was fully constrained in the model and only the energy of the molecule was recorded as data. This is the energy of the water molecule interacting with atoms around the pore only. The molecule was positioned above the membrane directly above the pore where no atomic interactions occur. Energy was minimized and recorded. The molecule was subsequently moved closer to the membrane, energy was minimized and recorded. This step was repeated as the molecule approached, transited and moved away from the pore on the opposite side of the membrane. Similar experiments were conducted with sodium ions and chloride ions for comparisons and then repeated on models of nanoporous graphene sheets. Both hydrophilic and hydrophobic pore models were evaluated.

The water molecule aligned with one hydrogen pointing down, directly at the center of the pore. As the molecule transited the pore it tilted so that the opposite hydrogen is pointing straight up and perfectly aligned with the center of the pore. As the molecule moved away there appeared to be no specific orientation following the event. The water molecule was tested in all possible orientations and oriented itself identically every time. Additionally, experiments where the water molecule was positioned above a transition metal center or above the nitrogen or carbon of the cyano-bridge and moved toward the membrane results in the water molecule always repositioning at the center of the pore and orienting the same way to transit. When the experiments were conducted using sodium ions in the same manner, the energy values are higher suggesting difficult transit conditions. Similar experiments were conducted with sodium ions and chloride ions for comparisons.

CHAPTER 3

EXPERIMENTAL METHODS

3.1. Preparation Methods for Cyanide-bridged Transition Metal Complexes

Laboratory experiments began with the preparation of the clathrate-like 3D structure of the cyanide-bridged transition metal complexes. These were all produced in a hydrated form by synthesis in water. Three methods of synthesis were used to produce single crystal forms, precipitated powders, and interfacial sheets. Each method provides a different type of material. These materials have different properties and characteristics.

3.1.1. Single Crystal Growth Method

The single crystal growth method produces large single crystals by slow growth in water. This method was used by Nash *et al.* and is fully described in that publication.³⁰ A review of the method is presented and the experimental crystal growth setups using the method are reported. Large single crystals of the hydrated cyanide-bridged transition metal complex were grown by slow diffusion of reactants through a water bridge. A glass tube bent into a U-shape was inserted into rubber stoppers at each end such that ≈ 1.5 inches of the glass extended beyond the stopper. The glass tube and two standard clean test tubes were submerged in a bath of clean deionized (DI) water. All air was evacuated from the test tubes and the glass bridge tube. The stoppered ends were carefully inserted into the test tubes closing off the apparatus from air. The

assembly was removed from the bath with the bridge facing up. Figure 15 is a picture of the experimental tube apparatus.



Figure 15. Single crystal growth apparatus. A continuous water bridge is formed in the U-shaped tube and air cannot enter the bridge. Crystal growth can be seen in the bridge.

After the exterior surfaces of the assembly was dried off, the stopper on one side was withdrawn from the end of the test tube enough to insert a syringe. The syringe was used to remove a small amount of water, taking care not to reduce the water level below the end of the U-tube. A measured quantity of the water soluble potassium tetracyanonickelate(II) hydrate solid was carefully added through the small gap. The solid salt sank to the bottom of the test tube and the stopper was reinserted fully. The

process was repeated on the transition metal salt side in the identical manner using one of the forms of metal salts. The source information for all reagents used in this research can be found in the Appendix. All reagents were used as received. The loaded assembly was labeled and placed into an oven at 40 °C in a test tube rack. The crystal growth was monitored over a period of four weeks. Crystals were expected to form at the junction located at the top of the glass bridge tube after slow diffusion of the reactants. Table 2 shows the loadings for four experiments performed.

Crystal formation was not observed and air bubbles occupied the bridges of all but one of the samples. One of the samples had developed a crack in the bridge tube and leaked air. Minor discoloration occurred after two months but no large crystal growth occurred. The experiment was not repeated.

Table 2. Reactant loadings in single crystal growth in U-tube experiments. The loadings are stoichiometric to obtain equal molar concentrations on each side.

Target Crystal	Compound A	Amount (g)	Compound B	Amount (g)
$\text{Fe}(\text{H}_2\text{O})_2 \text{Ni}(\text{CN})_4 \cdot 4\text{H}_2\text{O}$	$\text{K}_2\text{Ni}(\text{CN})_4 \cdot x\text{H}_2\text{O}$	0.0885	$(\text{NH}_4)_2\text{Fe}(\text{SO}_4)_2 \cdot 6\text{H}_2\text{O}$	0.1662
$\text{Co}(\text{H}_2\text{O})_2 \text{Ni}(\text{CN})_4 \cdot 4\text{H}_2\text{O}$	$\text{K}_2\text{Ni}(\text{CN})_4 \cdot x\text{H}_2\text{O}$	0.11	$\text{CoCl}_2 \cdot 6\text{H}_2\text{O}$	0.0988
$\text{Mn}(\text{H}_2\text{O})_2 \text{Ni}(\text{CN})_4 \cdot 4\text{H}_2\text{O}$	$\text{K}_2\text{Ni}(\text{CN})_4 \cdot x\text{H}_2\text{O}$	0.0955	$\text{MnSO}_4 \cdot \text{H}_2\text{O}$	0.142
$\text{Ni}(\text{H}_2\text{O})_2 \text{Ni}(\text{CN})_4 \cdot 4\text{H}_2\text{O}$	$\text{K}_2\text{Ni}(\text{CN})_4 \cdot x\text{H}_2\text{O}$	0.1055	$\text{NiSO}_4 \cdot 6\text{H}_2\text{O}$	0.1222

3.1.2. Bulk Precipitation Method

The bulk precipitation method was used to produce small crystals. This method is fast and easy. It is not possible to obtain large single crystals by this method but the 3D structure of the cyanide-bridged transition metal complexes will form. These syntheses were carried out in DI water. Each of the two reactants is dissolved separately to form dilute solutions of approximately 2% by weight. Table 3 contains the reactant quantities for all of the experiments performed. Equal molar concentrations were used.

Table 3. Reactant loadings in the bulk precipitation growth method.

Target Precipitate	Compound A	Amount (g)	Compound B	Amount (g)
$\text{Fe}(\text{H}_2\text{O})_2 \text{Ni}(\text{CN})_4 \cdot 4\text{H}_2\text{O}$	$\text{K}_2\text{Ni}(\text{CN})_4 \cdot x\text{H}_2\text{O}$	5.923	$(\text{NH}_4)_2\text{Fe}(\text{SO}_4)_2 \cdot 6\text{H}_2\text{O}$	8.969
$\text{Co}(\text{H}_2\text{O})_2 \text{Ni}(\text{CN})_4 \cdot 4\text{H}_2\text{O}$	$\text{K}_2\text{Ni}(\text{CN})_4 \cdot x\text{H}_2\text{O}$	1.1599	$\text{CoCl}_2 \cdot 6\text{H}_2\text{O}$	0.6204
$\text{Mn}(\text{H}_2\text{O})_2 \text{Ni}(\text{CN})_4 \cdot 4\text{H}_2\text{O}$	$\text{K}_2\text{Ni}(\text{CN})_4 \cdot x\text{H}_2\text{O}$	5.9473	MnCl_2	2.8999
$\text{Ni}(\text{H}_2\text{O})_2 \text{Ni}(\text{CN})_4 \cdot 4\text{H}_2\text{O}$	$\text{K}_2\text{Ni}(\text{CN})_4 \cdot x\text{H}_2\text{O}$	3.5084	$\text{NiSO}_4 \cdot 6\text{H}_2\text{O}$	3.5608
$\text{Zn}(\text{H}_2\text{O})_2 \text{Ni}(\text{CN})_4 \cdot 4\text{H}_2\text{O}$	$\text{K}_2\text{Ni}(\text{CN})_4 \cdot x\text{H}_2\text{O}$	3.1686	$\text{ZnSO}_4 \cdot 7\text{H}_2\text{O}$	3.78

The transition metal salt solution was added dropwise while slowly stirring using a magnetic stirrer. Both solutions were heated to 60 °C prior to combining and the tetracyanonickelate solution was maintained at 60 °C during the addition. After all of the aqueous solution of the transition metal salt was added, the reaction was allowed to cool without stirring. The precipitation formed within 15 seconds of the mixing. The precipitate settled rapidly and was washed by light centrifugation and decanting. The $\text{Ni}(\text{H}_2\text{O})_2\text{Ni}(\text{CN})_4 \cdot 4\text{H}_2\text{O}$ precipitated solid was much smaller than the others and was more difficult to wash. The washed solid powders were air dried. These powders were

examined by X-ray powder diffraction in the Bragg-Brentano geometry on a Bruker D8 Focus diffractometer with an area matrix detector using a Cu K α source from 2.0 degrees 2-Theta to 80.0 degrees 2-Theta. The powders were measured by thermal gravimetric analysis (TGA) on a TA Instruments® Q50 TGA. The sample was loaded on a 10 mm platinum pan. The analysis for each product used a ramp rate of 20 °C per minute from room temperature to 850 °C in argon shielding gas. The sample size was 15-20 mg.

3.1.3. Formation of Interfacial Sheet Method

A series of experiments were performed to attempt to synthesize the cyanide-bridged transition metal complex directly onto the membrane support material. This was accomplished by using a modified version of the U-tube bridge apparatus used to synthesize the single crystals. The device used a 25 mm polypropylene filter holder with a plastic mesh grating between a threaded clam shell housing. A rubber gasket formed a watertight seal between the halves. Polypropylene tubing was used to complete the solvent bridge. These tubes were connected using Speedfit® connectors at the inlet and outlet. The two pieces threaded together and a water tight seal was formed by a rubber gasket between. With the membrane support loaded in the holder, the apparatus was assembled under DI water in a similar fashion as described above. The test tube on each side was loaded with solid reactants and the tubes sealed using rubber stoppers. The device was held upright in a metal rack and placed in an oven at 40°C. The holder and tubing were not transparent so evaluation of the apparatus and growth of the membrane

was impossible other than by complete disassembly. The device was left undisturbed for a period of four weeks. Several attempts were made but the device was compromised on every attempt and air formed or was trapped in the holder at the membrane. This led to incomplete coverage so these membranes were never evaluated. A variety of modifications to the device failed.

3.2. Hydration States of Cyanide-Bridged Transition Metal Complexes

There were interesting differences in appearance, materials formation, and diffraction data in both the precipitation and single crystal growth methods. An experiment was designed to measure the water contained in the structure of the 3D transition metal complex. This was accomplished by using the TGA to collect dehydration data. The powder samples were placed in a 100% humidity chamber for 24 hours prior to analysis to ensure a completely hydrated state at room temperature and standard pressure. The sample size was 10 mg. A slower ramp rate of 5 °C per minute from room temperature to 250 °C was used. This data would show both the amount of water contained in the sample and also the type of interaction and probable location in the crystal structure.

3.3. Exfoliation of 2D Sheets from 3D Frameworks

Many of the samples treated and used in subsequent experiments were obtained from the previous work of Nash *et al.*³⁰ Many of these crystals had been

growing for extended periods of up to two years. The crystals ranged in size from <0.1 mm to 1 mm in length. The specimens have been stored in jars containing DI water. Some were broken up into flakey sheet-like pieces. The water remained clear even after shaking. Good specimen crystals of $M = \text{Fe}, \text{Mn}, \text{and Cd}$ were found and were exfoliated.

Several pieces of crystal were placed in a small pyrex beaker. DDP was added drop wise to a height of just covering the crystals. The beaker was heated to 175 °C in an air oven without agitation. The boiling point of DDP is 245 °C at standard pressure so no boiling was observed. There was a hazy substance above the liquid during heating, possibly water vapor. The crystals were seen to expand into flakey layers. The beaker was removed from the oven and allowed to cool in air. The $M = \text{Mn}$ crystals were less flakey than either the $M = \text{Fe}$ or the $M = \text{Co}$. The samples were transferred to a 20 ml test tube and sonicated using an ultrasonic probe, Sonics and Materials INC. Vibra-cell® model, for 1 minute. Care was taken to not let the sample overheat. In all three samples particulate could be seen in the liquid following sonication. Several of the exfoliated materials left from Nash *et al.* were also investigated. Many of these exhibited the appearance of crystallinity that differed from the hydrated single crystals.

The bulk precipitated powder samples were exfoliated in a similar method but at lower concentrations in the DDP. The samples exfoliated were $\text{Ni}_2(\text{CN})_4$, $\text{FeNi}(\text{CN})_4$, $\text{MnNi}(\text{CN})_4$ and $\text{ZnNi}(\text{CN})_4$. The process was originally carried out

using oven-dehydrated materials but this was found to produce poor results. These samples were heated in air to 100 °C with a double boiler. Frequent stirring was done using a glass rod. Sonication was performed using the Vibra-cell® ultrasonic probe for two 30 second intervals with intermittent stirring. The material was then heated in an oven to 180 °C for several hours. An additional 5 ml of DDP was added. Further ultrasonic agitation was applied for 1 minute.

3.4. Ion Selective Membrane Fabrication and Testing

3.4.1. Deposition of Exfoliated Precipitated Powder

The simplest and fastest synthesis method for producing the cyanide-bridged transition metal complex was through the bulk precipitation method described above. The resulting powder has the potential to be utilized in an ion selective membrane. The powder was exfoliated in DDP at low concentrations. The resulting suspension contained individual sheets of the material. There is a broad distribution to the size of these sheets depending on the synthesis conditions and to a lesser extent, the sonication intensity and duration. These aspects have not been fully explored. The material in this research was analyzed by scanning electron microscopy (SEM) on a FEI Helios NanoLab 400. The sheets were deposited onto a polymeric substrate that provides rigid strength for the membrane. Two types of polymeric support were investigated. Figure 16 shows SEM magnified images of the structure of polytetrafluoroethylene (PTFE) and polyvinylidene fluoride (PVDF) membranes. The

pore size of these membrane discs is 200 nanometers with a thickness of 150 micrometers. These membranes will not retain small components in water such as sodium and chloride ions. The pressure requirement to move water through these membranes is about 10 psi.

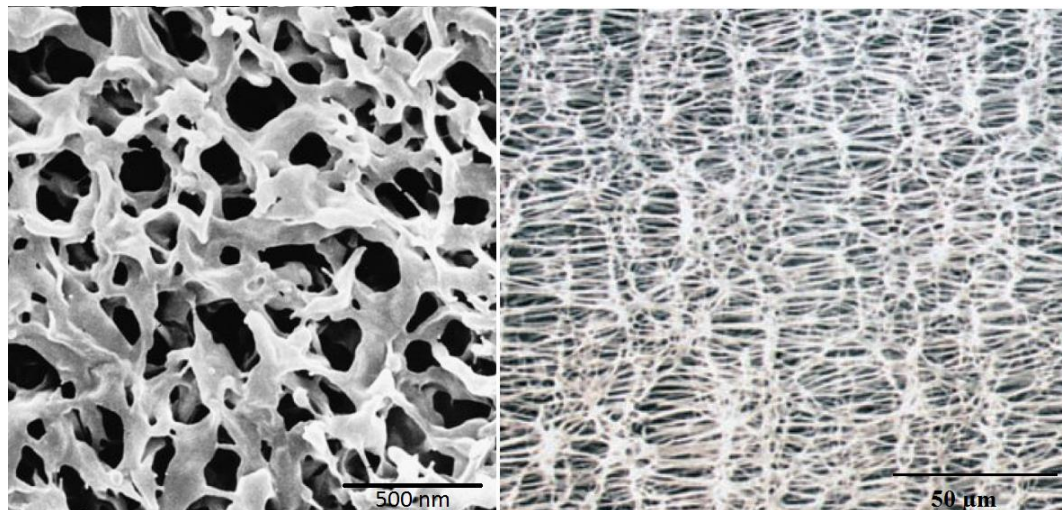


Figure 16. SEM images of the hydrophobic (right) and hydrophilic (left) membrane supports. Hydrophobic polytetrafluoroethylene and hydrophilic polyvinylidene fluoride were used as membrane supports for the atomistically thick membrane sheets.^{119,120}

Preparation of ion selective membranes using the nanosheets deposited onto the porous support is similar to the construction of a polymeric thin film composite membrane, except in process. The sheets, being pre-synthesized and exfoliated, were deposited onto the support by mechanical and gravitational methods. The goal was to have larger sheets covering the porous openings preventing ions from passing. The aim was that the coverage be continuous enough that no open pores in the support

would be exposed to the saline water. It was expected that sheets of the membrane that were too small would wash through the support during the process.

In one set of trials, the platelet-like membrane sheets were allowed to settle unto the membrane supports through a drop cast method. Drop casting was performed by dripping liquid suspensions onto a substrate while it was rotating. The drop cast apparatus was built using a laboratory magnetic stirrer motor with a thin aluminum plate functioning as a turntable. The polymer support was held in place by double sided tape. A suspension of exfoliated particles in DDP were drop cast on the polymer support discs in air at standard temperature and pressure (STP). The DDP was carefully poured away after several hours. The process was repeated three times. After the final cycle the membrane and the support disc were placed on a vacuum filter and water was used to flush the remaining DDP from the membrane and support. The single exfoliated sheets are not visible on the support but there was slight discoloration or darkening. The membranes were permitted to dry in some experiments and remained wetted in others. It was believed that drying resulted in cracking of the membrane but this was not effectively studied.

In another set of experiments the sheets were deposited by vacuum deposition where they were pulled onto the supports using vacuum. The vacuum flask used was a Millipore® 47 mm glass disc holder designed to handle high vacuum. The filter holder contained a fine glass frit to support the polymer discs. Vacuum was produced to -25 mm of Hg using a Welch® Duoseal® 1402 laboratory vacuum. Exfoliated powder

suspended in DDP was charged onto the polymer disc support loaded in the filter holder. DDP was pulled through and followed by DI water to rinse DDP off of the membrane. The porous structure of the membrane support was coated by many layers of the exfoliated sheet. If the layer was continuous, the membrane should provide ion-selectivity and be capable of desalination. Many experiments were performed with various layer depths of the precipitated material. It was believed that the best approach was to continue to add material until the filter was blinded and no more DDP could pass through. After washing, this may produce a semipermeable barrier. The layers were thick, some of them more than 1mm in thickness. When dry, the membrane powder formed a mud crack effect. The cracking was smoothed mechanically using a metal spatula. The results are discussed in Chapter 4.

3.4.2. Deposition of Exfoliated Single Crystal

The single crystals were difficult to produce and very little membrane experimentation was performed. The drop cast method described above was used in a similar manner. The exfoliated single crystal material in DDP was very dilute. The PTFE membrane support was difficult to wet with DDP. Pools formed on the surface and rolled to the edges easily. Achieving complete coverage of the support membrane was difficult. Membranes were washed in a vacuum funnel with DI water to remove DDP prior to testing.

3.4.3. Interfacial Precipitation Method

In an attempt to increase the size of the crystals using the precipitation method. A series of experiments were conducted where a deviation from the normal precipitation method was explored. The interface between the two aqueous reactants could be controlled to slow down the rate of growth by forcing diffusion to occur. Two types of interfacial layers were tried. The interfacial precipitation was carried out on a large Pyrex watch glass at room temperature. First, 20 ml of a 0.025 g/mL aqueous solution of potassium tetracyanonickelate was poured into the watchglass. Next, a layer of 10 mL isobutyl alcohol was introduced above the potassium tetracyanonickelate(II) solution by slowly pouring around the edges. Lastly, 20 mL of a 0.03 g/mL aqueous solution of iron(II) ammonium sulphate was poured around the edges and floated over the alcohol layer. Little reduction in speed was realized and it appeared that the alcohol migrated away from the precipitation formed. The alcohol was allowed to evaporate and the precipitation in water was rinsed by centrifugation methods mentioned above.

The experiment was repeated with an interfacial layer of ethyl acetate. This created a skin like structure at the lower interface, but after pushing the skin with a metal spatula the skin fractured easily and broke into fine particles. The precipitation was still too rapid and no large crystalline growth was seen.

3.4.4. Membrane Function Testing

All membranes fabricated were tested by placing the 47 mm disc into a sealed holder made of polypropylene. The two piece holder consists of an inlet on the lid, a plastic mesh grating and an outlet at the bottom piece, opposite the inlet. The two pieces threaded together and a water tight seal was formed by a rubber gasket between. Polypropylene tubing was attached using the Speedfit® system. Valves on the inlet and outlet side controlled flow through the test holder. A water vessel was made using a 1.0 liter plastic bottle. The water was pressurized using compressed air from the laboratory air supply. This air had a maximum pressure of 90 pounds per square inch. The water vessel was filled with saline water of various concentrations that had been prepared by serial dilution in the lab using laboratory grade sodium chloride crystals and DI water. No trace elements normally found in seawater were added. The saline water concentrations prepared for the experiment are shown in Table 5. The total dissolved solids (TDS) of the saline water samples was measured using an HM brand digital pocket TDS meter. The range of the meter was from 0 ppm to 9990 ppm with a resolution of 1 ppm for the lower range and 10 ppm for the higher range. The measurements were calibrated for temperature variation.

Table 4. Saline water test solutions. Solutions were prepared by serial dilution to test desalination effectiveness.

Serial dilutions performed from 50,000 ppm.						
Measurements taken at 22 °C						
Dilution #	Conc. (mg/L)	TDS :1	TDS :2	TDS :3	TDS :4	
1	0.00	0	0	0	0	0
2	0.50	2	3	2	3	3
3	5.00	7	7	7	7	7
4	50.00	49	52	53	52	52
5	500.00	503	508	512	508	508
6	5000.00	3940	3830	3840	3940	3940
7*	50000.00	42610	42450	41100	42300	42300

* Diluted by 10X to stay within range of the meter

Testing was carried out by securing the membrane to be tested in the holder and filling the water vessel with the test saline water. The air supply was connected using a quick connect coupler. Air was supplied via a regulator on the supply outlet and was used to meter and control pressure. The outlet of the test holder was open to standard air pressure and a tube allowed for water to drain into an open flask for collection. The TDS of the collected water was measured and recorded using the hand held meter in real-time.

3.5. Magnetic Property Experiments

3.5.1. Observation of Magnetic Susceptibility

The magnetic experiments conducted early on were observational. The dry crystals and precipitated powders were not visibly influenced by manipulation of a

magnetic field generated by a large bar magnet or a large horseshoe magnet. When placed into water however, both single crystals and powders show some attraction to the magnetic field. This was confirmed experimentally by preparing 2.0% by weight, suspensions of the hydrated powder into DI water in a small vial. This was shaken to suspend the powder in the water. This suspension settled quickly due to the large particles. The vials were laid into a gap between two poles of a large horseshoe permanent magnet. The duration of the experiment was about thirty minutes. As the particles settled they would either be drawn to the poles or settle to the bottom. Figure 17 shows the experimental setup of the vial containing suspended powder. The horseshoe magnet used is a permanent magnet producing a magnetic field strength of 0.5 Tesla. The samples were also shaken and left to sit undisturbed on the bench out of the magnetic field as comparison. The precipitated powders tested in this experiment were $\text{Fe}(\text{H}_2\text{O})_2\text{Ni}(\text{CN})_4 \cdot 4\text{H}_2\text{O}$, $\text{Mn}(\text{H}_2\text{O})_2\text{Ni}(\text{CN})_4 \cdot 4\text{H}_2\text{O}$, $\text{Ni}(\text{H}_2\text{O})_2\text{Ni}(\text{CN})_4 \cdot 4\text{H}_2\text{O}$, $\text{Co}(\text{H}_2\text{O})_2\text{Ni}(\text{CN})_4 \cdot 4\text{H}_2\text{O}$, and $\text{Zn}(\text{H}_2\text{O})_2\text{Ni}(\text{CN})_4 \cdot 4\text{H}_2\text{O}$.

Solid crystalline pieces from the single crystal growth were also placed into water and measured in a similar manner. Large crystals and agglomerates were fractured and crushed in the water using a metal spatula. The smaller crystal pieces have a better chance at being attracted to the magnet since it appears the magnetic effects are small. The single crystals tested were $\text{Fe}(\text{H}_2\text{O})_2\text{Ni}(\text{CN})_4 \cdot 4\text{H}_2\text{O}$, $\text{Mn}(\text{H}_2\text{O})_2\text{Ni}(\text{CN})_4 \cdot 4\text{H}_2\text{O}$ because no single crystal material for the others was collected.



Figure 17. Observational magnetic experiment setup. A small vial containing cyano bridged transition metal complex suspended in water is placed in a magnetic field produced by a permanent horseshoe magnet.

3.5.2. Ferromagnetic Analysis

The magnetic influence on some of the transition metal cyanides is not surprising since DFT calculations predicted some magnetic property. The predictions done by Nash *et al.* stated that the $M = \text{Fe}, \text{Mn}, \text{Co}$ in the formula $M(\text{H}_2\text{O})_2\text{Ni}(\text{CN})_4 \cdot 4\text{H}_2\text{O}$ would have higher magnetic moments in the bulk crystal than $M = \text{Ni}$ or Zn .³⁰ They also suggested that Mn and Co would have antiferromagnetic

properties while Fe would have ferromagnetic properties. To test this visually a simple bench experiment was designed. The 2.0 wt% suspensions of precipitated powders were all placed in the magnetic field of the large horseshoe magnet for 48 hours. A steel rod of diameter 6.35 mm was heated and force impacted repeatedly to remove any possible magnetism from the iron in the steel. The samples were shaken vigorously to suspend all particles. The rod was inserted through a septum lid and into the suspension to a height that would be very close to, but above, the level of the particles in the vial after they settle. The rod was inspected for adhering powder and influence on the settling characteristics. The duration of the experiments was thirty minutes.

3.5.3. Thermal Gravimetric Analysis Magnetic Experiment

All of these material's magnetic properties appear to be small. A more sensitive method for semi-quantitatively analyzing these properties was devised to use a TGA modified to operate in a magnetic field. Magnetic properties are used in the calibration of the instrument by verification of a calibration alloy standard's Curie temperature. The bar magnet designed for use on the TGA was used in the same manner for our experiment. It may be possible to determine the material's Curie temperature. Using the TA Instruments Q50 TGA it would be possible to find a Curie point by ramping the temperature and recording the weight loss while in a magnetic field. This approach will only work between room temperature and the material's degradation temperature where the carbon-metal or nitrogen-metal bonds break. The

magnetic field is created by placement of a large bar magnet just below the TGA furnace when it is closed. Figure 18 shows the location of the magnet relative to the sample furnace. Taring of the platinum pan was performed with the magnet in place. A 10 mg sample was loaded into the tared pan. The sample was heated from room temperature to 400 °C at 10 °C / min. in argon while in the magnetic field the entire time.

Another set of experiments performed on the hydrated powders using a magnetic field in the TGA was to perform isothermal magnetic response tests. This was done by ramping 10 mg of the hydrate powder to a specific temperature and isothermally testing the effect of placing and removing the magnet for a specified amount of time. Two temperatures were tested on each sample, 30 °C and 250 °C. The magnet was inserted beneath the sample furnace after ten minutes at each isotherm and removed ten minutes later.



Figure 18. Magnetic TGA Experiment. Photo is of front and side views of the TGA in the left and right panes respectively. The 1x1x6 inch bar magnet is positioned on wood blocks. Experiments were conducted to see the effect of heat on the sample's magnetic properties.

3.5.4. Vibrational Sample Magnetometer Experiments

The initial magnetic experiments conducted on these materials were qualitative. To get quantitative data and proof of the type of magnetism (diamagnetic, paramagnetic, ferromagnetic, antiferromagnetic) and hysteresis curves, a more sophisticated method was needed. Vibrational Sample Magnetometry was used. The instrument used to collect hysteresis loops was located at Texas State in the Department of Physics. This VSM was limited to room temperature analysis. It is capable of generating a field intensity of 5000 oersted (Oe). Precipitated crystals of $\text{Fe}(\text{H}_2\text{O})_2\text{Ni}(\text{CN})_4 \cdot 4\text{H}_2\text{O}$ and $\text{Ni}(\text{H}_2\text{O})_2\text{Ni}(\text{CN})_4 \cdot 4\text{H}_2\text{O}$ were analyzed. The dry powders were carefully loaded into

small plastic cylinder sample holders. Light packing was done on the powder. The mass of the $\text{Fe}(\text{H}_2\text{O})_2\text{Ni}(\text{CN})_4 \cdot 4\text{H}_2\text{O}$ powder was 0.0018 grams by subtracting the mass of the sample holder. The $\text{Ni}(\text{H}_2\text{O})_2\text{Ni}(\text{CN})_4 \cdot 4\text{H}_2\text{O}$ powder sample was 0.0022 grams. Data was collected at the highest sensitivity, 0.3 seconds of integration time, and in normal measurement mode. A nickel calibration sample was used to adjust phase of “lock-in.” The system was aligned, and the lock-in phase was re-verified prior to collecting data.

CHAPTER 4

RESULTS AND DISCUSSION

4.1. Molecular Dynamics Simulations

Computational simulations accomplished in this work were designed to predict the behavior of the cyanide-bridged transition metal 2D sheets as a means to filter water and show the improved efficiency of desalination over the current technology. The experiments conducted generally fell into three categories within this effort. First, the model constructs were tested for accuracy in form and structure during dynamic simulations. The results were compared to crystallographic data to set assumptions regarding where the modeling might provide less-than-real conclusions. Next, the membranes were evaluated for performance in water permeability and ion selectivity. Some indication as to how these membrane materials might compare to other atomistically thick materials in performance was the goal. Finally, the membrane material was studied closely during the passage or transit of individual water molecules and ionic species to determine the energetic costs of the interactions with atoms in such close proximity. These data show the likelihood of particular atomic events based on an energetics comparison.

4.1.1. Model Construction and Crystallographic Comparisons

All models in this study were constructed from study of the available crystallographic data and other molecular and atomic data for constituents such as water, ionic species and DDP. This data has been previously published and the crystallographic information used is available in the Appendix. The models of the 3D cyanide-bridged transition metal frameworks were all built as periodic models using multiples of the unit cell to create sheets. Waters of hydration were added to the coordination sites on the octahedral structured atoms and free water in the interlamellar spaces. Once this was accomplished, the models were subjected to energy minimization and dynamic simulation with cell dimensional constraints removed. This allowed the unit cell to expand or contract to a size according to predictions of the bond lengths and slight variation to bond angles. After this was performed the bond lengths were again compared to crystallographic data and deviations noted.

Table 5 shows a comparison of the bonds lengths approximated by the computational model to what was determined by the crystallographic data from single crystal X-ray diffraction (XRD). These structures are hydrated upon synthesis, but changes in the hydration state will alter the crystallographic form. There has been limited study on the effect of dehydration on the structure of these materials.^{25,30} It is expected that the stability of the hydrated forms in the material plays a role in both crystal formation and the ability to form intercalates in the 3D structure.

Table 5. Modeled bond lengths vs. crystallographic bond lengths. The crystal structure data for selected species of cyanide-bridged transition metal complexes is compared to the values obtained by molecular dynamics simulations.

Name	Crystal Data	Model	Crystal Data	Model	Crystal Data	Model	Crystal Data	Model
	M1- N Bond (Å)	M1- N Bond (Å)	C- N Bond (Å)	C- N Bond (Å)	C- M2 Bond (Å)	C- M2 Bond (Å)	M1- O (Å)	M1- O (Å)
Fe(H ₂ O) ₂ Ni(CN) ₄ ·4H ₂ O (1)	2.143	1.995	1.150	1.147	2.861	2.859	2.156	2.156
Mn(H ₂ O) ₂ Ni(CN) ₄ ·4H ₂ O (2)	2.200	1.999	1.350	1.167	2.284	1.933	2.239	1.909
Co(H ₂ O) ₂ Ni(CN) ₄ ·4H ₂ O (3)	2.095	1.929	1.140	1.180	1.851	1.994	2.128	1.831
Ni ₂ (H ₂ O) ₂ (CN) ₄ ·4H ₂ O (4)	2.052	1.884	1.470	1.190	1.886	2.031	2.400	1.780
Fe(H ₂ O) ₂ Ni(CN) ₄ ·H ₂ O (1)	2.128	1.958	1.150	1.159	1.861	1.868	2.196	1.872
Mn(H ₂ O) ₂ Ni(CN) ₄ ·H ₂ O	ND	2.006	ND	1.168	ND	1.914	ND	1.891
Co(H ₂ O) ₂ Ni(CN) ₄ ·H ₂ O	ND	1.993	ND	1.181	ND	1.970	ND	1.810
Ni ₂ (H ₂ O) ₂ (CN) ₄ ·H ₂ O	ND	1.894	ND	1.190	ND	2.008	ND	1.759
FeNi(CN) ₄	ND	1.915	ND	1.150	ND	1.841	ND	
MnNi(CN) ₄	ND	1.940	ND	1.150	ND	1.842	ND	
CoNi(CN) ₄	ND	1.848	ND	1.153	ND	1.849	ND	
Ni ₂ (CN) ₄	ND	1.806	ND	1.160	ND	1.806	ND	
Reference	(1) Nash	(2) Ray	(3) Yan	(4) Hibble			ND = No Data	

The crystallographic bond lengths for the dehydrated forms were not found except for the trihydrate form of the iron containing complex. The formation of single crystals of these dehydrated and partially dehydrated complexes is a challenge because the structure is likely less stable.

The unit cell was determined by single crystal X-ray analysis. Table 6 compares the crystallographic unit cell dimensions for the materials after model energy minimizations. Following this step, the models were used with unit cells constrained. This is required if atoms in the structure are constrained from movement because a variation in the unit cell without a corresponding movement of atoms creates a disagreement error. A similar approach was used in the modeling of graphene and nanoporous graphene sheets used in these evaluations. It is worthwhile to note that simulations of organic compounds using the UFF are atypical. Most other force fields are not accurate in models containing transition metals.

Table 6. Comparison of the unit cell dimensions of molecular models with crystallographic data.

	Unit Cell Parameters, Literature			
	a =	b =	c =	Volume (\AA^3)
$\text{Fe}(\text{H}_2\text{O})_2 \text{Ni}(\text{CN})_4 \cdot 4\text{H}_2\text{O}$	12.0962	14.0037	7.225	1223.85399
$\text{Mn}(\text{H}_2\text{O})_2 \text{Ni}(\text{CN})_4 \cdot 4\text{H}_2\text{O}$	12.311	14.134	7.313	1272.48887
$\text{Co}(\text{H}_2\text{O})_2 \text{Ni}(\text{CN})_4 \cdot 4\text{H}_2\text{O}$	12.178	13.885	7.143	1207.8208
$\text{Ni}(\text{H}_2\text{O})_2 \text{Ni}(\text{CN})_4 \cdot 4\text{H}_2\text{O}$	7.09	13.84	6.10	598.56616

All values in angstroms

	Unit Cell Parameters, Model			
	a =	b =	c =	Volume (\AA^3)
$\text{Fe}(\text{H}_2\text{O})_2 \text{Ni}(\text{CN})_4 \cdot 4\text{H}_2\text{O}$	12.05	14.224	7.909	1355.59627
$\text{Mn}(\text{H}_2\text{O})_2 \text{Ni}(\text{CN})_4 \cdot 4\text{H}_2\text{O}$	12.4	14.288	7.992	1415.95223
$\text{Co}(\text{H}_2\text{O})_2 \text{Ni}(\text{CN})_4 \cdot 4\text{H}_2\text{O}$	12.332	14.05	7.665	1328.07316
$\text{Ni}(\text{H}_2\text{O})_2 \text{Ni}(\text{CN})_4 \cdot 4\text{H}_2\text{O}$	7.45	14.77	7.25	797.764625

All values in angstroms

4.1.2. Water Permeability Models

The modeling of water permeability involved the use of bulk amounts of water molecules forced between and impermeable piston and the test membrane. This method was used first to provide evidence that the pristine graphene sheet would not allow water molecules to deform and transit through abnormally stretched bonding or unnatural bond angle behavior. The result of this experiment was affirmative and the pristine graphene was used throughout as the piston.

Water permeability of the cyanide-bridged transition metal sheets was predicted to be high since there is a high density of pore-like openings in the framework. Water

molecules in the model readily transited all the membranes at pressures that would be equivalent to the corresponding volume of water. Direct system pressure was not provided by the software and this author was unable to relate atomic pressure to system pressure in these models. This meant that the pressure at which water would permeate the membrane was not predictable. Determination of the membrane pressure's contribution to the RO desalination equation for calculation of water flux could not be accomplished. Only comparative predictions were possible for water permeation determination. By monitoring the sum of potential and kinetic energies of the system during dynamic simulation, and the ease at which water molecules were able to orient and move through the membrane, assumptions were made regarding the performance. When water molecules became trapped between the piston and the test membrane, the energies of atomic repulsion increased irrationally fast. This was a qualitative indication of water permeability and was used as a first-pass approach to comparing the performance.

The models of nanoporous graphene with hydrophobic and hydrophilic edge groups and two pore sizes, 14 \AA^2 and 25.5 \AA^2 , were evaluated by identical means. The result showed that the nanoporous graphene sheets lack a high enough pore density to compete with the net-like structure of the cyanide-bridged transition metal sheets. An estimation was made that water permeation in the transition metal sheets was at least 1.65 times the permeation rate in nanoporous graphene with pore structure of 50% of the available surface area. Having engineered pore openings very close to one another in graphene could significantly lower its structural integrity.

4.1.3. Ion Selectivity Models

As was the case for the permeability models, the ion selectivity modeling was mostly qualitative. It was possible to form ratios of permeated water to ions that transit the membrane. Figure 19 shows the comparison for salt rejection performance for the FeNi(CN)₄ membrane and nanoporous graphene. The top graph compares the graphene sheet, having a 25.5 Å² pore, to the FeNi(CN)₄ membrane performance at a starting salt concentration of 35 ppt. Both hydroxyl and hydrogen edge modifications of the graphene pore are evaluated. The total ions passing the membrane versus the number of water molecules was plotted. A lower slope indicated better salt rejection. The graphene sheet only contained a single pore so its pore area is 15 times smaller than the available area for species to transit the membrane in these models. Having more pores on the graphene sheet in the model would increase the water permeability rate but also likely would result in lower salt rejection rates. The lower graph shows that at higher starting concentrations the salt rejection was lower as higher numbers of Na⁺ ions breached the pores relative to water molecules. The identity of the ion is not shown, but for the transition metal sheets no chloride ions passed at any time. The results suggest that the chloride ion is strongly attracted to the transition metal atoms and does not move through the pore.

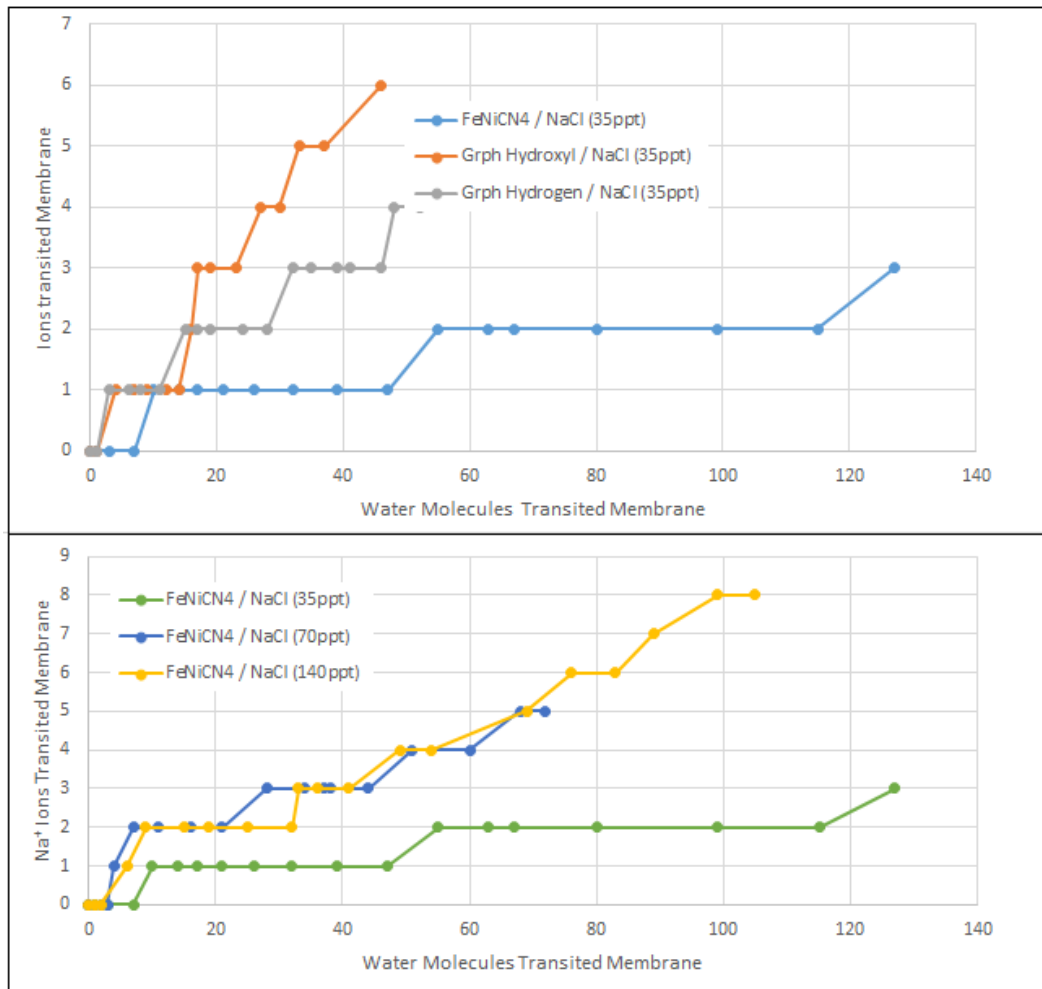


Figure 19. Plots of ion to water transit rates for $\text{FeNi}(\text{CN})_4$ and nanoporous graphene. $\text{FeNi}(\text{CN})_4$ is compared to nanoporous graphene with hydroxyl and hydrogen edge modification in the top graph. $\text{FeNi}(\text{CN})_4$ performance at different ionic concentrations is shown below. In both graphs a lower slope means better salt rejection.

Attraction of the chloride to the surface of the membrane is favorable to restricting its passage, however it would suggest a possibility of an ionic buildup on the surface leading to substantial concentration polarization on the surface.¹²¹ This effect would essentially act as a fouling mechanism but it couldn't be tested on the limited number of molecules occupying this system.

It was seen that higher concentrations of ionic species led to a lower rejection rate. This was especially prevalent at the early stages of the simulation where sodium ions were close to the surface and water pushed them through. What was absent from the simulation was the ionic cage effect around the ions. Water forms cage-like structures called solvation shell formation.¹²²

An observation was made from the behavior of water molecules passing the membrane that orientation of the molecule is an important aspect of the transit. The molecule tended to bounce off the membrane rather than transit if it wasn't oriented with a hydrogen facing the membrane. Naturally this effect is not encountered on ionic species but could play a role due to solvent shell effects not studied in these models.

4.1.4. Pore Transit Energy of Single Molecule/Ion Models

The detailed modeling of water molecules and ions as they pass individually through a pore in the membrane allowed for the collection of more precise energies of the interactions between the passing molecule or ion and the atoms around the pore. Figure 20 shows the close contacts model of a water molecule transiting the membrane using a wire frame model. In the frameworks $\text{CoNi}(\text{CN})_4$ and $\text{Ni}_2(\text{CN})_4$, the lower area in the pore required a slight contortion of the framework as water moved through. This

action required a higher energy and would likely result in a lower water permeability in these materials than frameworks containing Fe, Mn, or Pt.

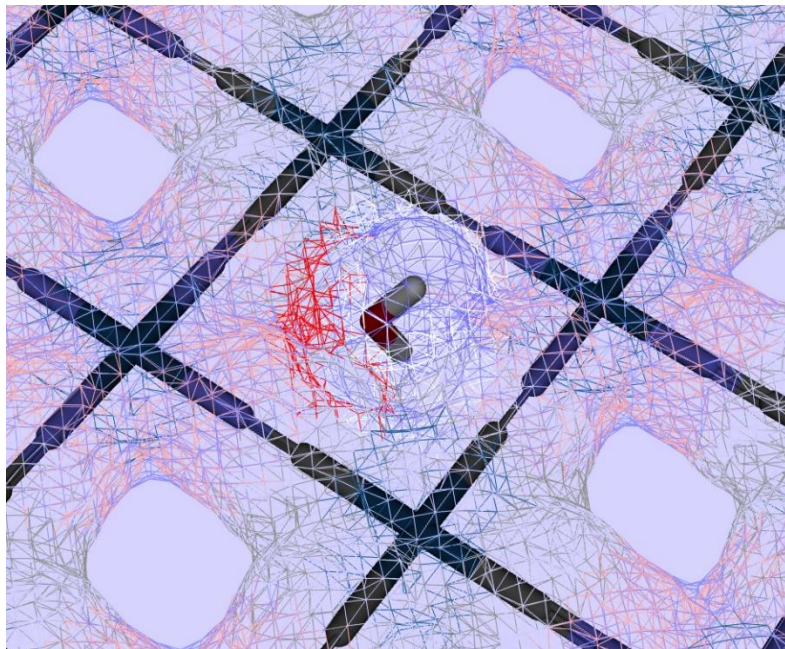


Figure 20. Wire frame model of the close contacts of water and the sheet atoms while in the pore of a $\text{Pt}_2\text{Ni}(\text{CN})_4$ sheet.

The effect of the identity of the transition metal and its atomic radii on the available area for the species to move through was studied. The water molecule aligned with one hydrogen pointing down, directly at the center of the pore. As the molecule transits the pore it tilted over so that the opposite hydrogen was pointing straight up and perfectly aligned with the center of the pore. As the molecule moved away from the membrane, there appeared to be no specific orientation following the event. The water molecule was tested in all possible orientations and will orient itself identically every time. Figure 21 shows a sequence of photos to visualize this orientation as the water

molecule moves from one side of the membrane to the other. Hydrogens are white and the oxygen atom is red in the figure.

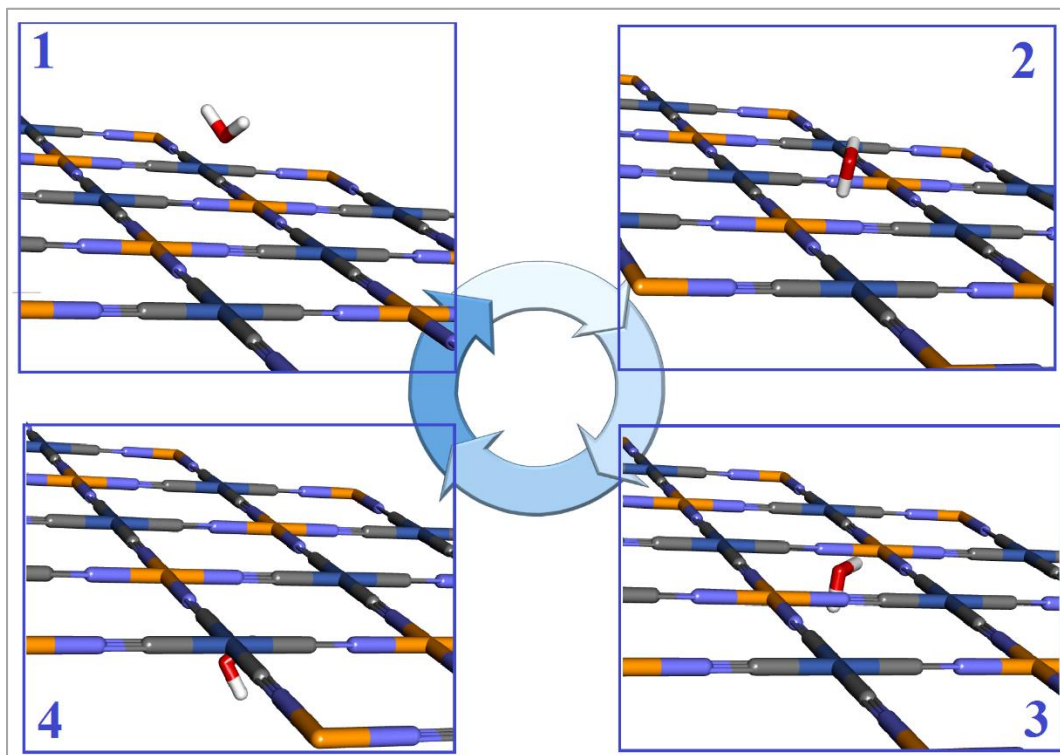


Figure 21. Sequence showing the orientation of water as it passes through the $\text{FeNi}(\text{CN})_4$ membrane. From top right clockwise the water molecule orients with hydrogen leading into the pore structure.

Additionally, experiments where the water molecule was positioned above a transition metal center, or above the nitrogen or carbon of the cyano-bridge and moved toward the membrane resulted in the water molecule always repositioning at the center of the pore and orienting the same way to transit. The ionic species behaved differently. They preferred the lowest energy state which was directly above or below the transition metal atoms, not above the opening in the center. Figure 22 compares four selected sheet

materials with different atomic radii from small to large. There was a subtle effect on the energy profile as the water molecule moved through the plane of the sheet. Interactions between the framework and the water molecule required energy input to overcome repulsion, but this energy is low in comparison to the energy required when the ion species were positioned within the pore framework.

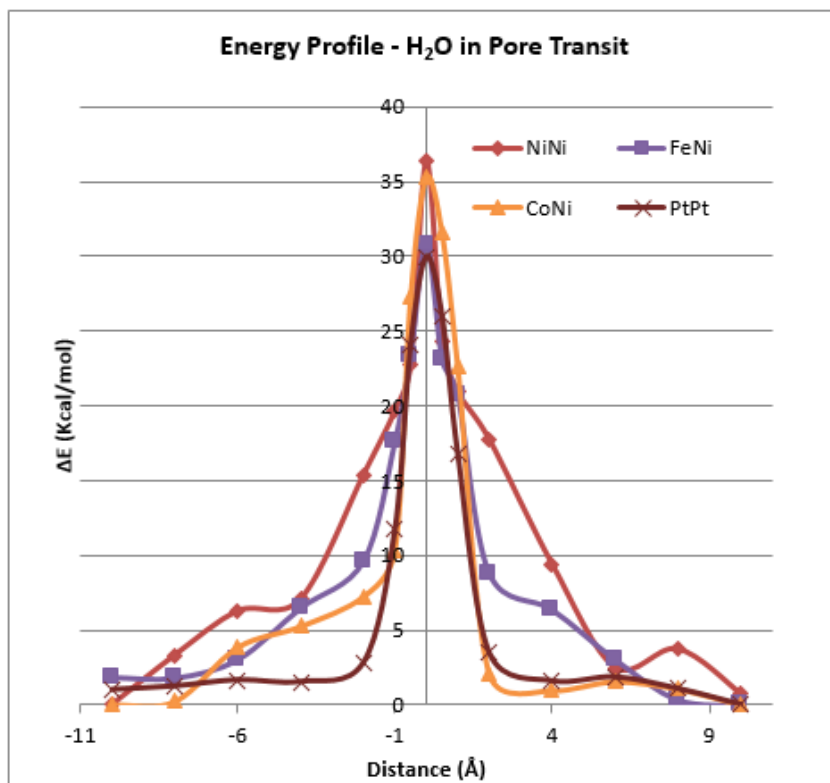


Figure 22. Energy profile of water during pore transit. The change in energy was recorded as the molecule approached and moved through the pore. The x-axis is the distance from the plane of the material. Smaller atomic radii in the transition metal exhibited a higher energy during passage.

When the experiments were conducted using sodium and chloride ions in the same manner the energy values were higher. Figure 23 reveals the higher energy profile

for ionic species to move through the pore structure than for water. The energy requirements for ions moving through are double what is required for water. To give some context to these energy values, covalent bond energies are ~75 kcal/mol for an O-O bond and ~100 kcal/mol for C-H. The van der Waal bond energy range is 5 kcal/mol to 35 kcal/mol.¹²³ The reason for the higher energy values required for chlorine and sodium are likely based on ionic radii. The radii for these ions is large compared to oxygen in water. There is a slight contortion of the pore by bond bending and stretching to accommodate size and these action increase the energy requirement. This indicates a strong case for size exclusion principles being the governing factor. The Appendix contains similar energy profiles for comparison. Quantifying the water permeability or salt rejection in this way is a good first pass approximation.

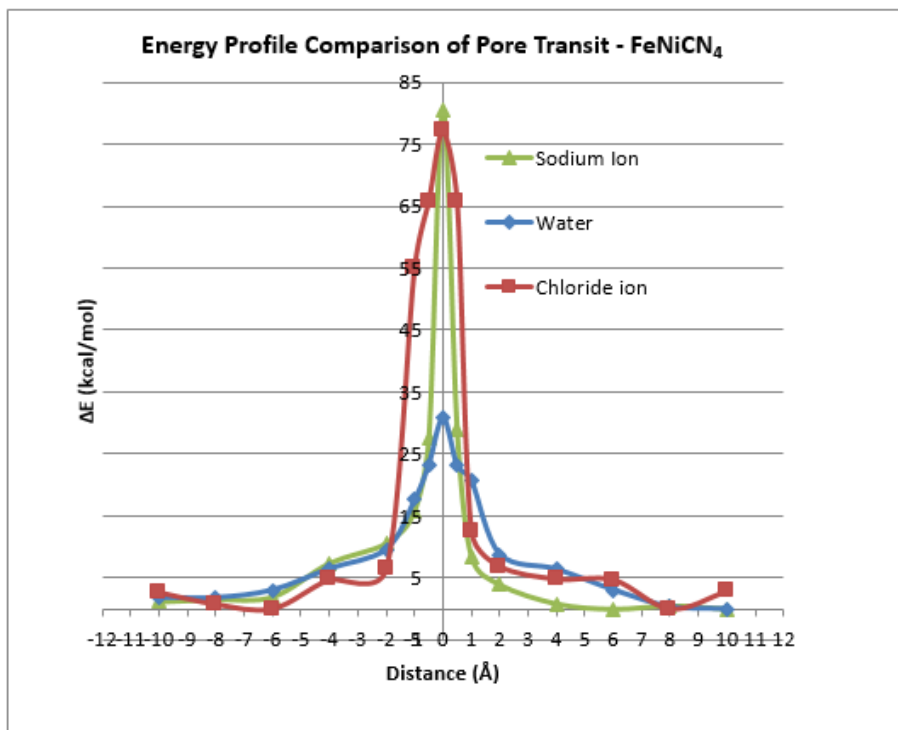


Figure 23. Energy profile comparison of water, sodium ion, and chloride as they transit the pore. The energy of passage for the sodium and chloride ions was higher than for water passage.

The modeling experiment did not examine the possible additional energy required for an ion surrounded by a hydration cage to pass through a pore. It was assumed that additional energy would be required to dehydrate the ion prior to passage, thus increasing the membrane's salt rejection.

When compared to the nanoporous graphene containing a pore area of similar size, the energy of transit was similar. The energy required was lower in the hydrophilic modified pore (hydroxyl lined). Figure 24 shows the comparison of transit energy

profiles for the sodium ion, chloride ion, and water molecule through the pore. The pore area was calculated to be 25.5 \AA^2 .

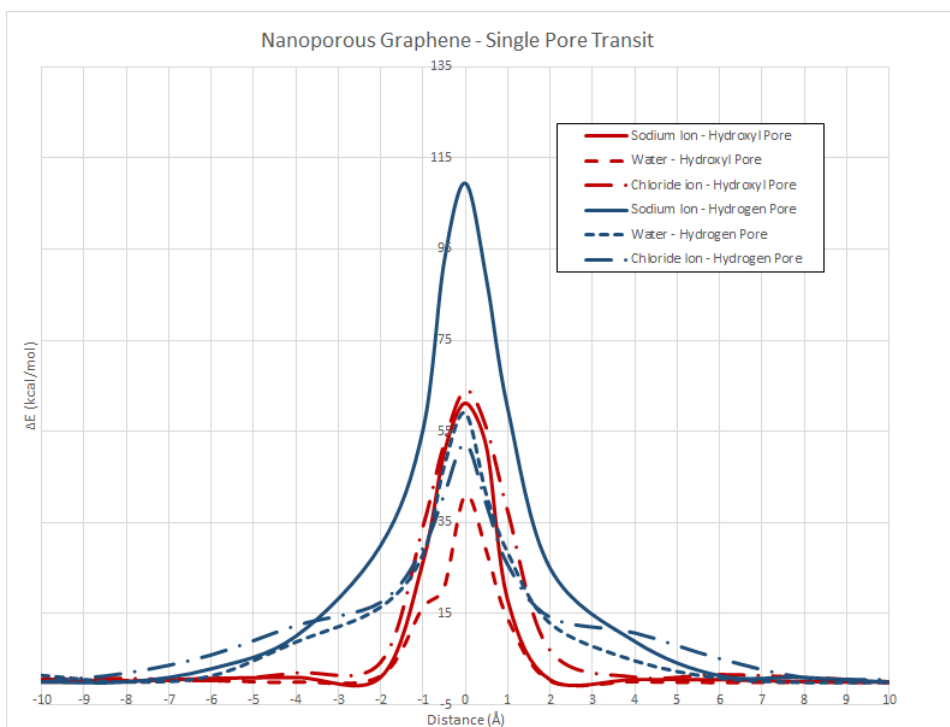


Figure 24. Energy profile comparison of hydrophobic and hydrophilic pores in nanoporous graphene. Red lines were used for the graphene pore with hydrophilic characteristic while blue lines were used for the hydrophobic pore characteristic.

4.2. Synthesis of Cyanide-Bridged Transition Metal Complexes

The synthesis of single crystal transition metal complexes yielded no successful crystals. Preparing duplicate samples in additional U-tubes may have provided successful crystal growth. An increase in the concentrations may also have resulted in crystal growth. The construction and filling of the apparatus is sensitive to faults such as air leaks. The samples may have been disturbed or up-ended during the growth period. Single crystals grown by Nash were collected and used for some of this work

The more rapid precipitation method was used to produce smaller crystals for the exfoliation and fabrication of membrane material. The precipitated powders produced good yields and were analyzed using thermal gravimetric analysis (TGA) to determine relative mass of the structure. Figure 25 is the TGA plot of synthesized precipitated powder of $\text{Fe}(\text{H}_2\text{O})_2\text{Ni}(\text{CN})_4 \cdot 4\text{H}_2\text{O}$ after it was dehydrated in an oven. The water of hydration is almost completely absent and the loss of mass above 400 °C is the thermal decomposition of carbon and nitrogen in the structure. This was determined by calculating the mass loss in the region of the plot between room temperature and 400 °C. If there is little or no weight loss the sample was already dehydrated prior to the TGA run.

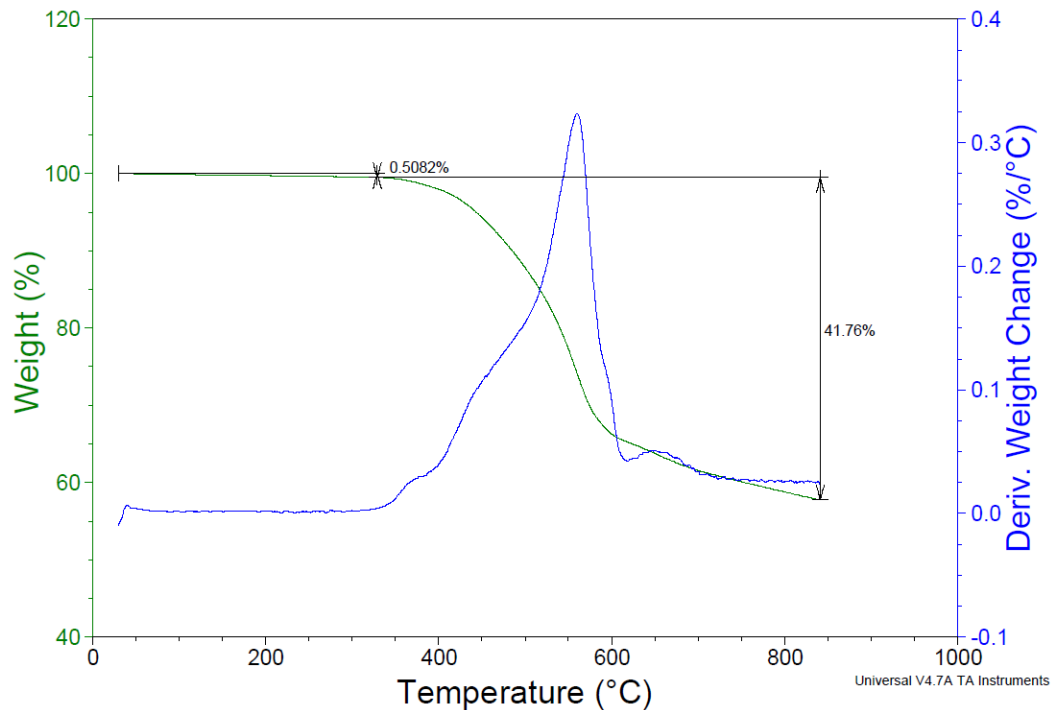


Figure 25. TGA plot of FeNi(CN)₄. Note the absence of water lost in the sample. The first losses occur over 375 °C and are the decomposition of C-N.

After all the carbon and nitrogen are gone the remaining mass is due to transition metals. Some oxides may be present but argon shielding gas prevents most of the oxidization especially when the sample was previously dehydrated. Table 7 contains the quantitative mass loss percentages used to determine the composition of precipitated powders.

Table 7. Quantitative TGA results for composition of cyanide-bridged transition metal precipitated powders

	Theoretical Mass % H ₂ O	Mass % H ₂ O Lost	Theoretical Mass % C-N	Mass % of C- N Lost	Theoretical transition metal content %	Mass % of transition metals Lost	Agreement
Fe(H ₂ O) ₂ Ni(CN) ₄ · 4H ₂ O	33.07%	0.50%	31.57%	30.43%	35.68%	28.57%	-7.11%
Mn(H ₂ O) ₂ Ni(CN) ₄ · 4H ₂ O	33.16%	0.50%	31.95%	29.87%	34.89%	29.64%	-5.25%
Co(H ₂ O) ₂ Ni(CN) ₄ · 4H ₂ O	32.76%	30.36%	31.86%	30.63%	35.07%	34.23%	-0.84%
Ni(H ₂ O) ₂ Ni(CN) ₄ · 4H ₂ O	32.78%	21.55%	31.59%	29.32%	35.63%	33.90%	-1.73%

The samples were analyzed by wide angle X-ray diffraction in the Bragg-Brentano geometry. CuK α radiation was used. The diffraction peaks were compared to structural expectations from previous work. Peak hkl indices were determined and used to confirm the structure of the cyanide-bridged transition metal complexes. Figure 26 is a compilation of the XRD patterns with the approximate hkl indices noted.

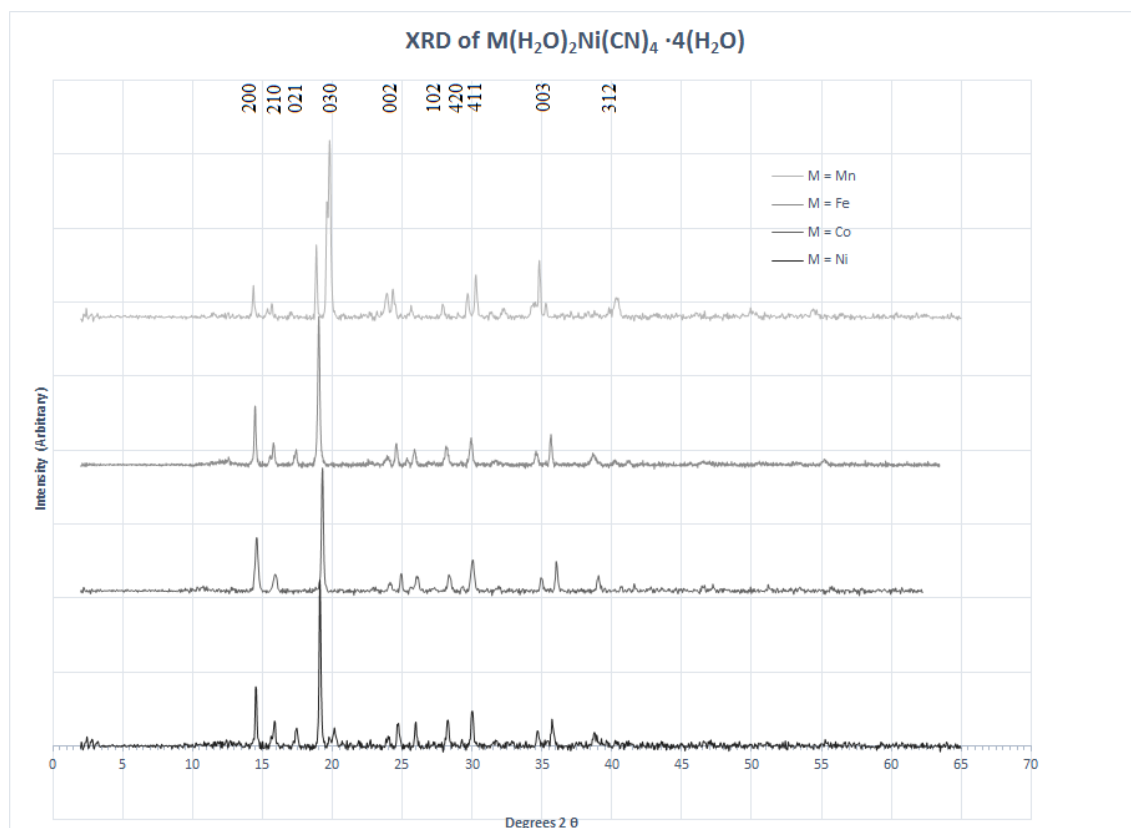


Figure 26. XRD powder diffraction patterns for the cyanide-bridged transition metal precipitates.

The peak positions for the cyanide-bridged transition metal complexes were in agreement with what is known from previous literature regarding the structure and atomic positions for these materials. The scans verified that these samples were the hexahydrated form. The location of the 003 peak at ~ 14 degrees 2θ in these samples indicates a distance of ~ 6.5 Å between adjacent layers. This is what is expected when water occupies the interlamellar space. Small variations in peak positions or absence of some peaks indicated the possibility of some distribution of other hydrated forms. The Appendix contains individual XRD patterns for these precipitated powders.

Scanning electron microscopy (SEM) was used to image these materials. The resolution of this SEM is capable of imaging an atomistically thick sheet. The sheet typically appeared as a dark area against a conducting background. Imaging against non-conducting surfaces is challenging. Often a sputter technique is required to give some conductivity to nonconductive surfaces. The images of the exfoliated sheets indicated that it was conductive material. Figure 27 reveals what is believed to be plate-like sheets about 0.5 μm in diameter. The sample was imaged on silicon and appears to be undergoing electron charging.

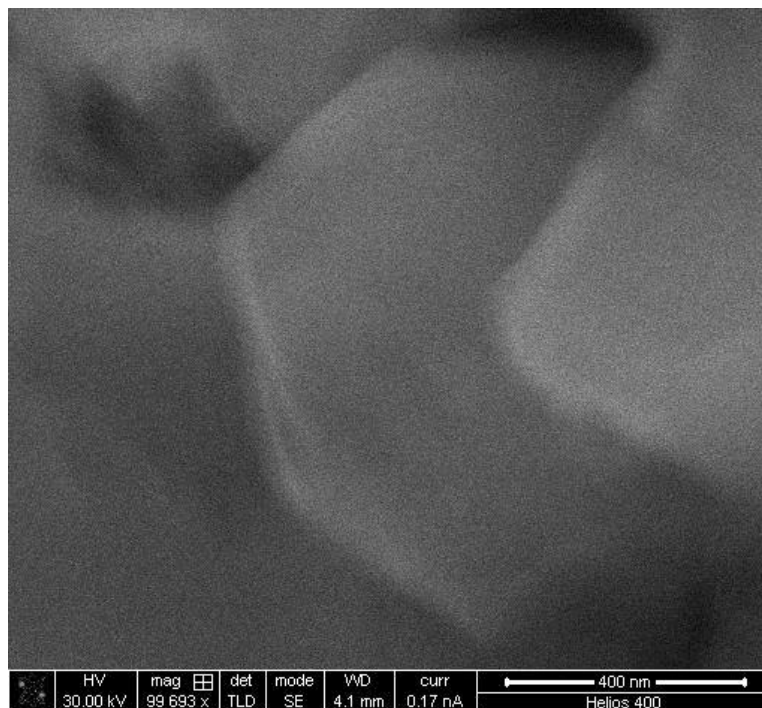


Figure 27. SEM image of thin plate-like sheets of the exfoliated material. The 500 nm diameter platelets had a shape similar to the single crystals grown when looking at them under a microscope.

4.3. Ion Selective Membrane Fabrication

The fabrication of ion selective membranes in this work ultimately yielded no success. Many aspects of fabrication were explored and a number of issues pertaining to the inability to produce an ion-selective or desalination membrane were identified.

Figure 28 is an SEM image of the substrate after attempting to deposit exfoliated powder using DDP as the exfolient and carrier liquid.

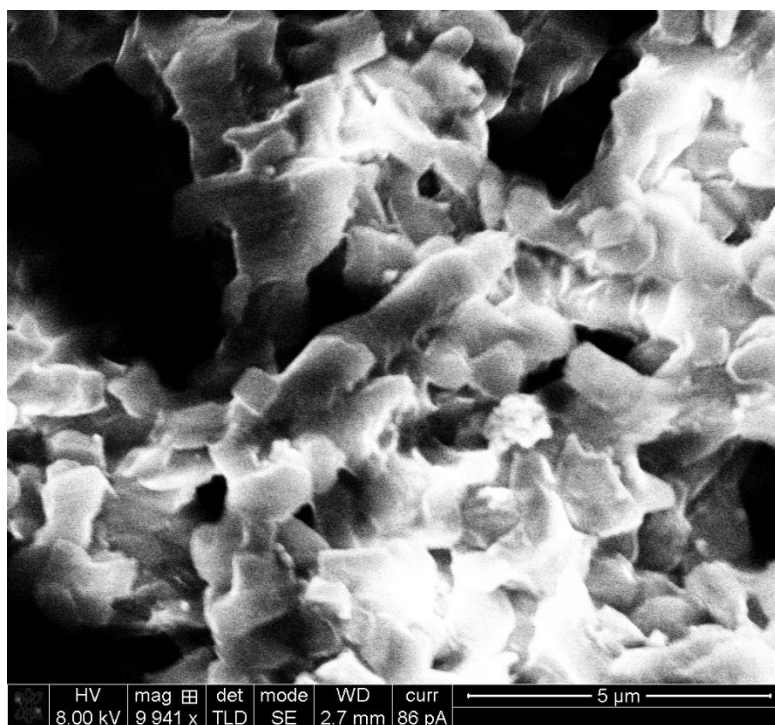


Figure 28. SEM image of the PVDF membrane after deposition of exfoliated $\text{Fe}(\text{H}_2\text{O})_2\text{Ni}(\text{CN})_4$ powder. No evidence of the single sheet membrane covering pore structure is present.

The pore openings are largely exposed. The sheet-like material coverage is incomplete. There is little evidence that the material was able to withstand the washing

following the fabrication method and may have washed out of, or through the pores in the support structure. The membrane material might be bunching up after water is reintroduced during washing. No method was identified that yielded a positive result.

4.4. Dehydration Stability Study

A study of dehydration stability in these materials was conducted to further analyze phenomena noticed by Nash *et al.* previously that may be an explanation why single crystal growth and X-ray crystallography of the $\text{Ni}(\text{H}_2\text{O})_2\text{Ni}(\text{CN})_4 \cdot 4\text{H}_2\text{O}$ has been problematic. If the structure variation that occurs when all of the transition metal components are the same element is responsible for poor single crystal growth, then identifying a pattern for hydration state stability could help to understand this. Hydration states can be seen by performing TGA runs at lower temperatures in the range of where water is evaporated. Precipitated powder samples were used in this analysis. Figure 29 is a TGA plot of $\text{Fe}(\text{H}_2\text{O})_2\text{Ni}(\text{CN})_4 \cdot 4\text{H}_2\text{O}$ from room temperature to 250 °C. The plot has been truncated at about 150 °C to show detail in the 1st derivative.

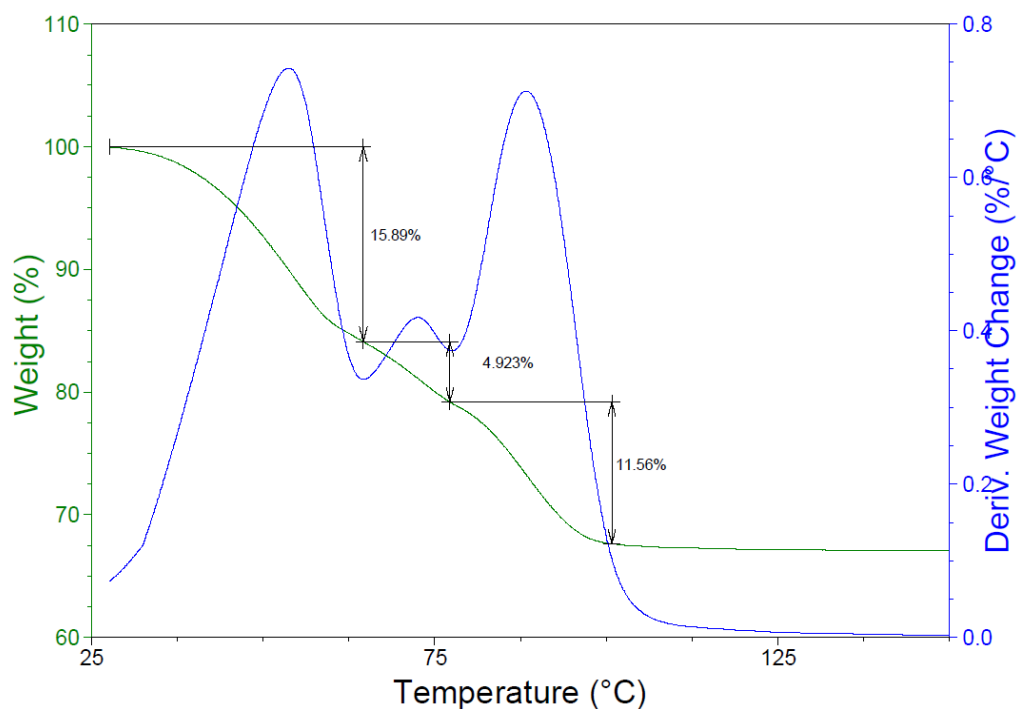


Figure 29. TGA Plot of $\text{Fe}(\text{H}_2\text{O})_2\text{Ni}(\text{CN})_4 \cdot 4\text{H}_2\text{O}$ showing dehydration events.

The first derivative curves of the mass loss curve revealed three distinct loss profiles. The cause of these different evaporation characteristics of water in an organometallic framework are position and bonding. The water loss around 50 °C represents water that is not coordinated and is mostly held by hydrogen bonding interactions and weak van der Waals interaction. The 2nd event is also non-coordinated water, but it has some bonding interaction or placement that is making it slightly harder to get out of the structure. The third evaporation event in the 80 °C range is water that has a more stable bonding arrangement and is likely water occupying the two coordination sites on the octahedral transition metal centers. By analysis of the mass loss % for each of these events, it appears to be a 3:1:2 (from lowest to highest temperature) ratio. This could fit the six waters of hydration seen in the molecular formula. The water

molecules from the first and second event are non-coordinated and enclathrated in the framework. The second loss event is a single molecule that is possibly slightly more bound by proximity to the coordinated water. The other cyanide-bridged transition metal complexes have different and unique dehydration characteristics as well. Figure 30 is a graph showing the relationship between the size of the framework (due to differences in atomic radii) and the dehydration profile for series of cyanide-bridged transition metal complexes.

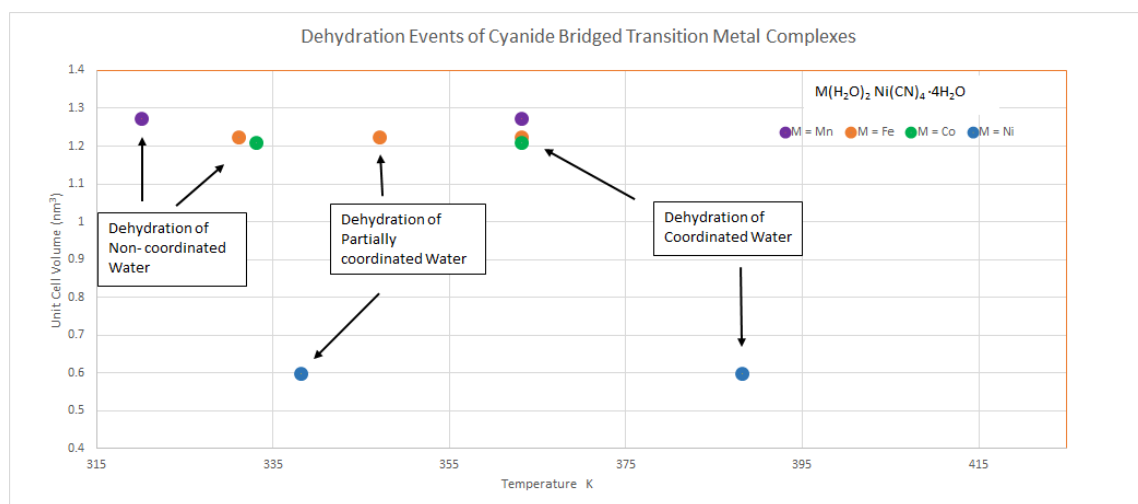


Figure 30. Plot of dehydration events, temperature vs. unit cell volume. The $\text{Ni}(\text{H}_2\text{O})_2\text{Ni}(\text{CN})_4 \cdot 4\text{H}_2\text{O}$ loses the coordinated water at considerably higher temperature than the others.

The $\text{Fe}(\text{H}_2\text{O})_2\text{Ni}(\text{CN})_4 \cdot 4\text{H}_2\text{O}$ complex is the only one that exhibits three dehydration events. This is due to an absence of interactions of enclathrated water so the water is lost in a 4:2 ratio in all complexes other than the iron containing one.

Another aspect of the dehydration experiment is the observation of sample color change. The $\text{Fe}(\text{H}_2\text{O})_2\text{Ni}(\text{CN})_4 \cdot 4\text{H}_2\text{O}$ and $\text{Mn}(\text{H}_2\text{O})_2\text{Ni}(\text{CN})_4 \cdot 4\text{H}_2\text{O}$ complexes turn

darker when dehydrated, but the $\text{Ni}(\text{H}_2\text{O})_2\text{Ni}(\text{CN})_4 \cdot 4\text{H}_2\text{O}$ and $\text{Co}(\text{H}_2\text{O})_2\text{Ni}(\text{CN})_4 \cdot 4\text{H}_2\text{O}$ have complete color change on dehydration. The di-nickel compound turns from light blue to tan or brown color while the cobalt containing sample turns from pink to dark purple. Figure 31 shows the color change. It was discovered that completely dehydrated complexes are not easily rehydrated in high humidity. An experiment was conducted on the color changing species where partial dehydration could be compared to full dehydration. Hydration states were determined by TGA contained in the Appendix.

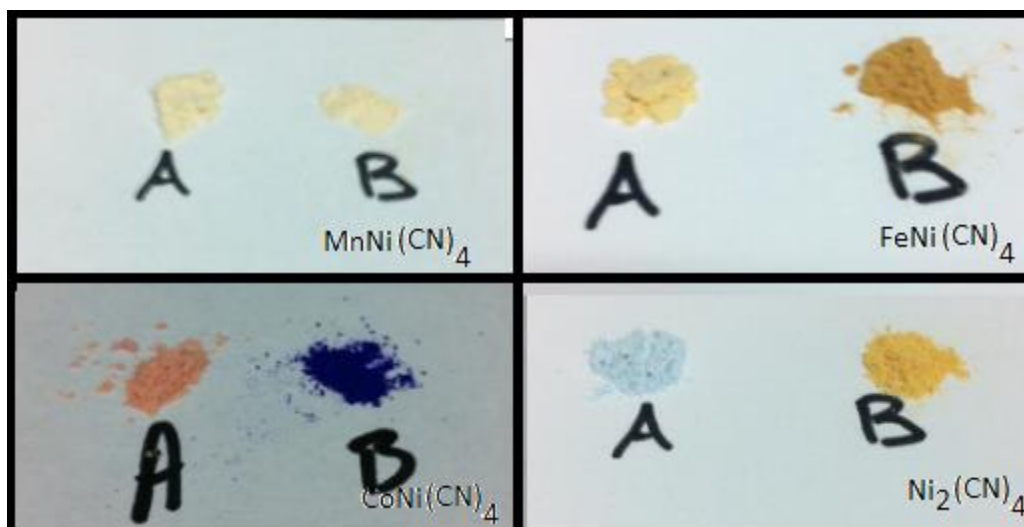


Figure 31. Color change on dehydration of cyanide-bridged transition metal precipitated powder. “A” is the fully hydrated form while “B” is the partially dehydrated form. Color change was found to be reversible with rehydration.

The trihydrate form of $\text{Fe}(\text{H}_2\text{O})_2\text{Ni}(\text{CN})_4 \cdot 4\text{H}_2\text{O}$ was able to be rehydrated after only being heated to the first event, but when heated beyond that complete rehydration was not possible. This effect was more marked in the $\text{Ni}(\text{H}_2\text{O})_2\text{Ni}(\text{CN})_4 \cdot 4\text{H}_2\text{O}$ complex where heating past the first dehydration event resulted in a change of color to tan, but

rehydration was possible in high humidity. If the second, high temperature event was passed then the color changed to a dark brown and was irreversible.

4.5. Magnetic Properties

The observation of magnetic properties in these materials were made through visually investigating the behavior. A small amount of the dry $\text{Fe}(\text{H}_2\text{O})_2\text{Ni}(\text{CN})_4 \cdot 4\text{H}_2\text{O}$ precipitated powder was placed onto a glass slide and moved into a magnetic field. No movement was observed that would suggest magnetic susceptibility. The larger single crystal pieces of $\text{Fe}(\text{H}_2\text{O})_2\text{Ni}(\text{CN})_4 \cdot 4\text{H}_2\text{O}$ were similarly tried and no movement occurred. This indicates that the material is either diamagnetic or the magnetic moment is too small to overcome surface friction. The powder samples were placed into DI water at a loading of 2% solids and shaken to disperse. The suspensions are unstable and complete settling occurred within 30 minutes. The powders were re-suspended and placed between the poles of a large horseshoe magnet. The magnetic field strength was estimated to be about 5000 Gauss (0.5 Tesla). Figure 32 shows two samples of the $\text{Fe}(\text{H}_2\text{O})_2\text{Ni}(\text{CN})_4 \cdot 4\text{H}_2\text{O}$ powder in water. The magnetic field directs powder to settle on the sidewalls of the container adjacent to the magnetic poles. In the absence of the field the powder settles straight down as influenced by gravity. This behavior was evident in the materials where $M = \text{Fe}$ or Mn in the general formula, $M(\text{H}_2\text{O})_2\text{Ni}(\text{CN})_4 \cdot 4\text{H}_2\text{O}$ but not when $M = \text{Ni}$, Co , or Zn . This trend followed the predictions of Nash *et al.* but the small magnetic susceptibilities expected might be too small to see even by this means.



Figure 32. Magnetic behavior in the precipitated powder. For the iron and manganese containing complexes a magnetic field was able to influence settling patterns. The image on the left is in a strong magnetic field while the right image is absent the field.

Small single crystal pieces were collected and similarly placed into DI water. The small crystals could be directed to the magnetic field and would move toward the poles. An attempt was made to establish if magnetic properties could orient the small crystals in a particular direction but no pattern was recognized at this scale. An experiment was conducted under the microscope using a small bar magnet but insufficient magnetic pull resulted in no movement.

The attraction of the powders and crystals to the poles of a large magnet indicates that the material contains a magnetic moment. The material could either be ferromagnetic, antiferrimagnetic, or paramagnetic. If the material exhibits either

ferromagnetic, or antiferromagnetic it should be possible to induce the material to retain its own magnet field even when removed from the large magnet. This property was tested by leaving the samples in the magnetic field of the large magnet for 48 hours then bringing a demagnetized steel bar in contact with the suspended powder and looking for attraction. Figure 33 is a photograph of the experimental technique for determining ferromagnetism at room temperature.

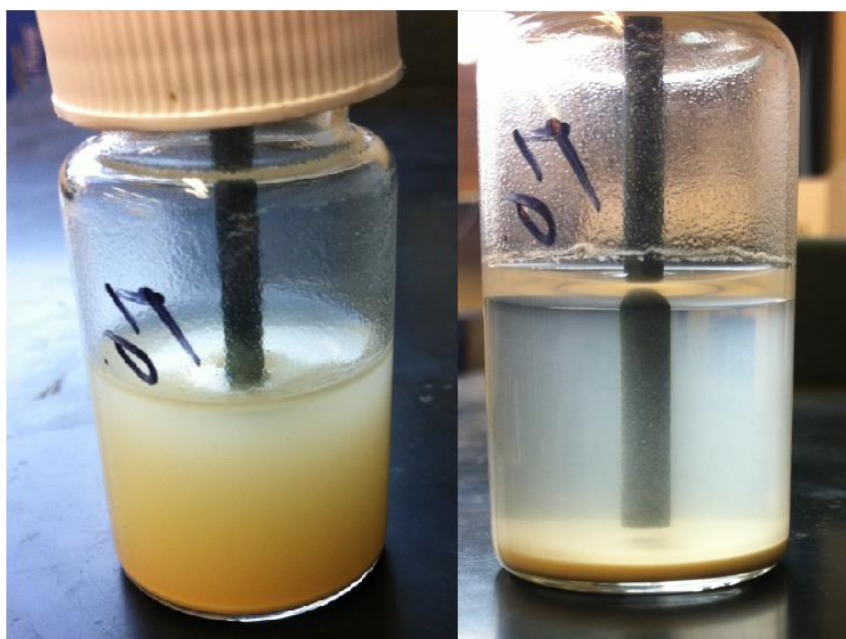


Figure 33. Ferromagnetic suspension test of suspended powder in water. The image is of the suspension of $\text{Fe}(\text{H}_2\text{O})_2\text{Ni}(\text{CN})_4 \cdot 4\text{H}_2\text{O}$ powder before (left) and after (right) settling. No magnetic properties were evident.

The magnetic properties were further investigated by using the TGA to look for small mass changes. Two experiments were conducted on all of the powder species. The first was a ramp of temperature from room temperature to 250 °C while in the magnetic field. An abrupt change in the mass loss curve during the run would indicate a

dependence on temperature. There was no indication of a change in any of samples run. Literature examples of similar materials indicate that a Néel temperature is present at temperatures in the range of 2-10 K.⁹ It is unlikely that any antiferromagnetic behavior is evident at room temperature and it would appear that if the material has a Curie temperature it is above the materials degradation temperature.

The second experiment was carried out in isothermal configuration. The objective was to look at quantifiable mass changes at 30 °C and 150 °C. This was accomplished by ramping the sample to the isothermal temperature and then placing it in the magnet field for a length of time and then removing it. The offset of mass on the mass loss curve could be used to comparatively assess the strengths of the magnetic fields. Figure 34 is a TGA plot of this type. The x-axis of the plot, which is normally temperature, is changed to show time.

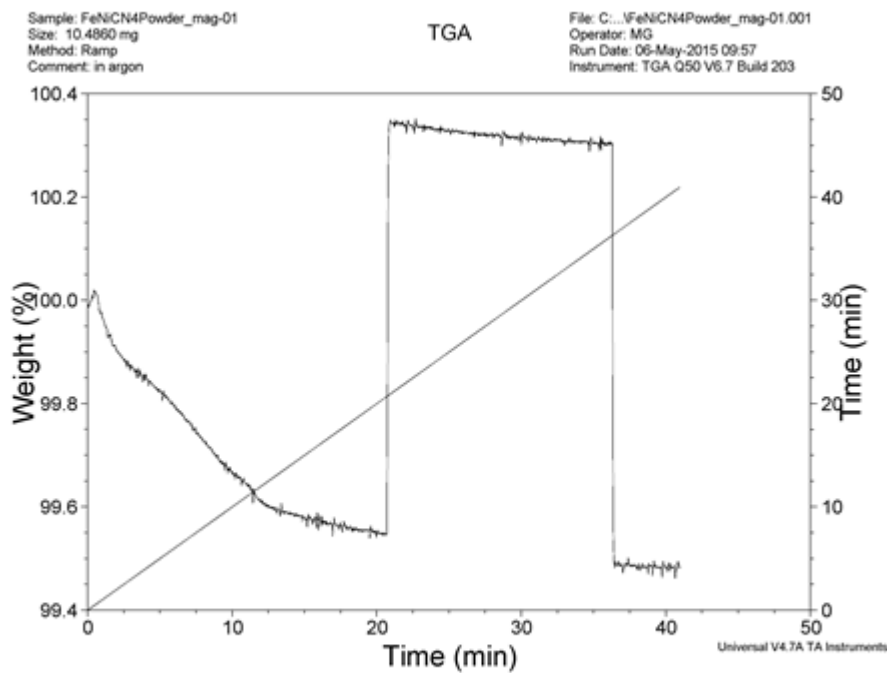


Figure 34. TGA plot of the influence of a magnetic field on the precipitated powders. The x-axis is displaying the time regime.

The sudden increase in mass on the curve occurred when the magnetic field was activated. The drop in mass approximately 15 minutes later is the deactivation of the magnetic field. Interestingly, a small amount of mass loss was recorded when the empty pan was run but was deemed negligible since the experiment was comparative. The relative mass change was calculated from the data. Table 8 shows the results of the TGA isothermal experiments.

Table 8. Mass change in the isothermal samples under a magnetic field.

	Mass $\Delta\%$ @ 30 °C	Mass $\Delta\%$ @ 150 °C
$\text{Fe}(\text{H}_2\text{O})_2 \text{Ni}(\text{CN})_4 \cdot 4\text{H}_2\text{O}$	1.000	0.805
$\text{Mn}(\text{H}_2\text{O})_2 \text{Ni}(\text{CN})_4 \cdot 4\text{H}_2\text{O}$	0.660	0.585
$\text{Zn}(\text{H}_2\text{O})_2 \text{Ni}(\text{CN})_4 \cdot 4\text{H}_2\text{O}$	0.555	0.420
$\text{Ni}(\text{H}_2\text{O})_2 \text{Ni}(\text{CN})_4 \cdot 4\text{H}_2\text{O}$	0.480	0.380

The magnetic attractive force is greater in the $\text{Fe}(\text{H}_2\text{O})_2\text{Ni}(\text{CN})_4 \cdot 4\text{H}_2\text{O}$ and $\text{Mn}(\text{H}_2\text{O})_2\text{Ni}(\text{CN})_4 \cdot 4\text{H}_2\text{O}$ samples than the others. This corroborates the observed visual findings. A trend was evident that suggests the magnetic effects are reduced with elevated temperature. This is consistent with reported behavior of magnetic materials in general since elevated temperature causes electron orbital expansion, separating electrons from each other slightly, reducing the influence on each other, thus decreasing the magnetic moments. This method seems to indicate that all of these complexes exhibit paramagnetic or ferromagnetic behavior. None are diamagnetic.

The magnetic hysteresis loops were obtained for the precipitated crystals of $\text{Fe}(\text{H}_2\text{O})_2\text{Ni}(\text{CN})_4 \cdot 4\text{H}_2\text{O}$ and $\text{Ni}(\text{H}_2\text{O})_2\text{Ni}(\text{CN})_4 \cdot 4\text{H}_2\text{O}$. Both complexes exhibit small ferromagnetic properties. The $\text{Fe}(\text{H}_2\text{O})_2\text{Ni}(\text{CN})_4 \cdot 4\text{H}_2\text{O}$ was found to be more ferromagnetic with a magnetic saturation of 0.004332 emu/g. The $\text{Ni}(\text{H}_2\text{O})_2\text{Ni}(\text{CN})_4 \cdot 4\text{H}_2\text{O}$ sample had a magnetic saturation of 0.00692 emu/g. The magnetic remanence for both of the complexes was unable to be determined due to the low response in these materials. Figure 35 shows the magnetic hysteresis loops for the $\text{Fe}(\text{H}_2\text{O})_2\text{Ni}(\text{CN})_4 \cdot 4\text{H}_2\text{O}$ and $\text{Ni}(\text{H}_2\text{O})_2\text{Ni}(\text{CN})_4 \cdot 4\text{H}_2\text{O}$ precipitated complexes.

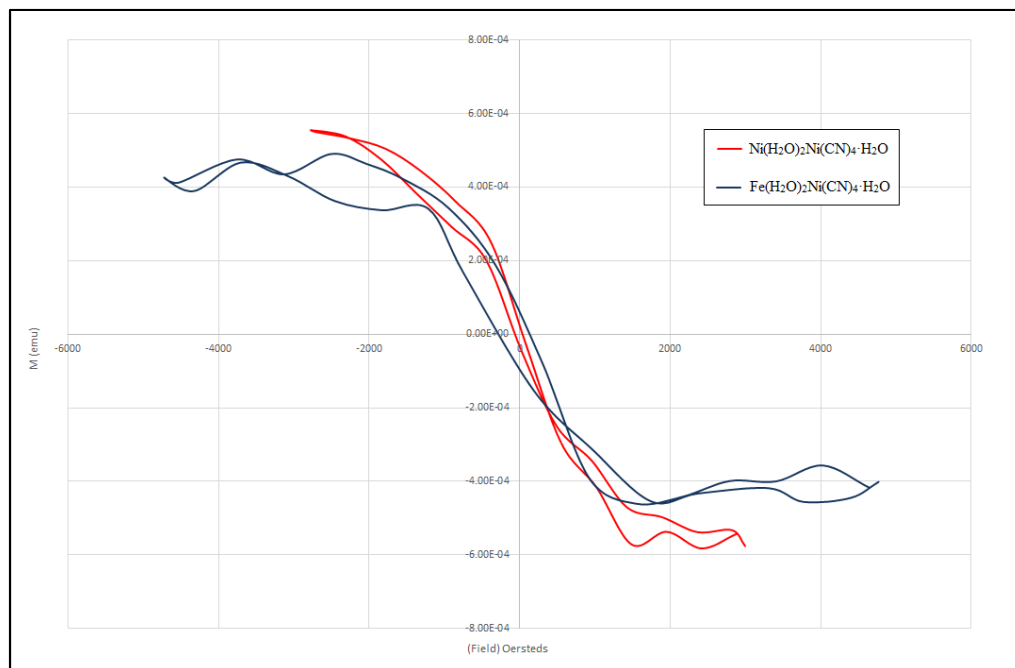


Figure 35. Vibrational sample magnetometer hysteresis loops. Data for the $\text{Fe}(\text{H}_2\text{O})_2\text{Ni}(\text{CN})_4 \cdot 4\text{H}_2\text{O}$ and $\text{Ni}(\text{H}_2\text{O})_2\text{Ni}(\text{CN})_4 \cdot \text{H}_2\text{O}$ precipitated complexes reveals a slight ferromagnetic characteristic.

Coercivity was not determined here because only a single loop was performed.

The samples were evaluated at room temperature. It was necessary to subtract the magnetic response of the plastic sample holder to obtain an accurate measure of magnetic susceptibility.

CHAPTER 5

CONCLUSIONS

5.1. Summary

There were three main goals in this study. The first was to model 2D and 3D structures of cyanide-bridged transition metal complexes for the purpose of determining the possibility of using these sheet-like, single atom thick membranes to desalinate seawater and other ion selective applications. Models were constructed based on crystallographic data and modified to the single layer structure which occurs during exfoliation of the material. This single layer structure was used in a model where water, sodium ions and chloride ions were placed under pressure by manipulating a rigid piston and were directed toward these membranes. The work revealed that the membranes were effective at separation of salt from water at qualitatively reasonable pressures.

The second goal was to produce viable membranes for study in the lab and for verification of the computational approach. Although the membranes produced in the laboratory failed to desalinate water, the pursuit did reveal a phenomenon regarding the mechanism of dehydration in both the single crystal material and the precipitated powder. This study has shown that the identity of the transition metal does effect the stability of the hydrated structure.

The third goal was to verify the existence of a magnetic moment in these materials. This was demonstrated in some of the materials, but others had magnet

properties that were either too small to observe or some of the complexes are diamagnetic as was predicted.

5.2. Future Work

Continuation of this work provides a large number of paths to investigate. This work in general was limited in both time and scope. Unfortunately the task of providing a functional membrane material that verifies the predictions seen using molecular dynamic simulations was not accomplished. In follow on work there are several key areas where development has come up short. A select list of these characteristics requires further investigation:

- Complete the development of a long range 2D sheet that is relatively free of defects.
- Determine if the 2D membrane material is stable and can adhere to the support structure enough to prevent being damaged or completely washed away by the RO pressures applied.
- Provide a thorough analysis of the membrane selectivity and antifouling characteristics experimentally.
- Provide data for a system working with actual brine or saline water containing the variety of dissolved solids seen outside laboratory controls.
- Determine the feasibility of implementing production techniques to the fabrication of a 2D membrane from these materials.

- Prove that the material can be produced consistently and without expensive practices that negate any gains made in performance.

In terms of molecular dynamics simulation, the analysis could benefit from study on a more accurate water model than what was used in the UFF. The model's platform was limited in computational and graphical display power. A system capable of modeling behavior with a much larger number of atoms would provide more reliable data regarding characteristics and performance.

The magnetism study has opened the door to more applications of the materials. Aside from improving our fundamental understanding of the magnetic properties in these high-spin materials, study could focus on determining how magnetic properties are effected by exfoliation into individual sheets. A pertinent question is: what relationship does the magnetic field have to the crystal orientation? If the field is oriented along crystal growth in any particular way, it could lead to the use of magnetism for fabrication or application of the membrane by using the magnetization to direct growth. An electronic property study to determine the conditions at which the material may conduct electricity or behave as a semiconductor would be another area of interest.

APPENDIX SECTION

Crystallographic Data

Fe(H₂O)₂ Ni(CN)₄ ·4H₂O		Fe(H₂O)₂Ni(CN)₄·H₂O	
Empirical Formula		Empirical Formula	
C ₄ H ₁₂ Fe ₄ Ni ₄ O ₆		C ₄ H ₆ Fe ₄ Ni ₄ O ₃	
Formula Weight	329.617	Formula Weight	272.66
Crystal Color, Habit		Crystal Color, Habit	
colorless, prism		colorless, prism	
Temperature 20.0°C		Temperature 20.0°C	
Crystal Dimensions		Crystal Dimensions	
0.79 X 0.45 X 0.33 mm		0.27 X 0.22 X 0.13 mm	
Crystal System	Orthorhombic	Crystal System	Orthorhombic
Lattice Type	Primitive	Lattice Type	I-Center
Lattice Parameters		Lattice Parameters	
a = 12.0962(7) Å		a = 7.2153(10) Å	
b = 14.0037(8) Å		b = 14.3801(18) Å	
c = 7.2250(4) Å		c = 8.9471(12) Å	
V = 1223.86(12) Å ³		V = 928.3(2) Å ³	
Space Group	Pnma (#62)	Space Group	Imma (#74)
Z value	4	Z value	4
Dcalc	1.773 g/cm ³	Dcalc	1.951 g/cm ³
F(000)	664	F(000)	544
μ(MoKα)	27.403 cm ⁻¹	μ(MoKα)	35.692 cm ⁻¹

Crystallographic Data Cont.

Reflections Collected	11906
Independent Reflections	1465 (Rint = 0.0240)
Observations ($I > 2.00\sigma(I)$)	1409
Variables	79
Reflection/Parameter Ratio	17.84
Refinement Method	
Full-matrix least-squares on F	
Function Minimized	
$\sum w (F_o - F_c)^2$	
Least Squares Weights	
Chebyshev polynomial with 3 parameters	
3.6881, 0.7577, 2.4643	
2 θ max cutoff	55.0°
Anomalous Dispersion	
All non-hydrogen atoms	
Residuals: R ($I > 2.00\sigma(I)$)	0.0285
Residuals: wR ($I > 2.00\sigma(I)$)	0.026
Goodness of Fit Indicator	0.995
Max Shift/Error in Final Cycle	0
Maximum peak in Final Diff. Map	
0.83 e-/Å ³	
Minimum peak in Final Diff. Map	
-0.88 e-/Å ³	

Reflections Collected	4510
Independent Reflections	593 (Rint = 0.0548)
Observations ($I > 2.00\sigma(I)$)	546
Variables	37
Reflection/Parameter Ratio	14.76
Refinement	
Full-matrix least-squares on F	
Function Minimized	
$\sum w (F_o - F_c)^2$	
Least Squares Weights	
Chebyshev polynomial with 3 parameters	
6.2750, 0.8991, 4.6084	
2 θ max cutoff	54.9°
Anomalous Dispersion	
All non-hydrogen atoms	
Residuals: R ($I > 2.00\sigma(I)$)	0.0475
Residuals: wR ($I > 2.00\sigma(I)$)	0.0543
Goodness of Fit Indicator	1.083
Max Shift/ Error in Final Cycle	0
Maximum peak in Final Diff. Map	
1.37 e-/Å ³	
Minimum peak in Final Diff. Map	
-1.40 e-/Å ³	

Crystallographic Data Cont.

Mn(H₂O)₂ Ni(CN)₄ · 4H₂O

Empirical Formula

C₄H₁₂MnN₄NiO₆

Formula Weight 328.708

Crystal Color, Habit

colorless, prism

Temperature 20.0°C

Crystal Dimensions

0.79 X 0.45 X 0.33 mm

Crystal System Orthorhombic

Lattice Type Primitive

Lattice Parameters

a = 12.311(6) Å

b = 14.134(6) Å

c = 7.313(3) Å

V = 1272.5(10) Å³

Space Group Pnma (#62)

Z value 4

Dcalc 1.773 g/cm³

F(000) 664

μ(MoKα) 27.403 cm⁻¹

Reflections Collected 2431

Independent Reflections 1854 (Rint = 0.1724)

Observations (I > 2.00σ(I)) 1409

Crystallographic Data Cont.

$\text{Ni}(\text{H}_2\text{O})_2 \text{Ni}(\text{CN})_4 \cdot 4\text{H}_2\text{O}$

Empirical Formula

$\text{C}_4\text{H}_{12}\text{N}_4\text{Ni}_2\text{O}_6$

Formula Weight 332.46

Crystal Color, Habit

colorless, prism

Temperature 20.0°C

Crystal Dimensions

0.79 X 0.45 X 0.33 mm

Crystal System Orthorhombic

Lattice Type Primitive

Lattice Parameters

$a = 7.26 \text{ \AA}$

$b = 14.20 \text{ \AA}$

$c = 8.88 \text{ \AA}$

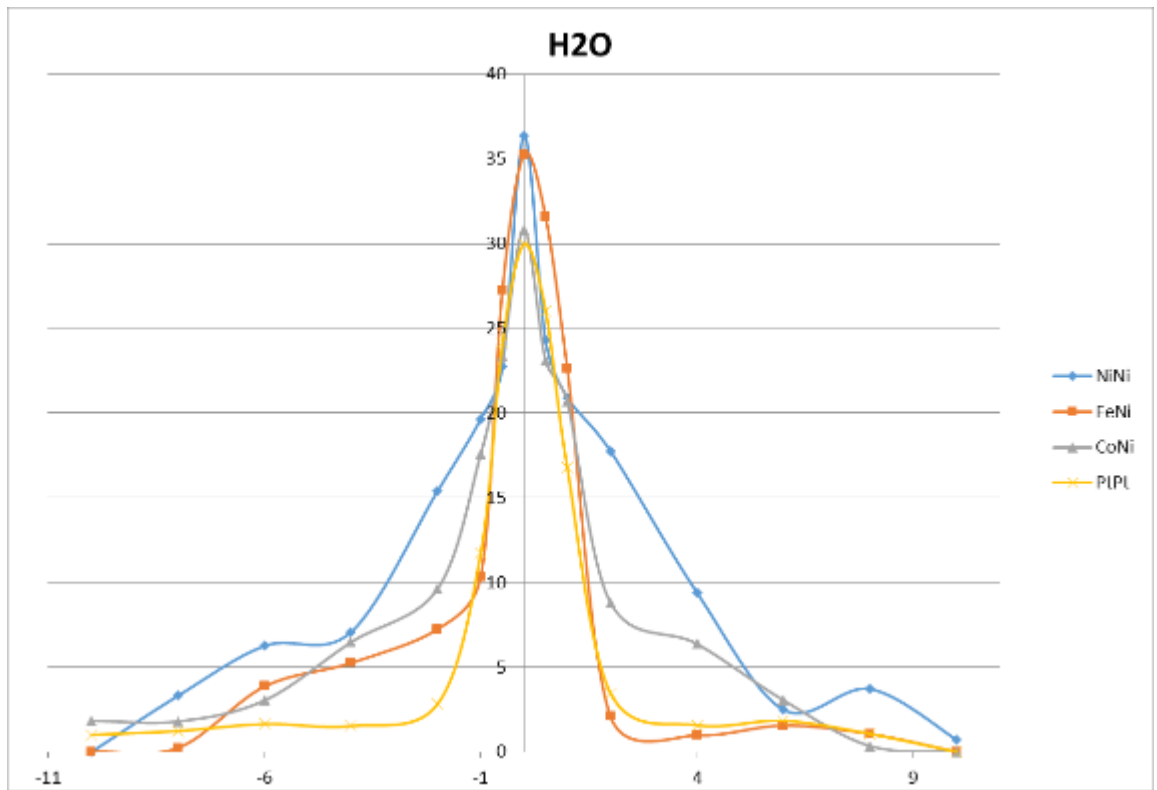
$V = 915.457 \text{ \AA}^3$

Space Group Pnma (#62)

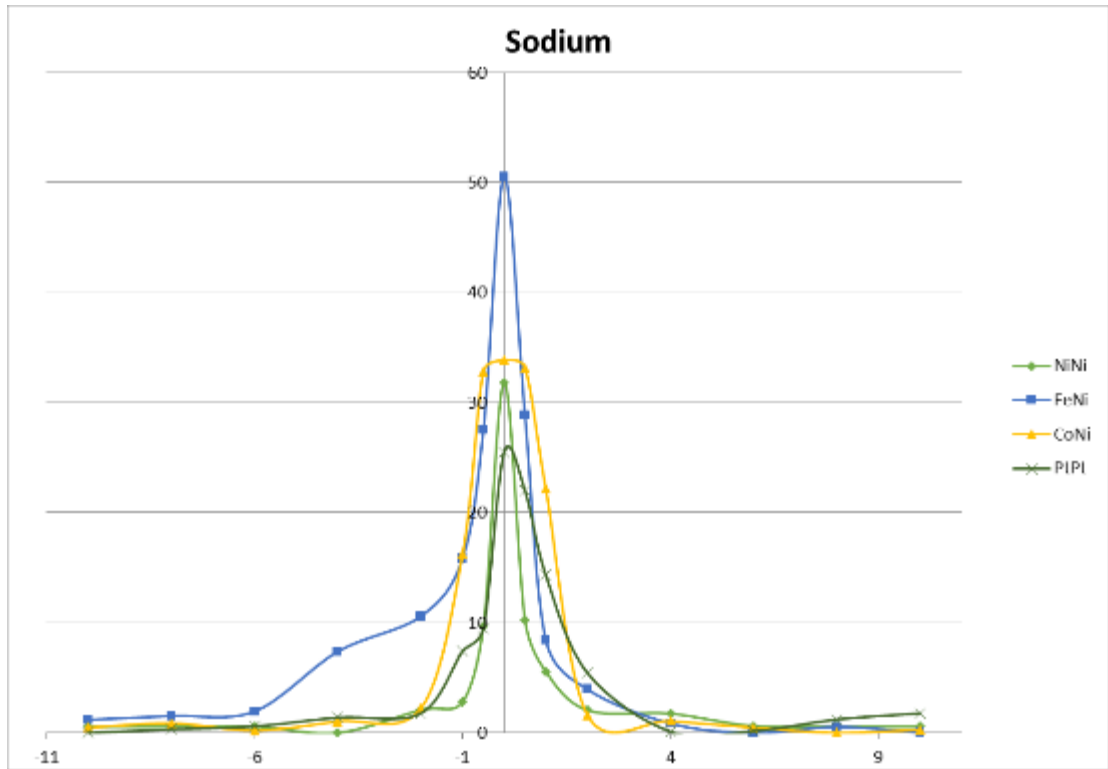
Chemicals Used In This Research

Name	Formula	Supplier	Grade	CAS #	Mol Wt. (g/mol)
potassium tetracyanonickelate(II) hydrate	$K_2Ni(CN)_4 \cdot xH_2O$	Sigma Aldrich	ACS 99%	339527-86-5	240.96
nickel(II) sulfate	$NiSO_4 \cdot 6H_2O$	Sigma Aldrich	ACS 99%	10101-97-0	262.85
Ammonium iron(II) sulfate hexahydrate	$(NH_4)_2Fe(SO_4)_2 \cdot 6H_2O$	ScholAR Chem.	Reagent	7783-85-9	392.14
cobalt(II) chloride hexahydrate	$CoCl_2 \cdot 6H_2O$	Sigma Aldrich	ACS 98%	7791-13-1	237.93
Zinc(II) chloride, anhydrous	$ZnCl_2$	Sigma Aldrich	ACS Reagent 97%	7646-85-7	136.3
Zinc(II) sulfate heptahydrate	$ZnSO_4 \cdot 7H_2O$	Sigma Aldrich	ACS Reagent Plus	7446-20-0	287.56
Manganese(II) sulfate monohydrate	$MnSO_4 \cdot H_2O$	Sigma Aldrich	ACS Reagent Plus	10034-96-5	169.02
Manganese(II) chloride	$MnCl_2$	Alfa Aesar	Reagent	7773-01-5	125.84
1-Dodecyl-2-pyrrolidinone	$C_{16}H_{31}NO$	ISP Technologies	(LP-300)	2687-96-9	253.42
acetone					
ethyl alcohol					
isobutanol					
ethyl acetate					

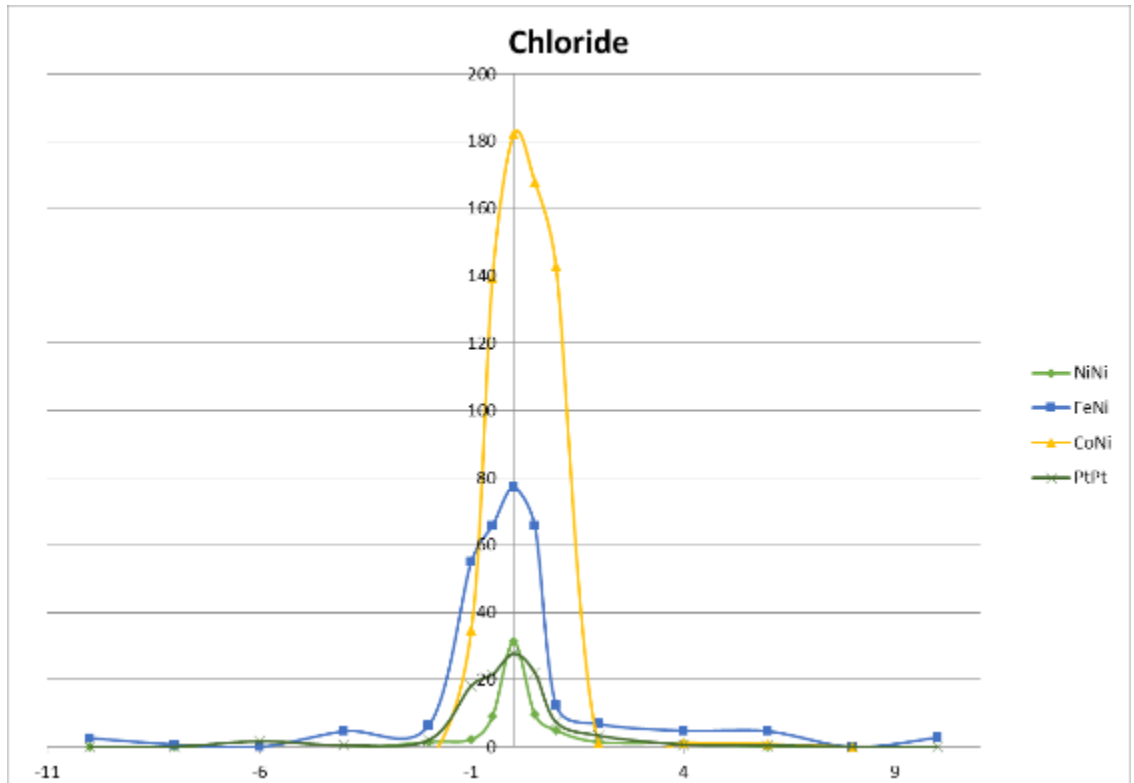
Energy Profile Charts



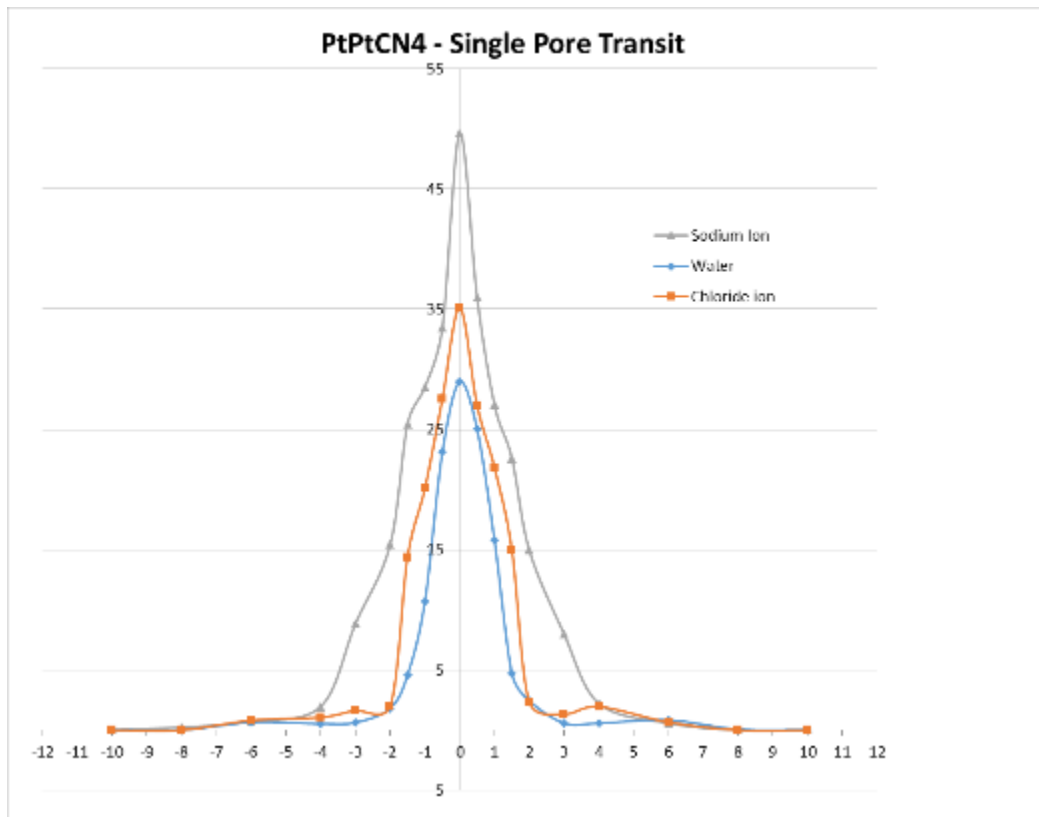
Energy Profile Charts Cont.



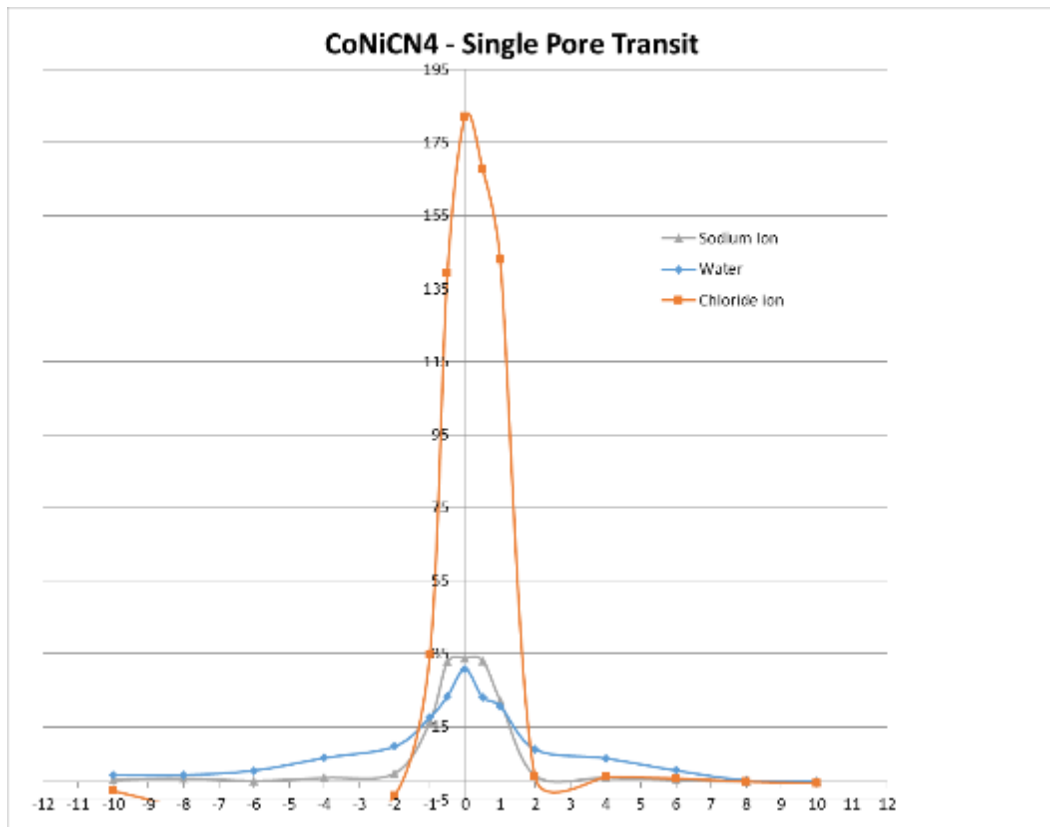
Energy Profile Charts Cont.



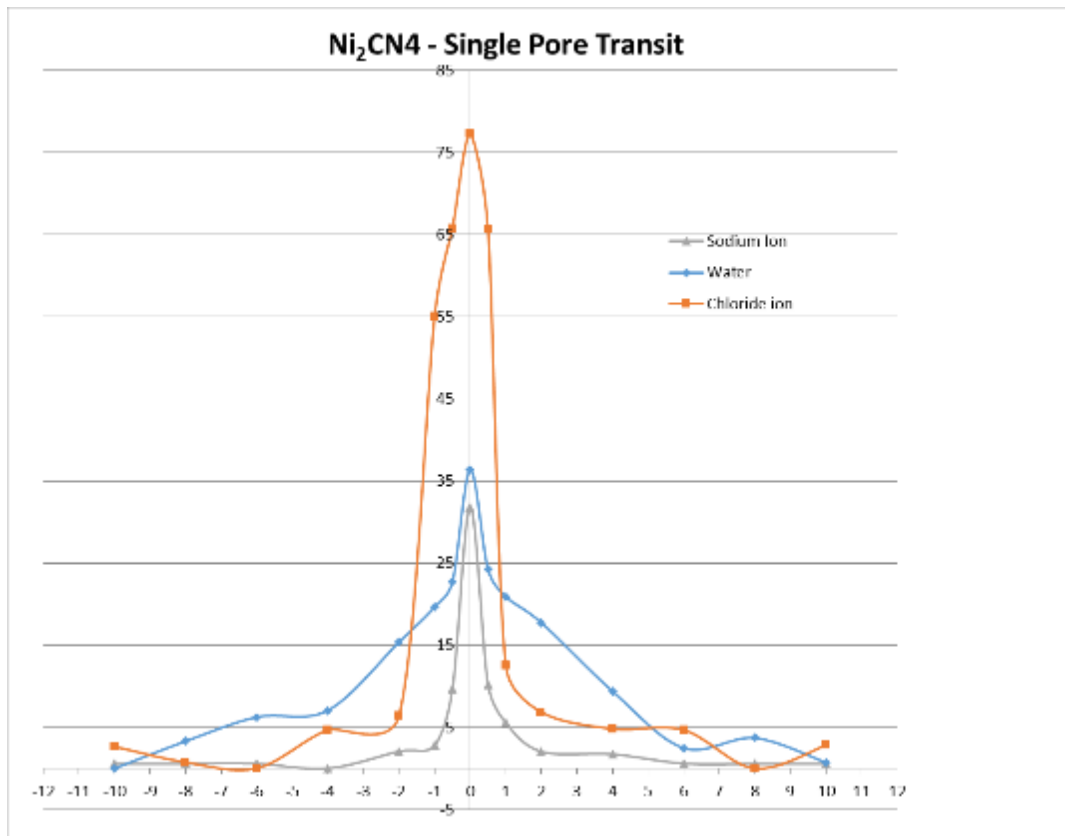
Energy Profile Charts Cont.



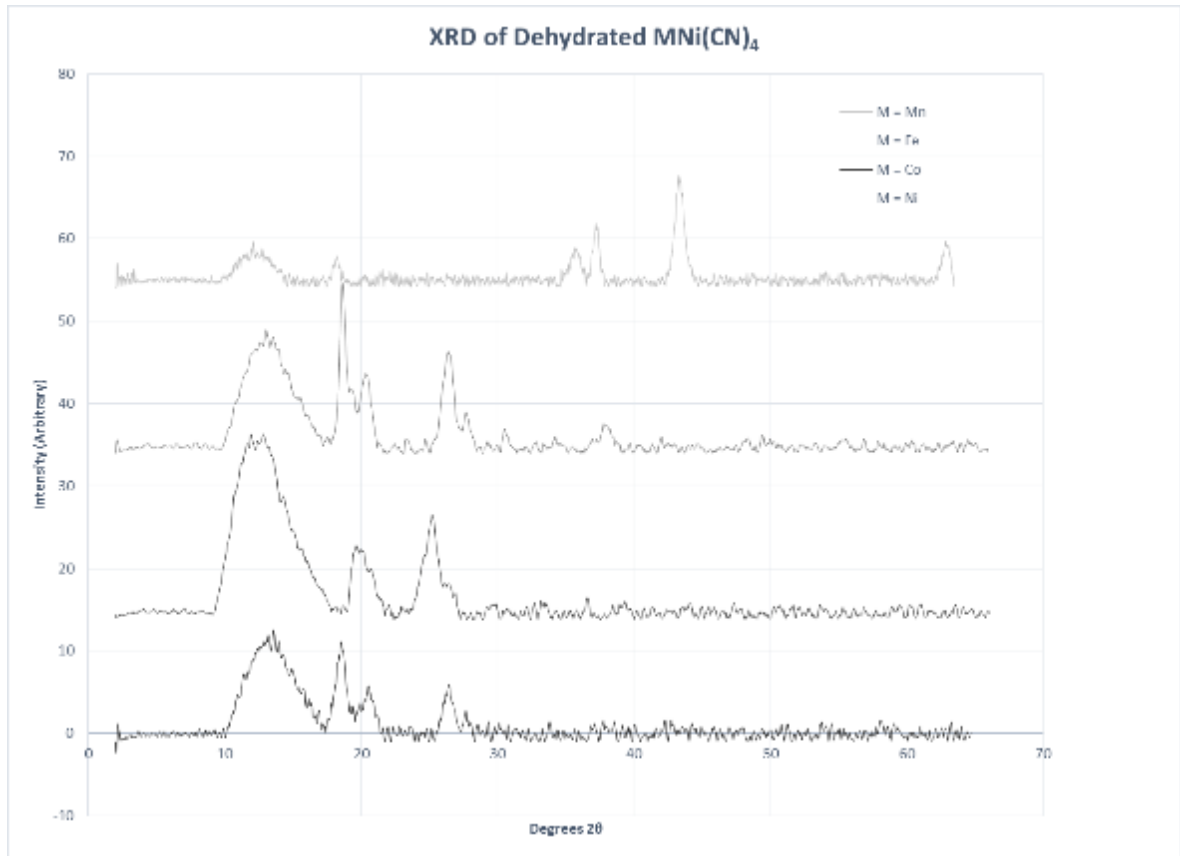
Energy Profile Charts Cont.



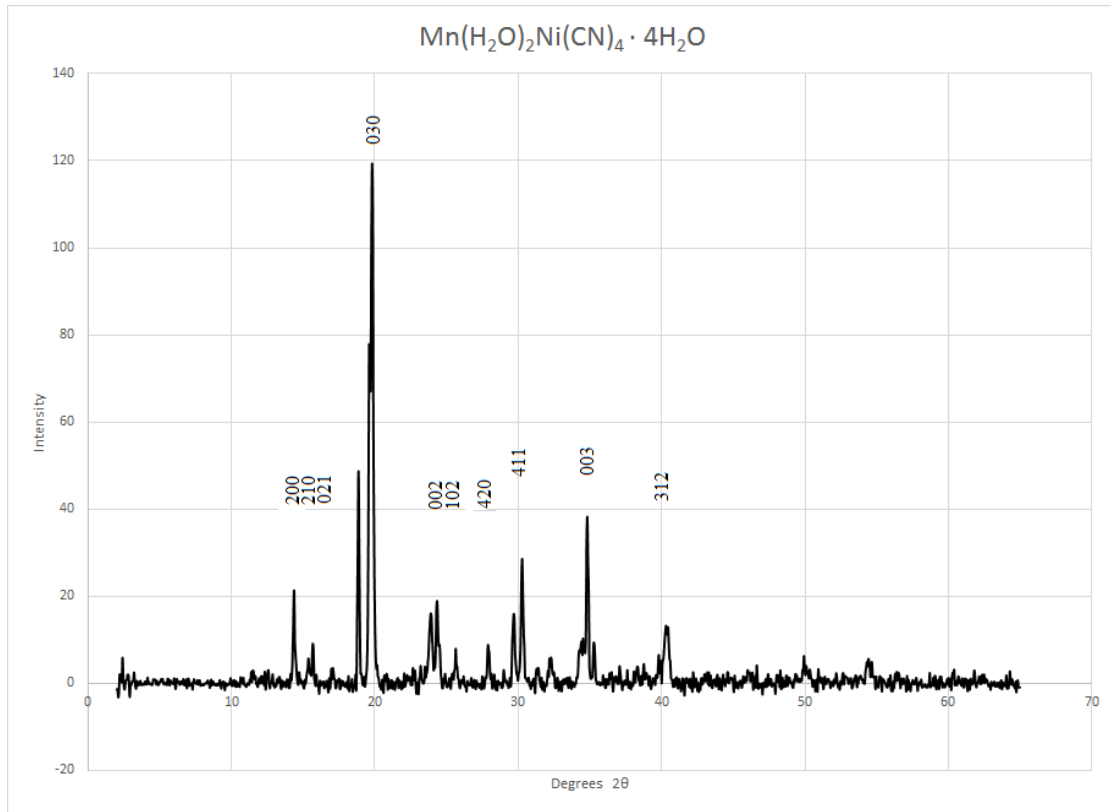
Energy Profile Charts Cont.



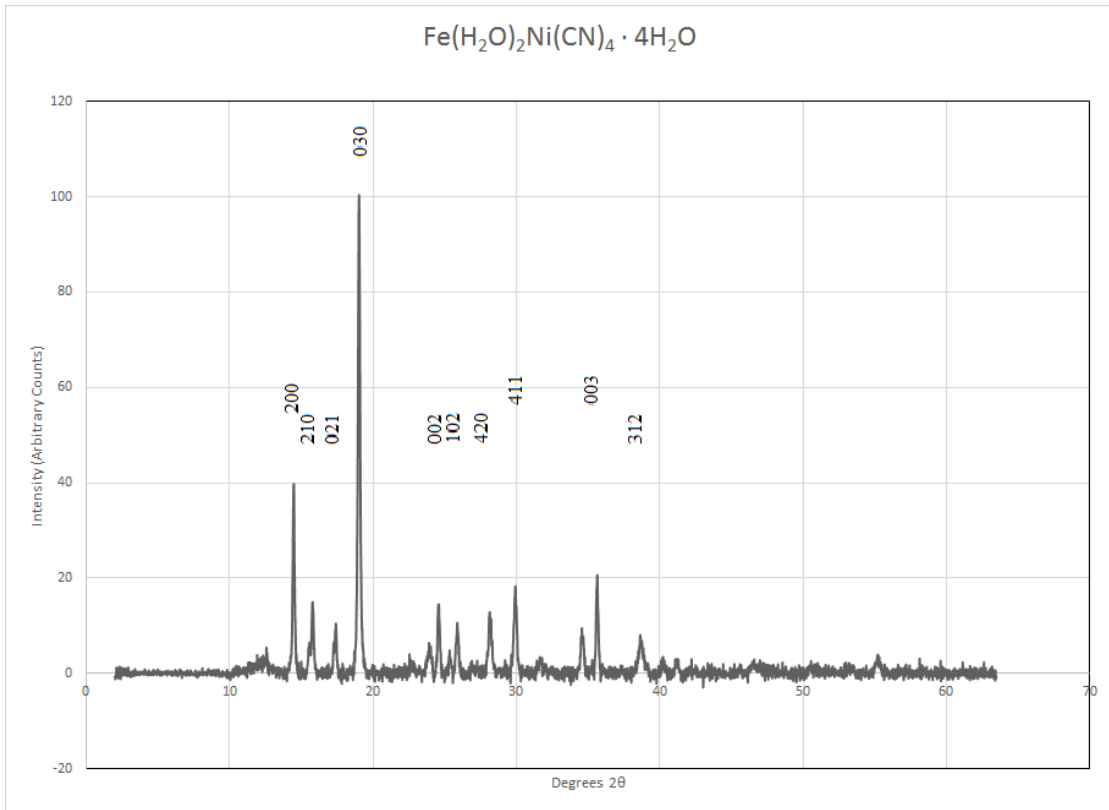
Wide Angle X-ray Diffraction (WXR) Data



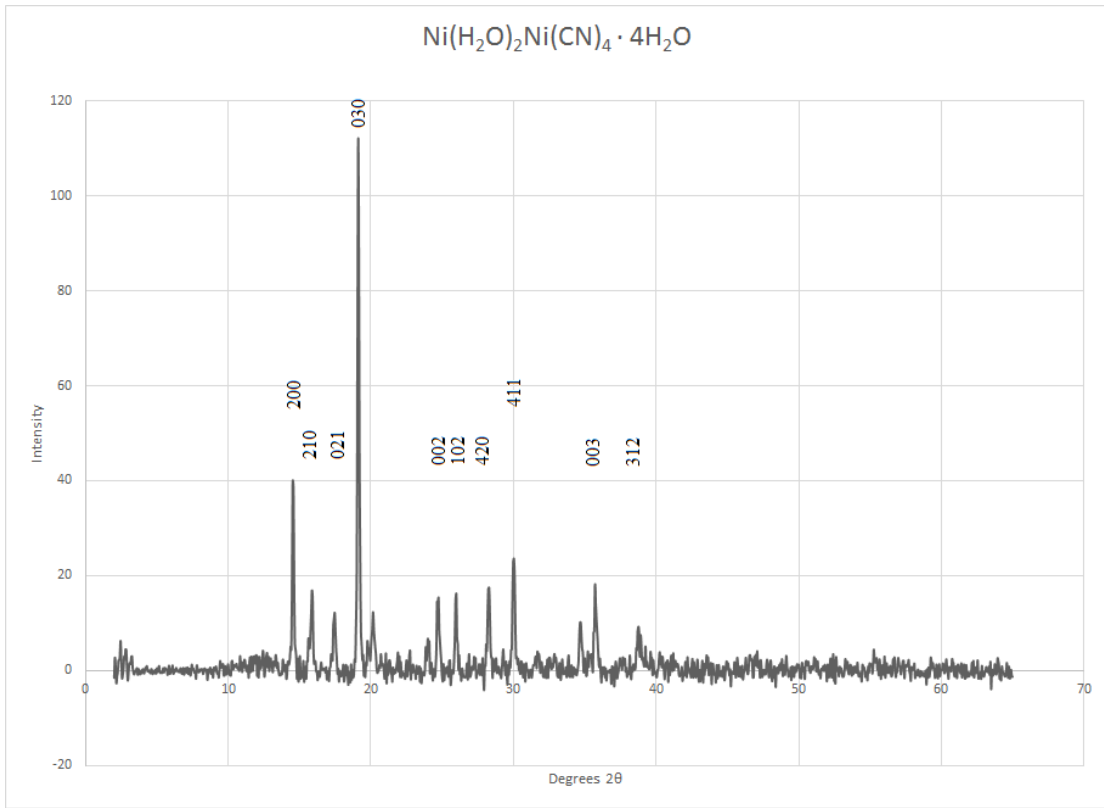
WXRD Data Cont.



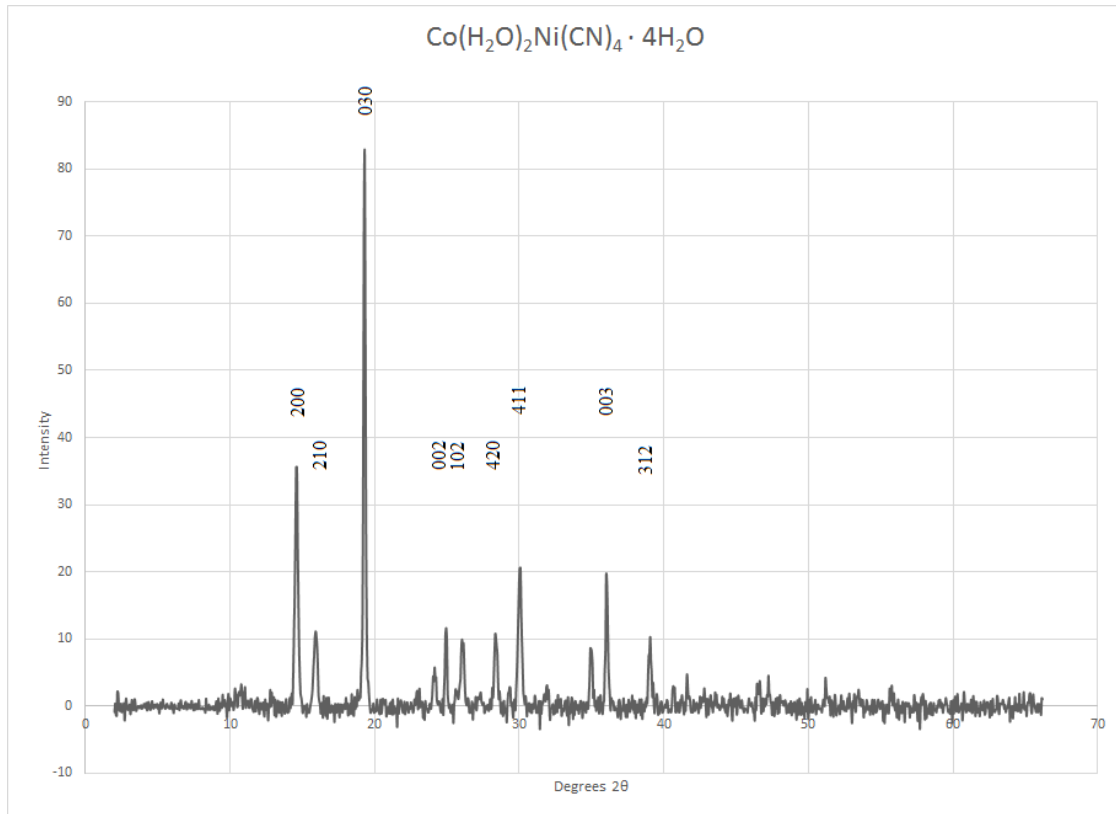
WXR Data Cont.



WXR Data Cont.

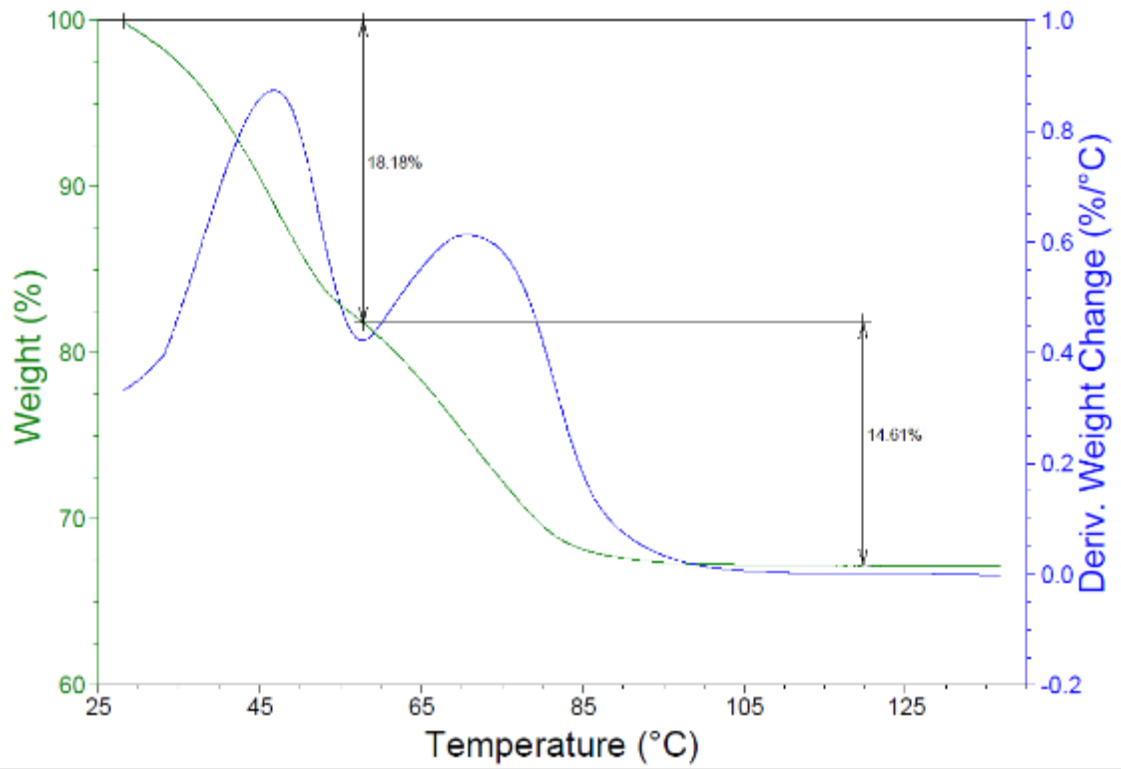


WXR Data Cont.



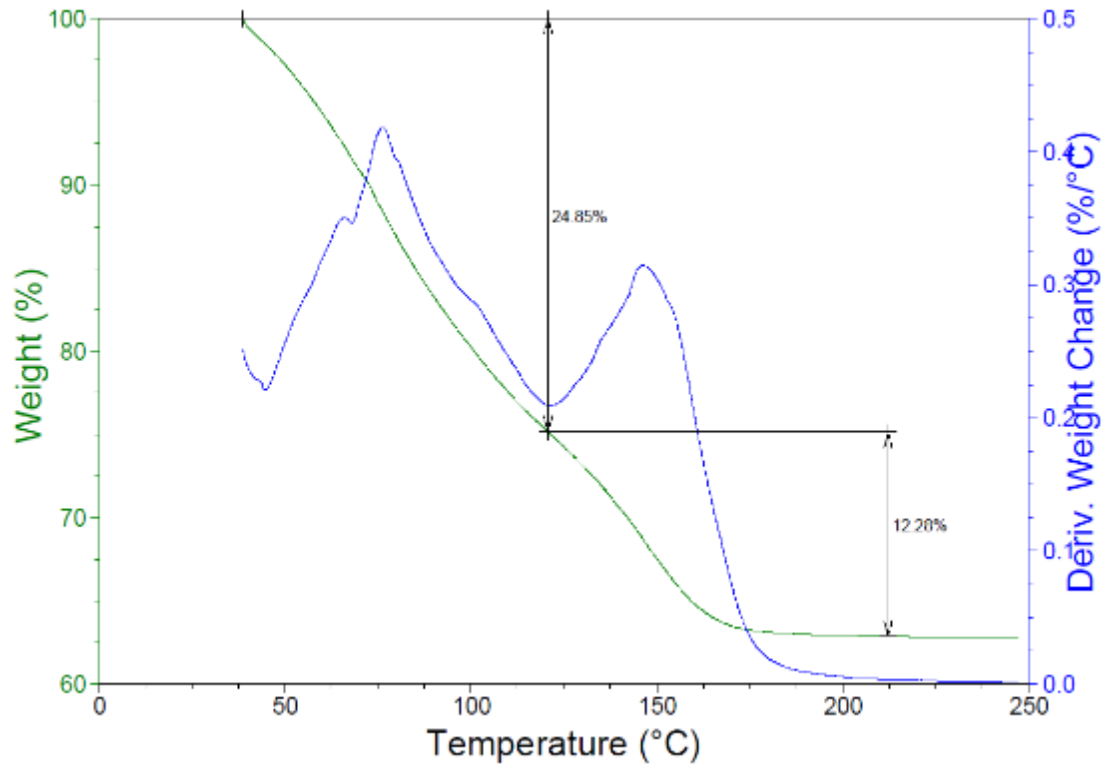
Thermal Gravimetric Analysis (TGA) – Hydration Data

MnNiCN4



TGA – Hydration Data

Ni₂CN₄



LITERATURE CITED

- (1) Dunbar, K. R.; Heintz, R. A. In *Progress in Inorganic Chemistry*; John Wiley & Sons, Inc.: 2007, p 283.
- (2) Buffagni, S.; Vallarino, L. M.; Quagliano, J. V. *Inorganic Chemistry* **1964**, 3, 480.
- (3) Iwamoto, T. *J Incl Phenom Macrocycl Chem* **1996**, 24, 61.
- (4) Bell, C. M.; Arendt, M. F.; Gomez, L.; Schmehl, R. H.; Mallouk, T. E. *Journal of the American Chemical Society* **1994**, 116, 8374.
- (5) Wang, S.; Ding, X.-H.; Li, Y.-H.; Huang, W. *Coordination Chemistry Reviews* **2012**, 256, 439.
- (6) Iwamoto, T. *J Mol Struct* **1981**, 75, 51.
- (7) Anno, H.; Hokazono, M.; Kawamura, M.; Matsubara, K. In *Thermoelectrics, 2003 Twenty-Second International Conference on - ICT 2003*, p 121.
- (8) Caneschi, A.; Gatteschi, D.; Totti, F. *Coordination Chemistry Reviews* **2015**, 289–290, 357.
- (9) Culp, J. T.; Park, J.-H.; Meisel, M. W.; Talham, D. R. *Polyhedron* **2003**, 22, 3059.
- (10) DeCiccio, D.; Ahn, S. T.; Sen, S.; Schunk, F.; Palmore, G. T. R.; Rose-Petruck, C. *Electrochemistry Communications* **2015**, 52, 13.
- (11) Kim, D.-Y.; Park, Y.; Lee, H. *Catalysis Today* **2007**, 120, 257.
- (12) Kin, T.; Nemoto, T.; Makino, K.; Koide, K. In *Innovative Computing, Information and Control, 2006. ICICIC '06. First International Conference on 2006*; Vol. 3, p 556.
- (13) Li, G.-L.; Ni, Z.-H.; Cheng, W.-Q.; Miao, B.-X.; Zhang, L.-F. *Inorganic Chemistry Communications* **2013**, 31, 58.
- (14) Schujman, S. B.; Slack, G. A. In *Thermoelectrics, 1999. Eighteenth International Conference on 1999*, p 213.
- (15) Shantz, D. F.; Burton, A.; Lobo, R. F. *Microporous and Mesoporous Materials* **1999**, 31, 61.
- (16) Culp, J. T.; Park, J.-H.; Benitez, I. O.; Meisel, M. W.; Talham, D. R. *Polyhedron* **2003**, 22, 2125.
- (17) Frye, F. A.; Pajerowski, D. M.; Lane, S. M.; Anderson, N. E.; Park, J.-H.; Meisel, M. W.; Talham, D. R. *Polyhedron* **2007**, 26, 2281.

- (18) Jinli, Y.; Yan, X.; Desheng, X. *Chemical Physics Letters* **2007**, *435*, 317.
- (19) Pardo, E.; Verdaguer, M.; Herson, P.; Rousseliere, H.; Cano, J.; Julve, M.; Lloret, F.; Lescouezec, R. *Inorg Chem* **2011**, *50*, 6250.
- (20) Peng, Y.; Li, Y.; Ban, Y.; Jin, H.; Jiao, W.; Liu, X.; Yang, W. *Science* **2014**, *346*, 1356.
- (21) Herrera, J.-M.; Baca, S. G.; Adams, H.; Ward, M. D. *Polyhedron* **2006**, *25*, 869.
- (22) LeBaron, P. C.; Wang, Z.; Pinnavaia, T. J. *Applied Clay Science* **1999**, *15*, 11.
- (23) Ying, Z.; Xianggao, L.; Bin, C.; Fei, C.; Jing, F. *Composite Structures* **2015**, *132*, 44.
- (24) Arranz-Andrés, J.; Pérez, E.; Cerrada, M. L. *Polymer* **2012**, *53*, 386.
- (25) Nash, T. L., Novel Two Dimensional Cyanide-Bridged Metal Nanosheets: Crystallographic Study And Preparation By Exfoliation, Master's Thesis, Texas State University, 2011.
- (26) Rayner, J. H.; Powell, H. M. *Journal of the Chemical Society (Resumed)* **1952**, 319.
- (27) Ham, W. K.; Weakley, T. J. R.; Page, C. J. *Journal of Solid State Chemistry* **1993**, *107*, 101.
- (28) Mathey, Y.; Mazieres, C. *Canadian Journal of Chemistry* **1974**, *52*, 3637.
- (29) Niu, T.; Crisci, G.; Lu, J.; Jacobson, A. J. *Acta Crystallographica Section C* **1998**, *54*, 565.
- (30) Nash, T. L.; Beall, G. W.; Lee, B.; Higgins, C. *Science of Advanced Materials* **2014**, *6*, 703.
- (31) Coleman, J. N.; Lotya, M.; O'Neill, A.; Bergin, S. D.; King, P. J.; Khan, U.; Young, K.; Gaucher, A.; De, S.; Smith, R. J.; Shvets, I. V.; Arora, S. K.; Stanton, G.; Kim, H.-Y.; Lee, K.; Kim, G. T.; Duesberg, G. S.; Hallam, T.; Boland, J. J.; Wang, J. J.; Donegan, J. F.; Grunlan, J. C.; Moriarty, G.; Shmeliov, A.; Nicholls, R. J.; Perkins, J. M.; Grievson, E. M.; Theuwissen, K.; McComb, D. W.; Nellist, P. D.; Nicolosi, V. *Science* **2011**, *331*, 568.
- (32) Adame, D.; Beall, G. W. *Applied Clay Science* **2009**, *42*, 545.
- (33) Fornes, T. D.; Yoon, P. J.; Keskkula, H.; Paul, D. R. *Polymer* **2001**, *42*, 09929.
- (34) Gerds, N.; Katiyar, V.; Koch, C. B.; Risbo, J.; Plackett, D.; Hansen, H. C. B. *Applied Clay Science* **2012**, *65–66*, 143.

- (35) Ruan, X.; Huang, S.; Chen, H.; Qian, G. *Applied Clay Science* **2013**, 72, 96.
- (36) Wu, L.; Yang, C.; Mei, L.; Qin, F.; Liao, L.; Lv, G. *Applied Clay Science* **2014**, 99, 266.
- (37) Beall, G. W.; Goss, M. *Applied Clay Science* **2004**, 27, 179.
- (38) Althuluth, M.; Overbeek, J. P.; van Wees, H. J.; Zubeir, L. F.; Haije, W. G.; Berrouk, A.; Peters, C. J.; Kroon, M. C. *Journal of Membrane Science* **2015**, 484, 80.
- (39) Amani, M.; Amjad-Iranagh, S.; Golzar, K.; Sadeghi, G. M. M.; Modarress, H. *Journal of Membrane Science* **2014**, 462, 28.
- (40) Chen, G. Q.; Kanehashi, S.; Doherty, C. M.; Hill, A. J.; Kentish, S. E. *Journal of Membrane Science* **2015**, 487, 249.
- (41) Goh, P. S.; Ismail, A. F.; Sanip, S. M.; Ng, B. C.; Aziz, M. *Separation and Purification Technology* **2011**, 81, 243.
- (42) Buonomenna, M. G. *Desalination* **2013**, 314, 73.
- (43) Fritzmann, C.; Löwenberg, J.; Wintgens, T.; Melin, T. *Desalination* **2007**, 216, 1.
- (44) Hu, Z.; Chen, Y.; Jiang, J. *The Journal of chemical physics* **2011**, 134, 134705.
- (45) Lau, W. J.; Ismail, A. F.; Misdan, N.; Kassim, M. A. *Desalination* **2012**, 287, 190.
- (46) Ebrahimi, M.; Willershausen, D.; Ashaghi, K. S.; Engel, L.; Placido, L.; Mund, P.; Bolduan, P.; Czermak, P. *Desalination* **2010**, 250, 991.
- (47) Zimmerman, J. B.; Mihelcic, J. R.; Smith, J. *Environmental science & technology* **2008**, 42, 4247.
- (48) United States Census Bureau - US Dept. of Commerce
<http://www.census.gov/popclock/> (Accessed May 12,2015).
- (49) Cohen, J. E. *Science* **2003**, 302, 1172.
- (50) *Water security [electronic resource] : national and global issues*; [Reston, Va.] : U.S. Dept. of the Interior, U.S. Geological Survey, [2010], 2010.
- (51) Richter, B. *Chasing Water [electronic resource] : a guide for moving from scarcity to sustainability / by Brian Richter*; Washington, DC : Island Press/Center for Resource Economics : Imprint: Island Press, 2014., 2014.
- (52) Pedro-Monzonís, M.; Solera, A.; Ferrer, J.; Estrela, T.; Paredes-Arquiola, J. *Journal of Hydrology* **2015**, 527, 482.

- (53) United Nations Environment Programme), U.N.E.P., <http://www.unep.org/dewa/vitalwater/article77.html>, (Accessed May 1, 2015).
- (54) Betts, K. *Environmental Science & Technology* **2004**, *38*, 246A.
- (55) Glater, J. *Desalination* **1998**, *117*, 297.
- (56) Chong, T. H.; Loo, S.-L.; Krantz, W. B. *Journal of Membrane Science* **2015**, *473*, 177.
- (57) Drioli, E.; Paul, D. R. *Industrial & Engineering Chemistry Research* **2007**, *46*, 2235.
- (58) Li, D.; Wang, H. *Journal of Materials Chemistry* **2010**, *20*, 4551.
- (59) Pendergast, M. M.; Hoek, E. M. V. *Energy & Environmental Science* **2011**, *4*, 1946.
- (60) Yokozeki, A. *Applied Energy* **2006**, *83*, 15.
- (61) Campbell, N. A. *Biology: Concepts & Connections*; 6th ed.; Pearson/Benjamin Cummings: San Francisco, 2009.
- (62) Ang, W. S.; Tiraferri, A.; Chen, K. L.; Elimelech, M. *Journal of Membrane Science* **2011**, *376*, 196.
- (63) Bereschenko, L. A.; Stams, A. J.; Euverink, G. J.; van Loosdrecht, M. C. *Applied and environmental microbiology* **2010**, *76*, 2623.
- (64) Goosen, M. F. A.; Sablani, S. S.; Al-Hinai, H.; Al-Obeidani, S.; Al-Belushi, R.; Jackson, D. *Separation Science and Technology* **2005**, *39*, 2261.
- (65) Hussain, Y. A.; Al-Saleh, M. H.; Ar-Ratrout, S. S. *Desalination* **2013**, *328*, 17.
- (66) Auxiaqua, <http://www.auxiaqua.es/en/sistemas-filtracion/> (Accessed May 29, 2015).
- (67) Chae, H.-R.; Lee, J.; Lee, C.-H.; Kim, I.-C.; Park, P.-K. *Journal of Membrane Science* **2015**, *483*, 128.
- (68) Lalia, B. S.; Kochkodan, V.; Hashaikeh, R.; Hilal, N. *Desalination* **2013**, *326*, 77.
- (69) Liu, M.; Chen, Z.; Yu, S.; Wu, D.; Gao, C. *Desalination* **2011**, *270*, 248.
- (70) Misdan, N.; Lau, W. J.; Ismail, A. F. *Desalination* **2012**, *287*, 228.
- (71) Pendergast, M. M.; Ghosh, A. K.; Hoek, E. M. V. *Desalination* **2013**, *308*, 180.

- (72) Wang, S.; Wang, Z.; Zhang, Y.; Wu, W.; Liu, D.; Zhang, X. *Desalination* **2005**, *177*, 7.
- (73) Yang, W.; Wang, Z.; Zhou, Y.; Ye, X.; Shi, L.; Cheng, L.; Chen, N.; Dong, W.; Zhang, Q.; Zhang, X. *Desalination* **2013**, *324*, 57.
- (74) Ozaki, H.; Li, H. *Water research* **2002**, *36*, 123.
- (75) Corry, B. *The Journal of Physical Chemistry B* **2008**, *112*, 1427.
- (76) Goh, P. S.; Ismail, A. F.; Ng, B. C. *Desalination* **2013**, *308*, 2.
- (77) Holt, J. K.; Park, H. G.; Wang, Y.; Stadermann, M.; Artyukhin, A. B.; Grigoropoulos, C. P.; Noy, A.; Bakajin, O. *Science* **2006**, *312*, 1034.
- (78) Zuo, G.; Shen, R.; Ma, S.; Guo, W. *ACS Nano* **2010**, *4*, 205.
- (79) Bunch, J. S.; Verbridge, S. S.; Alden, J. S.; van der Zande, A. M.; Parpia, J. M.; Craighead, H. G.; McEuen, P. L. *Nano letters* **2008**, *8*, 2458.
- (80) Cohen-Tanugi, D.; Grossman, J. C. *Nano letters* **2012**, *12*, 3602.
- (81) Cohen-Tanugi, D.; Grossman, J. C. *The Journal of chemical physics* **2014**, *141*, 074704.
- (82) Cohen-Tanugi, D.; Grossman, J. C. *Desalination* **2015**, *366*, 59.
- (83) Zhu, A.; Rahardianto, A.; Christofides, P. D.; Cohen, Y. *Desalination and Water Treatment* **2010**, *15*, 256.
- (84) Thomas, M.; Corry, B.; Hilder, T. A. *Small* **2014**, *10*, 1453.
- (85) Lukov, V.; Kogan, V.; Levchenkov, S.; Shcherbakov, I.; Popov, L. *Russian Journal of Coordination Chemistry* **2015**, *41*, 1.
- (86) Culp, J. T.; Park, J.-H.; Frye, F.; Huh, Y.-D.; Meisel, M. W.; Talham, D. R. *Coordination Chemistry Reviews* **2005**, *249*, 2642.
- (87) Gallagher, N. M.; Olankitwanit, A.; Rajca, A. *The Journal Of Organic Chemistry* **2015**, *80*, 1291.
- (88) Spinu, L.; Dodrill, B. C.; Radu, C. In *Internet; International, M. T., Ed.; Magnetics Technology International: 2013*, p 2.
- (89) Bejoy, V.; Rajesh, S.; Nandakumaran, V. M. *Turkish Journal of Physics* **2015**, *39*, 60.

- (90) Cheng, C. Y. *Biology and regulation of blood-tissue barriers*; Springer Science+Business Media, Landes Bioscience: New York, N.Y., Austin, Tex., 2012.
- (91) Cheng, F.; Ma, Y. *Computer-aided design, manufacturing, modeling and simulation II : selected, peer reviewed papers from the 2nd International Conference on Computer-Aided Design, Manufacturing, Modeling and Simulation (CDMMS 2012), September 21-23, 2012, Chongqing, China / edited by Fangyin Cheng and Yan Ma*; Durnten-Zurich, Switzerland ; Enfield, NH : Trans Tech Publications, [2013], 2013.
- (92) Dae-Eun, L.; Minseok, S. *International Journal of Control & Automation* **2014**, 7, 75.
- (93) Gower, D. J. *Biotic evolution and environmental change in Southeast Asia*; The Systematics Association : Cambridge University Press: Cambridge, 2012.
- (94) International Conference on Life System, M.; Simulation; Li, K.; Dr **2007**.
- (95) Somogyi; Gali. *Journal of Physics: Condensed Matter* **2014**, 26, 14.
- (96) Tomasula, P. M.; Datta, N.; Yee, W. C. F.; McAloon, A. J.; Nutter, D. W.; Sampedro, F.; Bonnaille, L. M. *Journal Of Dairy Science* **2014**, 97, 4594.
- (97) Buehler, M. J.; Yung, Y. C. *Nature Materials* **2009**, 8, 175.
- (98) Sholl, D. S.; Steckel, J. A. *Density functional theory [electronic resource] : a practical introduction / David S. Sholl and Jan Steckel*; Hoboken, N.J. : Wiley, c2009., 2009.
- (99) Bungartz, H. J.; Zimmer, S.; Buchholz, M.; Pflüger, D. *Modeling and Simulation [electronic resource] : An Application-Oriented Introduction / by Hans-Joachim Bungartz, Stefan Zimmer, Martin Buchholz, Dirk Pflüger*; Berlin, Heidelberg : Springer Berlin Heidelberg : Imprint: Springer, 2014., 2014.
- (100) Walter, J. C.; Barkema, G. T. *Physica A* **2015**, 418, 78.
- (101) Kaier, W.; Steyn-Ross, M. L.; Steyn-Ross, D. A.; Wilson, M. T.; Sleigh, J. W.; Yoichi, S. *BMC Systems Biology* **2014**, 8, 1.
- (102) Öchsner, A.; Merkel, M. *One-Dimensional Finite Elements [electronic resource] : An Introduction to the FE Method / by Andreas Öchsner, Markus Merkel*; Berlin, Heidelberg : Springer Berlin Heidelberg : Imprint: Springer, 2013., 2013.
- (103) Reddy, J. N. *An introduction to the finite element method*; 3rd ed.; McGraw-Hill Higher Education: New York, NY, 2006.

- (104) Thompson, E. G. *An introduction to the finite element method : theory, programming, and applications*; John Wiley: Hoboken, NJ, 2004.
- (105) White, R. E. *An introduction to the finite element method with applications to nonlinear problems*; Wiley: New York, 1985.
- (106) Forrai, A. *Embedded Control System Design [electronic resource] : A Model Based Approach / by Alexandru Forrai*; Berlin, Heidelberg : Springer Berlin Heidelberg : Imprint: Springer, 2013., 2013.
- (107) Li, D.-C.; Liu, C.-W.; Chen, W.-C. *International Journal of Production Research* **2012**, *50*, 6679.
- (108) Box, G. E. P. *An accidental statistician [electronic resource] : the life and memories of George E.P. Box / George E.P. Box*; Hoboken, New Jersey : John Wiley & Sons, c2013., 2013.
- (109) Rappe, A. K.; Casewit, C. J.; Colwell, K. S.; Goddard, W. A.; Skiff, W. M. *Journal of the American Chemical Society* **1992**, *114*, 10024.
- (110) Rappe, A. K.; Colwell, K. S.; Casewit, C. J. *Inorganic Chemistry* **1993**, *32*, 3438.
- (111) Nosé, S. *The Journal of chemical physics* **1984**, *81*, 511.
- (112) Chang, W.-K.; Chiang, R.-K.; Wang, S.-L. *Journal of Solid State Chemistry* **2007**, *180*, 1713.
- (113) Manohara, G. V.; Vishnu Kamath, P.; Milius, W. *Journal of Solid State Chemistry* **2012**, *196*, 356.
- (114) Radha, S.; Milius, W.; Breu, J.; Kamath, P. V. *Journal of Solid State Chemistry* **2013**, *204*, 362.
- (115) Cohen-Tanugi, D.; Grossman, J. C. *Nano letters* **2014**, *14*, 6171.
- (116) Cohen-Tanugi, D.; McGovern, R. K.; Dave, S. H.; Lienhard, J. H.; Grossman, J. C. *Energy & Environmental Science* **2014**, *7*, 1134.
- (117) Banhart, F.; Kotakoski, J.; Krasheninnikov, A. V. *ACS Nano* **2011**, *5*, 26.
- (118) Sassi, K. M.; Mujtaba, I. M. *Desalination* **2012**, *306*, 8.
- (119) Pall Corp. <http://www.pall.com/main/laboratory/product.page?id=20023>, (Accessed May 30, 2015).
- (120) Advantec MSF, http://www.advantecmfs.com/filtration/membranes/mb_ptfephil.shtml, (Accessed June 1, 2015).
- (121) Park, P. K.; Lee, S.; Cho, J. S.; Kim, J. H. *Water research* **2012**, *46*, 3796.

- (122) Rey, R.; Hynes, J. T. *Journal of Physics: Condensed Matter* **1996**, 8, 9411.
- (123) Brown, T. L. *Chemistry : The Central Science / Theodore L. Brown, University of Illinois at Urbana-Champaign, H. Eugene LeMay, Jr., University of Nevada, Reno, Bruce E. Bursten, University of Tennessee, Knoxville, Catherine J. Murphy, University of Illinois at Urbana-Champaign, Patrick M. Woodward, The Ohio State University, Matthew W. Stoltzfus, The Ohio State University*; Boston : Pearson, [2015] 13th edition., 2015.